

UNIVERSITA' DEGLI STUDI DI ROMA
"La Sapienza"

Dipartimento di Chimica

2005

XVIII ciclo di dottorato in Scienze Chimiche

Structural and Electronic Properties of Chiral Molecules on Surfaces

Relatore Esterno
Dott. T. Prosperi

Relatore Interno
Prof. F. A. Gianturco

Simona Irrera

Contents

1	Introduction	4
2	Chirality	8
2.1	Enantioselectivity	11
2.2	Chiral Recognition Process	15
2.3	Creating Chirality at Surfaces	16
2.3.1	Modified surface: adsorption in UHV	20
2.3.1.1	Self-Assembled monolayers	24
2.4	Alaninol: A Chiral Amino-Alcohol	26
3	Experimental Techniques	29
3.1	Randomly Oriented Chiral Molecules: Spectroscopy	29
3.1.1	Photoelectron Spectroscopy	33
3.1.2	Circular Dichroism in Angle Resolved Photoelectron Spectroscopy	35
3.2	Experimental Surface Science Techniques	40
3.2.1	Photoelectron spectroscopy: surface case	41
3.2.2	Low energy electron diffraction	43
3.2.3	Scanning tunnelling microscopy	45
3.2.4	Synchrotron radiation	48

4	Experimental Apparatus	53
4.1	AR-XPS Apparatus ISM laboratory	54
4.2	Circular Polarization Beamline	59
4.2.1	Electromagnetic elliptical wiggler (EEW)	59
4.2.2	UPS chamber: CDAD apparatus	60
4.3	VUV Photoelectron Beamline	62
4.3.1	Experimental set up	62
4.4	STM Apparatus at Advanced Photoelectric-effect Experiment (APE) Beamline	63
4.5	Sample Preparation: Procedure	66
5	Circular Dichroism in Angle Resolved Photoelectron Spec- troscopy in Gas Phase: D- and L-Alaninol	69
5.1	Photoelectron Spectroscopy of L-Alaninol in Gas Phase	70
5.2	Circular Dichroism (CDAD) of D- and L-Alaninol	84
5.3	Conclusions	93
6	D-Alaninol Adsorption on Cu(100) and Cu(110)	96
6.1	Single Crystal Copper Surfaces	97
6.1.1	Clean Cu (100) and (110)	100
6.2	D-Alaninol on Cu(100) Surface: Results	102
6.2.1	Adsorption: growth morphology	102
6.2.2	Low energy electron diffraction (LEED)	105
6.2.3	Photoelectron spectroscopy results	107
6.2.4	Scanning tunneling microscopy images	116
6.2.5	Conclusions: Adsorption Structure	120
6.3	D-Alaninol on Cu(110): Growth Dynamics	123

7 Conclusions and Future Development	129
Bibliography	135

Chapter 1

Introduction

Chirality is the symmetry property of objects which exist in two mirror-like forms not superimposable, such as hands ($\chi\varepsilon\iota\rho$, kheir = hand, in greek); these two mirror faces are called enantiomers. The importance of such a property is emphasized by the fact that life on earth is based on chiral biomolecules such as proteins, aminoacids, sugars, RNA and DNA, all naturally selected with a single handedness. Human proteins are exclusively built from “left-handed” aminoacids, while all sugars are “right-handed”. Homochirality allows these molecules to suit to enzymes; otherwise DNA could not be stabilized in a helix structure, thus a long chain could not be formed if only one monomer had the opposite-hand (left).

Chiral systems associated with molecular species have attracted strong interest, over the past decades, because of the evidence of chiral sensitivity in chemical based communication. Chirality is crucial for general and fundamental reactions such as those involved in pharmaceutical and biological processes and a stereoselective reaction could be exploited in catalysis for bio-compatible materials and sensors [1, 2, 3].

This work concerns two correlated topics: chiral molecules in the gas phase

and chiral molecules chemisorbed on metal surfaces, with special focus on the possibility of yielding chiral properties from a three dimensional randomly oriented system (gas phase) to supramolecular ordered assemblies.

Electronic, vibrational and optical spectroscopies coupled with *ab initio* simulations are classical and powerful tools to face the problem of transferring chiral expression from molecules to ordered assemblies. A new insight in this field is offered by the use of circularly polarized synchrotron light provided from third synchrotron radiation generation source. Circularly polarized synchrotron radiation is a chiral probe and photoelectron spectroscopy of gas phase systems have been proved to be ideal for investigating asymmetrical interactions governing biological processes. Circular Dichroism (CD) is the different intensity response from a chiral molecule to right and left circularly polarized light and is the main tool to characterize the chiral properties of enantiomers. CD was intensively measured in optical and infrared absorption, the new advance is to investigate CD in the angular distribution (CDAD) of photoelectrons. This tool adds new features: first, it is possible to associate CD effect to each structure in the photoionization spectra; second, this effect is larger in magnitude compared to the absorption. [4, 5]

Few papers are already available in literature on rigid ring-like structured molecule such as bromocamphor [6] and methyloxirane [7], a new upgrade is to direct attention on quasi-linear molecule with a biological and catalytical interest as amino-alcohols.

The way in which biologically or catalytically active molecules bind to and then order onto surfaces is topical for a number of applications. The structure, conformation and local order of these molecules upon adsorption influence their interaction with further incoming species and the process of

molecular recognition, so acting as enantioselective catalysts.[8]

A surface science approach, therefore, has been applied to understand essential interaction between inorganic surfaces and organic asymmetrical molecules by studying model systems, at first consisting of small units adsorbed on surfaces.

R-(-) and S-(+)-2-Amino-1-Propanol also known as D- and L-Alaninol have been studied in the gas phase with photoelectron spectroscopies and CDAD. Experimental data are presented and discussed in Chapter 5.

D-Alaninol has been deposited on Cu (100) and Cu(110) in Ultra High Vacuum; D-Alaninol on Cu(100) has been investigated by means of low energy electron diffraction (LEED), photoelectron spectroscopies in soft X-ray and UV range and scanning tunnel microscopy (STM); experimental results are illustrated in Chapter 6.

Investigation of the growth of D-Alaninol on Cu(110) surface has been performed, even if this experiment is still at a preliminary stage, results are presented as well.

So far only few studies of this systems have been investigated [9, 10] despite of the interest in life science [11, 12].

Surface modification induced by chemisorption of organic systems yields new properties to surface, especially, the catalytic functionalities added can be used to produce enantiomerically pure compounds which are central in chiral molecular recognition both in an unoriented and oriented environment.

The program of this theses required the setting up and instrumental characterization of a new laboratory UHV-XPS apparatus equipped with LEED optics to select and study heterogeneous samples. This AR-XPS is located at the Istituto di Struttura della Materia (ISM) at the Consiglio Nazionale della

Ricerca (CNR) in 'Tor Vergata' Area della Ricerca in Rome, Italy.

Chapter 2 describes fundamental concepts on chirality that is the base of this study, and the most common spectroscopies employed are briefly described in Chapter 3. Equipments and experimental set-ups are described in Chapter 4.

D- and L-Alaninol have been preliminary characterized with photoelectron spectroscopy and CDAD in the gas-phase by means of synchrotron radiation that provides higher resolved and circularly polarized photons (Chapter 5). Interaction of D-Alaninol and copper surfaces have been first investigated in our laboratory by means of XPS and LEED tools in order to understand the adsorption dynamics and the growth morphology and then extended to STM and synchrotron radiation UPS investigation for topography and valence band characterization (Chapter 6).

Chapter 2

Chirality

The concept of chirality is a central topic since most of biochemistry is chiral. Classes of bio-molecules such as aminoacids and sugars are largely found to be homochiral.

The origin of homochirality in the living world is still an open and attractive field. History of the research developments in understanding of chirality in the universe and on earth can be found in Mason's "Chemical Evolution" book together with other important topics concerning the origin of the elements, molecules and living systems [13]. As reported in this publication, many theories have been proposed to explain the rise of homochirality both in biology and in basic physics interactions. In 1860 Pasteur postulated that forces involved in enantioselectivity weren't reproducible in laboratory [14] and between 1884 and 1919 Fisher studying sugar (D) and aminoacids (L) homochirality proposed "key and lock" reaction mechanism¹ [15, 16, 17]. He, also, studied how plants can optically resolve the two enantiomers of glucose to build up cellulose [18]. At this point it began to be clear how nature selects enantiomers

¹a molecule that acts as receptor interacts exclusively with an acceptor on specific sites based on its complementary shape

Pasteur, discovering diastereomers ², found a new laboratory method to separate racemate mixture. Up to now, a general way to discriminate between enantiomers (R and S) is to introduce a chiral probe that is an homochiral compound, since enantiomers have identical physical properties, the reaction with a chiral compound (such as R') provides diastereomers (RR' and SR') which are not mirror images, so these can be separated by means of common techniques like different solubility in water, boiling and melting point.

Nevertheless, all the hypothesis and findings for propagation of biomolecular homochirality left unknown features on initial pre-biotic enantioselection. Dissymmetry has been observed, indeed, not only in bioactive systems but also in the interstellar medium. An L-excess of aminoacids was found in the Murchison meteorite [19, 20, 21] (figure 2.1) and could be the missing link between a purely racemic scenario on the pre-biotic earth and the almost complete homochirality of life. The analysis of the aminoacids found in this meteorite yields an L-excess of more than 10%. Anyway, all aminoacids isolated from the cores of the other carbonaceous meteorites are found invariably to be racemic.

In 1895 Cotton discovered the differential absorption of left- and right-circularly polarized light by an optically active substance [22]. This difference was called circular dichroism (CD), $\Delta\epsilon = \epsilon_L - \epsilon_R$, where ϵ_L and ϵ_R are the molar extinction coefficients for left- and right-circularly polarized light. CD is equal in magnitude but opposite in sign for two enantiomers. Thus, a solution of the racemic mixture of two enantiomers, irradiated with one of the two forms of the circularly polarized light at a wavelength producing photochemical change, is expected to become optically enriched in the enantiomer with the smaller extinction coefficient for the particular circular radiation component employed.

²when there are two or more chiral centers in a molecule, its stereoisomers that are not enantiomers are called diastereomers which are, thus, not chiral.



Figure 2.1: Murchison meteorite whichin an L-aminoacid excess was found.

In 1929 Kuhn investigated enantioselective photolysis by means of irradiation with circularly polarized light hence producing a selective destruction of one enantiomer leading to an excess of its opposite. But, he, also, found that CD in absorption vanishes when integrated over the spectrum as a whole [23, 24]. Hence, in the optical region circularly polarized light can lead to slight excess of the L- or D-form in a sample if only a narrow spectral region is used instead of white light.

In the first half of the twentieth century the principle of conservation of parity (1927, Wigner) became dominant and it was, generally assumed to apply both to classical and nuclear interactions. But in 1929, Franklin and, then in 1956, T.D. Lee and C.N. Yang provided evidence of “parity violation” in the weak nuclear interaction [25, 26]. Weak nuclear interaction can, thus, play a central role in generating an enantiomeric excess due to its dissymmetric nature. Except of weak nuclear interaction all known forces do not violate the parity conservation, especially, the electromagnetic forces that determine

chemistry and molecular structure give no preference to the L- or the D-form. This leads to the well known consequence, that chiral molecules always occur as racemic mixtures when they are created from achiral compounds in an achiral environment. The problem of how chiral biology could have evolved from purely racemic substances had a new input when it has been observed that absorption due to circular polarization in the UV - soft X-ray in the interstellar environment can produce the selective destruction of amino acid enantiomers of a particular configuration so, amino acid homochirality could be a result of the excitation from exposure to UV circularly polarized light originated in interstellar medium. Even if this phenomenon can only create a small excess of a few percent but it was, also, observed that once a little excess of an enantiomer has been formed then it acts as a catalyst in its consequent formation.

Moreover, synchrotron radiation originating in the galaxy, for instance from the spinning of a neutron star, has been proposed as source of polarized light, [27] and it could have caused homochirality as well.

Finally many theories have been postulated but scientific community has not yet reached a general agreement leaving this as an opened and unsolved problem.

2.1 Enantioselectivity

Chirality and enantioselectivity have attracted the interest of the scientific community since Pasteur's discovery because the chemical and biological activity of a substance often depends on its stereochemistry.

The first manifestation of optical activity was pointed out by Arago [28] in 1811, during his study on the interaction of a quartz plate with polarized light. Several years later, Biot [29] showed that this phenomenon was not confined to

crystalline substances. Solution of certain natural products also possessed the property of rotating the plane of polarization of the plane-polarized light. Biot studied the physical law of the phenomenon in detail and showed, in particular, that the angle of rotation varies linearly with the thickness of the solution through which the beam of the light passes, as well as with the concentration of active product. Furthermore, he showed that the angle of rotation varied with the wavelength.

In 1848 Pasteur identified chiral molecules, sodium ammonium tartrate crystals, and separated physically those into right-hemihedral and left-hemihedral shapes, in other word, they were specular images to each other. He found out, that the two crystals rotate the plane of polarization of the light differently, clockwise and counterclockwise [30, 31, 32, 33]. This was the case of a chiral molecule that performs a spontaneous resolution by crystallization since enantiomers co-crystallize forming a conglomerate of two enantiomorphous crystal, and it is common to about 1% of the known systems. Moreover, he showed the importance for organic synthesis whichin the possibility of separating racemates into active enantiomers constitutes the main step.

Optical rotatory power was rapidly found to be an essential characteristic of many organic substances, but Pasteur's discovery of the optical resolution of racemic tartrates represented the most significant advance. Pasteur was able to interpret the observed hemihendry of crystals and correlate their macroscopic asymmetry with the asymmetry of the molecule itself, thus initiating the science of optical isomerism. He deduced that the rotatory power was connected with the existence of non-superimposable asymmetry in the molecule. Moreover, he showed the importance for organic synthesis since the possibility of separating racemates into active enantiomers constitutes the main step.

At that time bond theory was only at an early stage but Pasteur was able to visualize the tetragonal carbon bond. He had, in fact, observed that, when the hemihedral facets of tartrate crystals are protracted, tetrahedral are obtained; the orientation of which changes with the sign of the optical activity of the tartrate.

The concept of a carbon atom situated at the center of the tetrahedron with its valence bonds directed toward the apices was not defined until the results of work by Le Bel [34] and van't Hoff [35] appeared in 1874. If four different substituents are attached to the carbon atom, the molecule possesses a rotatory power. The concept of the asymmetry carbon atom was, thus, deduced.

The theory of the asymmetric carbon atom was developed upon the fact that the presence of at least one such carbon atom in the molecule was necessary to give rise to optical activity; but this was found to be false. Certain molecules such as biphenyl derivatives for example, can be optically resolved, and in order to explain these phenomena, we have to return to Pasteur's concept of molecular dissymmetry and ascribe optical activity to any molecule whose mirror image is not superimposable with the original. It should be added that Le Bel had recognized this fact in his publication, which covered not only molecules containing carbon but also molecules encountered in inorganic chemistry.

Stereochemistry was born at this point. The concept of molecules in three dimensions was fundamental, but it was not less important to define for each individual case the configuration of the molecule, that is, the position in space of each atom.

Enantiomers are labelled R or S according to the nomenclature rules (se-

quence rule method, Cahn, Ingold and Prelog - 1966 [36]); a traditional nomenclature is used for aminoacids and carbohydrates (and similar structures as amino-alcohols), it indicates with labels D or L corresponding to R and S. (+) and (-) labels are connected to rotation of the plane polarized light clockwise and counter-clockwise, respectively.

The most of the biological receptors and membranes are chiral so many drugs, herbicides, pesticides and other biological agents must possess chirality for binding and action to occur.

Synthetic processes ordinarily produce a racemic mixture, that is, both enantiomers (left and right-handed molecules) are present at the same concentration. Two enantiomers can behave differently in a biological system.

There are many of this example: in the past this had led to tragic consequences such as for a sedative drug, thalidomide.

In perfumes and odours, also, chirality lead to peculiar diversity such as aspartame, one enantiomer is sweet and is used instead of common sugar, saccharose, but its mirror opposite is bitter; S- and R-limonene are essence of lemon or essence of orange, respectively.

Enantiomeric purity has become, then, one of the major concerns in the pharmaceutical industry. Much attention is direct to find a way of chiral separation by chromatography and membrane, and to design syntheses using bio and heterogeneous catalysts that enable only one enantiomer to be formed. In pharmaceutical industry enantiomeric purity can be gained by chromatography (liquid and gas) and capillary electrophoresis using chiral stationary phases [37].

Another connected field is environment science, where investigations are moved to the chirality of pollutants, such as herbicides and pesticides. Vital

information can be provided to assessing bio-availability, toxicity and transport. Reliable sensors capable of determining concentrations of enantiomers are needed.

Spectroscopy was largely developed for crystalline and liquid and only recently direct to gas phase whose interest involves molecular recognition processes and has implication for the origin of homochirality. The weak interactions involved in chiral discrimination can be investigated with gas phase techniques.

A second new area for physical chemistry is the study of chiral surfaces. Chiral surfaces could be used to catalyze the synthesis of optically pure samples working as heterogeneous chiral catalysts. Chiral surfaces are increasingly of interest for applications such as stereoselective chemical synthesis, surface modification in microelectronics and sensors, resolution of chiral compounds, protein adsorption and crystal growth.

2.2 Chiral Recognition Process

The molecular recognition process is the way how molecules identify each other and it is based on shape interactions between them. This process is central in living systems as witnessed by, among others, receptor-ligand, antigen-antibody, DNA-protein and receptor-medicine interactions.

The investigation of this phenomenon can be performed in gas phase since the absence of solvent decreases the complexity of the chemical environment which is reproducible; thus, different systems can be compared and insight on effects of structural modifications can be achieved. Moreover, these experiments can be compared directly to theoretical *ab initio* simulations.

Chiral recognition is one of the most challenging areas of molecular recog-

dition since it deals with selection between molecules that are atomically identical but distinct on the order of atoms, that is, they are stereoisomers and non covalent interactions plays a key role in this contest. Aminoacids are characterized by a side chain called residue which has different acid-base properties and affinity with water (hydrophilic or hydrophobic) so it is able to form weak bonds. Polypeptides are long chains formed by covalent interaction between $-COOH$ and $-NH_2$ of aminoacids, then this long chains interact by non covalent forces into 3D structures more and more complex such as hemoglobin.

Interactions in biological systems require high specificity, this is imparted through a chiral recognition, in fact, this weak forces can only be established according to the correct atomic positioning.

2.3 Creating Chirality at Surfaces

In organic chemistry, chirality is generally charged to a tetrahedral carbon where all the four attached substituent groups are different, which implies the impossibility of superimposing mirror faces. The general requirement is that the symmetry group of the unit structure contains no improper rotations, which include reflection planes, rotation-reflection axes and a centre of inversion. This definition can be moved easily from 3D objects to 2D structures, so chirality at surfaces is a bidimensional property since a surface can not possess a centre of inversion in 3D and can only maintain reflection mirror symmetry planes normal to the surface. In the case of solid surface the unit cell as a whole must be considered; if the molecules (or ions) in the unit cell are arranged in a dissymmetric pattern, the crystal will be optically active.

2D chirality can be created at surfaces in two ways: first, one can consider a naturally chiral surface [38]; second, one can adsorb chiral molecules on

a flat surface [39]. Chiral surfaces can be built from chiral constituents or chirality can be imparted to the surface from kinks and defects of high miller indices; both deserves attention but organic-metal adsorption offers more issues regarding conformation of the adsorbent which is important for reactivity and recognition processes, hence attention is focused on chemisorption on achiral metal surfaces.

Organic molecules bring to a metal surface many attributes, among these, chirality draws a special attention since it imparts a new function of selectivity. Chiral surfaces, as previously pointed, are deeply involved in many areas such as stereoselective chemical synthesis, surface modification in microelectronics and sensors, separation of chiral compounds, protein adsorption and crystal growth. This properties are due to a 'selective function' operated from empty/occupied sites left from a previous controlled adsorption of asymmetric adsorbate.

The adsorption of a non chiral molecules at a non chiral surface can lead to a chiral surface under controlled conditions but this chirality is expressed only at local level depending on alignment and disappears at the global one, that is, the surface is analogous to a racemic mixture and present no overall chirality. When a chiral molecules is adsorbed at a non chiral surface, it introduces chirality at the surface, that is the chirality of the adsorbent enables chiral expression to progress from local to global level. Adsorption of a chiral molecules which leaves the chiral center intact inevitably leads to local chiral system. Multiple functionalities possessed by these molecules which enable lateral interactions to be expressed explain the overall chirality that takes place on the surface. This features are well illustrated in a recent review by Barlow and Raval [2] and summarized in figure 2.2, in this picture all the

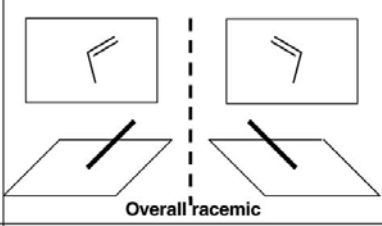
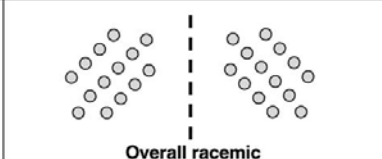
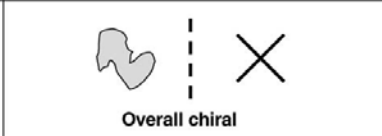
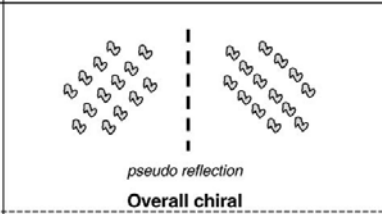
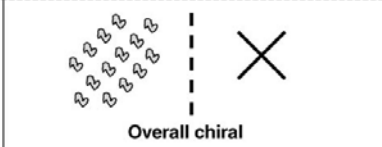
Non-chiral molecules	
<p>Adsorption induced chiral motifs.</p> <p><i>-alignment of molecule breaks the reflection symmetry axes of surface:</i> local point chirality <i>(i.e. belongs to a chiral point group).</i></p>	 <p style="text-align: center;">Overall racemic</p>
<p>Adsorption induced chiral arrangements (or domains).</p> <p><i>-the ordered domains possess a chiral space group:</i> local organisational chirality.</p>	 <p style="text-align: center;">Overall racemic</p>
Chiral molecules	
<p>Molecule induced chiral motifs.</p> <p><i>-intact preservation of chiral centre upon adsorption i.e. creates local chiral point group:</i> global point chirality.</p>	 <p style="text-align: center;">Overall chiral</p>
<p>Adsorption induced chiral arrangements.</p> <p><i>(i) asymmetric lateral interactions e.g. mediated by groups that are non-chiral - reflectional domains allowed:</i> global point and local organisational chirality.</p>	 <p style="text-align: center;"><i>pseudo reflection</i> Overall chiral</p>
<p><i>(ii) chiral lateral interactions- no reflectional domains allowed:</i> global point and global organisational chirality</p>	 <p style="text-align: center;">Overall chiral</p>

Figure 2.2: Classification of chirality at a surface due to self-assembly monolayer forming. [2]

possible motifs produced from chemisorption on surface are outlined.

Fundamental papers on this topic appeared at the end of 90's. In these experiments, chiral molecules modifies achiral surfaces to impart enantiospecificity to the surface [39]. Tartaric Acid adsorbed onto Cu(110) produces chiral surfaces [40]. Cysteine adsorbed on Au(110) from a racemic mixture forms molecular pairs that are exclusively homochiral [41]. The importance of a subsequent employment of this research in heterogeneous catalysis is witnessed by Nakagawa et al. they studied Raney nickel modified with (R,R)-tartaric

acid and found out that it can be used to catalyse the hydrogenation of β -ketoesters, producing the R-product with over 90% enantiomeric excess and S-product using (S,S)-tartaric acid [8]. Heptaelicene on Ni(111) surface was found to close pack, then the sample was subjected to metal vapor deposition to prepare a metal surface with preferred handedness [42].

Chiral surfaces could be used to catalyze the synthesis of optically pure samples, with the benefit of easily retrieving the catalyst afterwards. Fundamental studies of chiral surfaces underlie this effort to design heterogeneous chiral catalysts. Understanding molecule/surface interactions is also important for the improvement of chiral separations via chromatography. A prevailing model of retention of analytes in chiral stationary and mobile phases involves a 'three point recognition' process, if an analyte contacts the target at no less than three of its geometry points, the chirality of the analyte can be recognized and one enantiomer retained in favor of the other (the basis for separation) [43].

This approach has one problem: the adsorption has to be carried on along the synthesis [40], that is in a particular and not always real condition. Surface science studies on single crystal model systems performed under idealized condition, i.e., ultra high vacuum, have contributed substantially to a general understanding of elementary mechanisms governing gas-surface reactions and thereby the technologically important area of heterogeneous catalysis [44, 45]. In a few cases it has even been demonstrated that new catalysts, operating in technologically relevant conditions, can be designed on the basis of such fundamental surface science insight [46, 47].

Self-Assembly monolayer formation is studied through electron spectroscopy together with another major surface science technique, scanning tunneling mi-

croscopy (STM) that is also applied to determine chirality.

2.3.1 Modified surface: adsorption in UHV

The adsorption of chiral molecules on surfaces offers many features regarding the conformation of the adsorbent and is investigated with UHV standard surface science tools, using a well-defined single crystal model systems as substrates. The experimental conditions, even if idealized, represents a significant environment to investigate the elementary interactions underlying adsorbate-substrate bonding.

In this view essential issues on molecular adsorption on surfaces is illustrated and self-assembly mechanism is presented.

Adsorption describes the process whereby a molecule (adsorbate) forms a bond to the surface (adsorbent); the fractional coverage of adsorbate (θ) is defined as

$$\theta = \frac{N_s}{N} \quad (2.1)$$

where N_s is the number of surface sites occupied by adsorbate and N stands for the total number of substrate adsorption sites and is often numerically equivalent to the total number of surface atoms of the substrate; when $\theta=1$, the adsorbate ensemble is called monolayer.

Considering the kinetic theory of gases, the rate of surface bombardment by molecules (Z) is given by

$$Z = \frac{p}{(2\pi mkT)} cm^{-2} s^{-1}$$

where p = ambient pressure, in Ncm^{-2} ; m = molecular mass, in kg molecule^{-1} ; T = absolute temperature, in K ; and, k = Boltzmann constant, in J K^{-1} .

The rate of surface contamination will also depend upon the sticking prob-

ability S since the gas molecule may collide with the surface but it may not sticky. Assuming $S = 1$, we can estimate from (2.1) the coverage of a typical contaminant like CO (atomic mass = 28) produced at 300 K and at a pressure of 10^{-6} torr and 10^{-10} torr.

At 10^{-6} torr, (1 torr = $1.333 \times 10^{-2} \text{Ncm}^{-2}$)

$$Z = \frac{(1.333 \times 10^{-2} \times 10^{-6})}{[2 \times \pi \times (\frac{28}{1000 \times 6.02 \times 10^{23}}) \times (1.38 \times 10^{-23}) \times 300]} \text{cm}^{-2} \text{s}^{-1} = 3.82 \times 10^{14} \text{cm}^{-2} \text{s}^{-1}$$

At 10^{-10} torr,

$$Z = \frac{(1.333 \times 10^{-2} \times 10^{-10})}{[2 \times \pi \times (\frac{28}{1000 \times 6.02 \times 10^{23}}) \times (1.38 \times 10^{-23}) \times 300]} \text{cm}^{-2} \text{s}^{-1} = 3.82 \times 10^{10} \text{cm}^{-2} \text{s}^{-1}$$

Assuming an atomic density of $d = 10^{15} \text{cm}^{-2}$ (typical of most surfaces), the rate of surface contamination of CO ($S=1$) at 300K would be: $\frac{Z}{d} = 0.382$ monolayers $\cdot\text{s}^{-1}$ at 10^{-6} torr and 3.82×10^{-5} monolayers $\cdot\text{s}^{-1}$ at 10^{-10} torr.

Time taken to adsorb one monolayer at 10^{-6} torr $\Rightarrow 1/0.382 = 2.6$ s while at 10^{-10} torr $\Rightarrow (1/3.82) \times 10^5 = 26178 \text{ s} \simeq 7$ hours.

Since we aspire to study a well characterised adsorbate/substrate system at atomic level and while the experiment is performed, a constant composition of the system is required so UHV is needed to minimize contaminations.

Procedures for cleaning a contaminated surface depends on the solid, a general method to clean a metal surface is to sputter it with an ion gun which accelerate rare gas ions against the surface, to restore order on the surface after sputtering procedure, it is necessary to anneal the sample. Annealing will rearrange the surface into an ordered one (see section 4.5).

UHV request in surface science rises not only to prevent surface from contaminations but also to perform electron spectroscopies; the mean free path of UV and X-ray photons and photoemitted electrons is such that the probability they are absorbed or scattered before reaching either the sample or the analyser is high.

Gases below their critical temperature tend to adsorb as a result of general van der Waals interactions with the solid surface. The term adsorption is used to define the accumulation of an adsorbate at the surface of a solid or adsorbent; when a chemical bond is established between them, the adsorption phenomenon is called chemisorption, otherwise if the forces involved are intermolecular (van der Waals forces³), physisorption.

Physical adsorption equilibrium is rapid to attain and is reversible, the adsorbate being removed without change by lowering the pressure decreasing the temperature of the substrate. It is supposed that this type of adsorption occurs as a result of the same type of relatively nonspecific intermolecular forces that are responsible for the condensation of a vapor and in physisorption the heat of adsorption is of the same order of heats of condensation.

Chemisorption (or chemical adsorption) is an adsorption in which the forces involved are valence-like; the same as those operating in the formation of chemical compounds. Atoms on a surface clearly differ from their bulk counterparts since they cannot interact symmetrically with neighbouring atoms. Due to that, they commonly exhibit unsaturated valencies that cause an attractive force normal to the surface plane and allow them to form bonds with foreign atoms or molecules on the surface.

Strong adsorbate bonding to a solid substrate must be understood in terms of a chemical reaction, similar to the case of molecular covalent bonding. When the molecule (M) approaches the metal surface (S), one expects covalent bonding between the partially filled orbitals of the two partners, i.e., the orbital overlapping between M and S should lead to chemisorption with re-hybridisation

³In the last century J. D. van der Waals recognized the existence of weak non covalent forces [48, 49, 50]. Weak attractive interactions (dipole-dipole, dipole-induced dipole and induced dipole-induced dipole) are commonly called “van der Waals forces”.

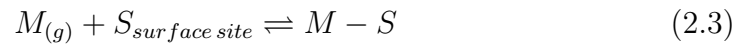
and formation of new MS orbitals, thus, modifying core lines and valence band of molecule and surface.

Chemisorption may be slow and the rate behavior indicative of the presence of an activation energy; in fact, it may be possible for a gas to be physically adsorbed at first, and then, more slowly, to undertake some chemical reaction with the surface of the solid.

The number of surface sites occupied by adsorbate molecules at equilibrium at a particular temperature will depend on the gas pressure P . The dependence of θ on P at constant temperature is called an adsorption isotherm; at low values of P the isotherm is linear and obeys at Henry's law

$$P = constant \times \theta \quad (2.2)$$

for an adsorption reaction:



we gain this Langmuir isotherm equation

$$\theta = \frac{N_s}{N} = \frac{KP}{1 + KP} \quad (2.4)$$

where $K = k_a/k_d$ and k_a and k_d are the rate constants for the adsorption and desorption steps.

The Langmuir growth curve is characterized by a growth rate being proportional to the number of available sites on the surface, we can write:

$$\frac{d\theta}{dt} = R(1 - \theta) \quad (2.5)$$

↓

$$\theta = 1 - \exp^{-Rt} \quad (2.6)$$

where t is the exposure time of the substrate to the gas phase and $\tau=1/R$ is the growth factor that is the characteristic time of the growth.

Curve growth are commonly shows as a function of exposure expressed in Langumir that is $1\text{s} \cdot 10^{-6}$ torr, which at a constant pressure is proportional to the exposure time.[51, 52, 53]

This model has some limits indeed the solid surface should be uniform and should contain a number of equivalent sites each of which may be occupied by only one molecule of adsorbate, a dynamic equilibrium must exist between the gas (at pressure) and the adsorbate layer at constant temperature, moreover the intermolecular interactions between adsorbed molecules should be negligible. An approach due to Fowler and Guggenheim [54] allows provision for interaction between adsorbed molecules. Monolayer adsorption are treated in terms of interatomic potential functions in a fundamental approach by Steele [55], and includes pair and higher order interactions; Young and Crowell [56] give additional details on the general subject and a recent treatment is by Rybolt [57].

2.3.1.1 Self-Assembled monolayers

Nanostructures have recently attracted great interest in the scientific community both for technological applications and fundamental science; self-organization of atoms or molecules and development in characterization techniques have allowed progress in manufacturing of high performance nanostructured devices, which find a wide range of applications, i.e. in catalysis, sensors, adhesion, corrosion inhibition, molecular recognition, optoelectronics and lithography.

Molecular organic materials have opened new perspectives of research be-

cause of the advantages organic chemistry can offer, especially, handness and variety; it is, moreover, an easy changeable, versatile and suitable tool.

This phenomenon is called Self-Assembly Monolayers (SAM) and can be grown either from solution or from gas phase, resulting in stable molecular assemblies by adsorption of surfactant molecule with a specific affinity of its functional group to the substrate. In this work, growth from gas phase has been chosen and so the sample (adsorbate+substrate) has been created *in situ*, this allows a clean environment and a better control of the growth conditions even if it is more expensive due to the UHV equipment.

The defining feature of self-assembly monolayer is thus the strong interaction between the head-group and substrate. This interaction, generally, involving molecule-substrate chemical bonding (chemisorption), constitutes the driving force for the adsorption onto the surface, while its complex interplay with the intermolecular interactions leads to the spontaneous structuring of the two-dimensional assembly. The structural phase is commonly accompanied with a first rapid adsorption that, then transforms itself into the fully-coverage structure with a long range order. Order formation is related to the rearrangement of the terminal groups which, weakly interacting each others (van der Waals, dipole-dipole and hydrogen bonds), package themselves into the lowest energy structure.

Self-assembly of molecules into stable, structurally well-defined supramolecular architectures allows a level of control over selection and placement of the constituent subunits in the supramolecular complexes and is attractive since it is a basic mechanism in the formation of a wide variety of biological nanoscale structures. Self-assembly is involved in the formation of membranes from lipid molecules and the living cell.

Spontaneous aggregation of organic molecules on surface was exploited by Langmuir [58, 59] at the beginning of the last century (see previous section); at present, self-assembly on solid surfaces has been recognized as a powerful tool for growing uniform nanostructures with regular size and spacing in a controlled way.

In the gas deposition method the substrate is located in an UHV chamber, which allows the preparation of a clean surface by sputtering and annealing. When the clean sample surface is exposed to a controlled flux of molecules, adsorption and self-organization could take place; the dynamics of these processes can be checked by using several techniques as described in the next chapter.

2.4 Alaninol: A Chiral Amino-Alcohol

The amino-alcohols represent a largely diffused class of biologically active substances. They characterise several drugs and natural substances like ephedrine, adrenaline, noradrenaline and some naturally occurring sphingoid like sphingosine and sphinganine.

The knowledge of complexing properties of amino-alcohols is not yet exhaustive and only a few issues related to their complex equilibria are known [12, 60]. In particular sphingosine and sphinganine in the last few years have received great attention because of their activity as inhibitors of tumoral cells growth [11, 61, 62, 63, 64]. Moreover, since a coordination bond involving the amino group also influences the pharmacological activity of amino-alcohols, interactions with metal ions had been studied to allow an efficient regulation of active species concentration [65].

Alaninol is an amino-alcohol with two functional groups, $-\text{NH}_2$ and $-\text{OH}$.

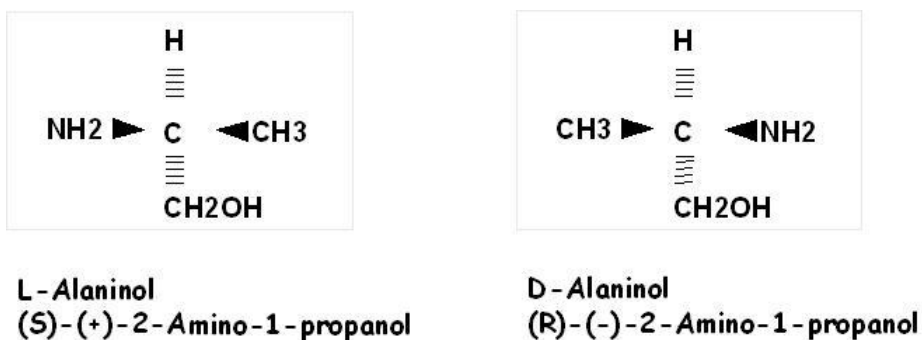


Figure 2.3: Alaninol Structure of both the enantiomers

Both are very important in organic and biological chemistry due to their coordinating properties. This molecule, rather unexplored, has been chosen because of the biological and catalytical activity and because it can be taken as a model for aminoacid-like structures. Alaninol is a reduced form of Alanine, it exist in liquid phase at room temperature and it can be evaporated easily into the vacuum chamber preventing from any decomposition due to heating or other treatment that a solid sample (like aminoacids) needs for sublimating.

Alaninol structure is shown in figure 2.3 in its two enantiomeric forms. Alanine, presented in figure 2.4 close to Alaninol, for comparison, is the simplest chiral amino-acid with a side group consisting of a methyl group ($-\text{CH}_3$).

Alaninol has a terminal $-\text{OH}$ group while alanine is a carboxylic acid and its monomer form exist as zwitterion ($+\text{NH}_3\text{CHCH}_3\text{COO}^-$) this is no longer true for amino-alcohols whose alcohol group is less acid ($\text{CH}_3\text{CH}_2\text{OH} - \text{pK}_a = 16$, $\text{CH}_3\text{COOH} - \text{pK}_a = 5$).⁴

⁴Acidity of alcohols in water can be defined in this way, consider
 $\text{ROH} + \text{H}_2\text{O} \rightleftharpoons \text{H}_3\text{O}^+ + \text{RO}^-$

acid dissociation constant of this reaction is k_a , and is defined by

$$K_a = \frac{[\text{H}_3\text{O}^+][\text{RO}^-]}{[\text{ROH}]}$$

This balance is referred to a diluted solution where water concentration can be considered negligible. k_a units are mol L^{-1} or molarity. Since k_a is a small number is more comfortable and so more diffuse to use

$$\text{pK}_a = -\log K_a$$

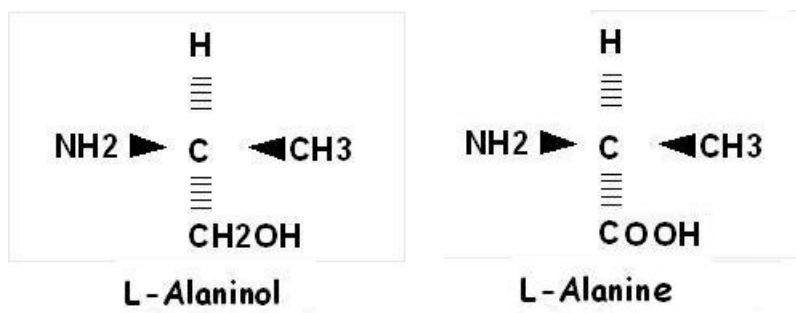


Figure 2.4: L-Alanine structure compared to L-Alaninol structure.

Chapter 3

Experimental Techniques

Experimental techniques used for this theses are here, shortly, described for gas phase and surface science study. A multi technical approach is required in order to exhaustively investigate the relation between electronic and structural properties of gas phase systems and thin films deposited on single-crystal metal surfaces.

3.1 Randomly Oriented Chiral Molecules: Spectroscopy

New antiviral, antibiotic and anticancer drugs manufacturing are greatly enlarged thanking to increasing studies, collection, isolation and structure determination of novel chiral natural products [66, 67]. One of the most challenging aspects of molecular structure determination is the assignment of the relative and absolute stereochemistry [68].

Most common chiral-sensitive measurements are: optical activity (or polarimetry) and circular dichroism spectroscopies. Polarimetry measures the

rotation polarization plane of linearly polarized light by chiral media, when measurements are made as a function of wavelength it is called optical rotatory dispersion (ORD). Also electronic and vibrational spectroscopy methods are widely used to assist in absolute stereochemical assignment. In the past years Circular Dichroism (CD) has focused mainly upon rigid structures with stereocenters in close proximity to chromophores and performed in absorption up to X-ray range.

The strengths of ORD and CD are related to the rotatory power. Rotatory power did not allow the configuration of a given product to be defined until 1951 when Bijvoet [69] employing an X-ray diffraction method, was able to solve the problem of absolute configuration. Measurement of rotatory power was employed for years in the visible region at a given wavelength (sodium D line or green and blue lines of mercury), but this was found to be an imperfect tool since these lines generally lie far from the absorption regions of the constituent groups in molecular compounds.

Rotatory power varies with wavelength and Biot [70] pointed out that rotatory dispersion was a more interesting characteristic of a substance than a simple measurement at a given wavelength. However, Cotton was the first to study rotatory dispersion in detail within the actual regions of absorption of chromophores and this as early as 1896 [22]. In addition the work of Levene, Pickard, Kenyon, Lowry, Kuhn and Rupe [71] should be quoted for theoretical developments. Considerable difficulties were met measuring rotatory power in the ultraviolet region (where most chromophores absorb), especially for what concerning time required to carry out the experiments. A huge development was the description of photoelectric polarimeters for use in the ultraviolet [72] and recording spectro-polarimeters [73, 74, 75] since it became simpler to

trace a dispersion curve. Anyway this technique has some intrinsic limitations, a continuous background due to the chromophores which absorb in the more distant ultraviolet is always superimposed upon the Cotton effect of a chromophore, this background disturbs and prohibits studies of fine structure to be performed.

Circular dichroism does not have this disadvantage. The phenomenon was studied by Cotton [22] at the same time as rotatory dispersion and he had shown that each optically active material absorbs left and right circularly polarized light to different extents.

Circular dichroism and rotatory dispersion are two manifestations of the same phenomenon, that is, the interaction between polarized light and asymmetric molecular structure.

Optical activity measurements are obtained when two conditions are met, first, molecules must be asymmetric, that is, have no center or plane of symmetry; second, light of helicoidal symmetry, i.e. circularly polarized light, must be employed.

CD can be measured between 1000 cm^{-1} in the infrared region and 75500 cm^{-1} (c.a. 9 eV) in the vacuum UV region covering the vibrational and electronic spectra.

Modern ORD and CD spectrometers cover in the near ultraviolet and visible regions of the spectrum, therefore measure electronic transitions. The methods are inherently sensitive to chirality, unlike other powerful structural tools such as Nuclear Magnetic Resonance (NMR), which requires chiral shift agents to determine chirality [76]. CD and ORD are of little use in studying molecules that do not have accessible chromophores.

When CD is conducted in the infrared region of the spectrum, vibrational

transitions are excited in the molecule, and vibrational CD, that is VCD, is achieved. Despite the fact that vibrational CD is several orders of magnitude smaller than electronic CD (due in part to the low frequency of the optical transitions), VCD is an useful tool for absolute molecular structure determination in solution when chiral species are involved. VCD was first implemented in 1974 by Holzwarth et al. [77] and Nafie [78]. VCD has the advantage to be a fast experiment (about one hour) but is difficult to interpret without extensive *ab initio* calculation, and for signal to noise ratio problems requires concentrated samples.

Circular Dichroism was extended to the X-ray region only very recently since it is a smaller effect (10^{-3} compare to 10^{-1} or 10^{-2} in UV), and both handedness of circularly polarized light and both enantiomers are required to perform the experiments. Moreover, these experiments are now made possible due to the development of high-brilliance synchrotron source with insertion devices capable of delivering high circular polarization rates. A great advantage is reached at this point since CD in Vibrational and Ultraviolet regions can determine a global dichroism while in X-ray absorption the local chirality around a given atom can be probed selecting its characteristic absorption threshold.

In the last years Circular Dichroism (CD) has also been used in gas phase enantio-discrimination performing an Angle-Resolved Photoelectron Spectroscopy (ARPES) experiment. In comparison to CD in absorption, CDAD is more intense in magnitude (10^{-2} compare to 10^{-3}).

Circular Dichroism in Angle-Resolved Distribution (CDAD) is a technique implemented in the last few years (see section 3.1.2). CDAD is the main tool for a chiral characterization of asymmetric systems but few studies have been

performed [79, 6, 7, 80].

First experiment appeared in 2001 when Bowering et al. studied photoionization of free, unoriented bromocamphor with circular polarized radiation obtaining a significant circular dichroism effect in the angular distribution. The spectra for left- and right-handed enantiomers of bromocamphor exhibit asymmetries up to several percent [6]. This effect can be similarly studied for biologically and catalytically active molecules.

So far only experiment on rigid or semi-rigid molecular systems were performed, now CDAD of D- and L-Alaninol has been studied, and is the first non cyclic molecule.

3.1.1 Photoelectron Spectroscopy

In a photoelectron spectroscopy experiment radiation in the VUV and soft X-ray causes photo-excited electrons to be emitted into the vacuum continuum.

For a molecule in the gas phase



where in each orbital, j , electrons have a characteristic binding energy, that is, the minimum energy needed to eject them to infinity.

In the one-electron picture, ionization potential for the removal of electrons from different molecular orbitals are obtained, according to the Koopman's theorem, with this expression:

$$I_j = -\varepsilon_j$$

where ionization potential, I_j , is equal to an orbital energy, ε_j

Thus, photoelectron spectrum of a molecule is a direct representation of the molecular orbital energy diagram.

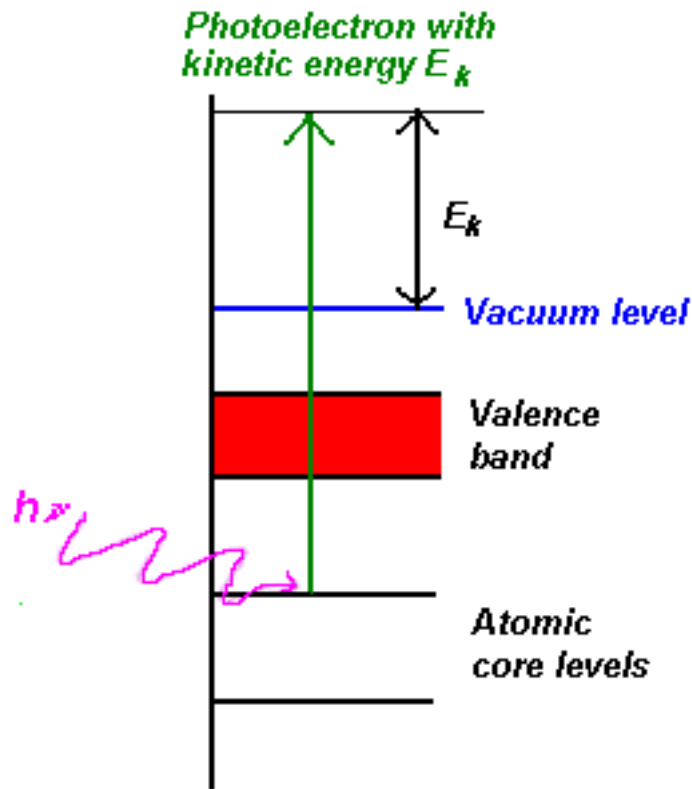


Figure 3.1: Outline of photoelectron spectroscopy technique.

This technique is schematically illustrated in figure 3.1.

Photoelectrons ejected are separated according to their kinetic energies in an electron energy analyser, detected and recorded. Applying the principle of energy conservation, kinetic energy (KE) of the electrons is in relation to the binding energy I_j (often referred as E_b) as:

$$KE = h\nu - I_j \quad (3.2)$$

Theoretical models to explain this phenomenon can be found elsewhere [81, 82, 83] and also an *ab initio* theoretical approach to photoelectron has been formulated in terms of the multiple scattering theory and based on the Green's function approach [84, 85].

3.1.2 Circular Dichroism in Angle Resolved Photoelectron Spectroscopy

Circular dichroism (CD) is the difference in the absorption intensity between right and left circularly polarized light and is an useful tool to investigate structural and optical properties of chiral molecules.

The quantum mechanical approach to light absorption involves evaluating matrix elements of a radiation-molecule interaction operator between initial and final states, according to the conservation of energy. The cross section for a photon absorption process in which there is an electronic transition from an initial state $\langle i|$ to a final state $|f\rangle$ is given by

$$\sigma = (4\pi^2\alpha_0\hbar/e^2\omega)|\langle i|H_{int}|f\rangle|^2\delta(E_f - E_i - \hbar\omega) \quad (3.3)$$

for radiation of angular frequency ω . α_0 is the fine structure constant and the δ - function takes care of energy conservation. The interaction operator here is essentially the scalar product of the electron momentum \mathbf{p} and the space part of the vector potential \mathbf{A} of the radiation field:

$$H_{int} = (e/m)\mathbf{p} \cdot \mathbf{A}$$

$$\mathbf{A} = \varepsilon e^{i\mathbf{k}\cdot\mathbf{r}}$$

for photons with wave-vector \mathbf{k} and polarization vector ε interacting with an electron at position \mathbf{r} .

The vector potential may be expanded in truncated Taylor series,

$$e^{i\mathbf{k}\cdot\mathbf{r}} = 1 + i\mathbf{k} \cdot \mathbf{r} \quad (\text{provided that } \mathbf{k}\cdot\mathbf{r} \ll 1)$$

which when substituted into the cross-section expression gives:

$$\sigma = (4\pi^2\alpha_0\hbar/e^2\omega) | \langle i | \varepsilon \cdot \mathbf{p} + i(\varepsilon \cdot \mathbf{p})(\mathbf{k} \cdot \mathbf{r}) | f \rangle |^2 \delta(E_f - E_i - \hbar\omega)$$

The $| \langle i | \varepsilon \cdot \mathbf{p} | f \rangle |^2$ contribution gives rise to the electric dipole absorption responsible for a large part of the electronic spectroscopy. The second term in the matrix element may be divided into a symmetric part, identifiable with the electric quadrupole interaction, and an antisymmetric part which is the magnetic dipole operator:

$$(\varepsilon \cdot \mathbf{p})(\mathbf{k} \cdot \mathbf{r}) = 1/2[(\varepsilon \cdot \mathbf{p})(\mathbf{k} \cdot \mathbf{r}) + (\varepsilon \cdot \mathbf{r})(\mathbf{k} \cdot \mathbf{p})] + 1/2[(\varepsilon \cdot \mathbf{p})(\mathbf{k} \cdot \mathbf{r}) - (\varepsilon \cdot \mathbf{r})(\mathbf{k} \cdot \mathbf{p})]$$

$$= \text{electric quadrupole} + \text{magnetic dipole}$$

The presence of these higher order terms in the expansion of the transition operator results in further contribution to the absorption cross section. Due to their dependence on powers of $\mathbf{k} \cdot \mathbf{r}$, these are expected to be smaller than the electric dipole contribution in many circumstances. For example, consider visible light ($\lambda = 500 \text{ nm}$) for which $|k| = 2\pi/\lambda \sim 2 \times 10^6 \text{ m}^{-1}$. Since $|\mathbf{r}| = 10^{-10} \text{ m}$ for a valence electron, $\mathbf{k} \cdot \mathbf{r} = 2 \times 10^{-4}$. At X-ray wavelengths, however, $|k| \sim 5 \times 10^9 \text{ m}^{-1}$ and $\mathbf{k} \cdot \mathbf{r} \approx 5 \times 10^{-1}$. Quadrupole activity is thus expected to be considerably enhanced in the X-ray region compared with the visible.

In the general treatment of higher order contributions to optical activity, Chiu [86] showed that, when the transition operator is written as a series with electric and magnetic multipole contributions:

$$T = E1 + E2 + \dots + M1 + M2 + \dots = \text{electric dipole} + \text{electric quadrupole}$$

+ ... + magnetic dipole + magnetic quadrupole + ...

then contributions to the total transition probability due to cross terms between transition moment operators of opposite parity are responsible for the differential absorption of circularly polarized light.

In total absorption CD depends on the second-order electric dipole-electric quadrupole E1-E2 and electric dipole-magnetic dipole E1-M1 operators so this is a weak effect of the order of 10^{-3} .

In angle-resolved photoelectron spectroscopy the dichroic effect shows up at the electric dipole level (E1) and in the differential cross section appears the dichroic effect that is non-zero only for chiral molecules, its magnitude is expected to be around 10^{-2} [87].

The photoelectron signal measured for randomly oriented asymmetric molecule in gas-phase and using circularly polarized light, is related to angle dependent photoionization intensity (the differential cross section of the process), in accordance with the following equation:

$$I(\theta) = \frac{\sigma(\omega)}{4\pi} \left[1 + \left(-\frac{1}{2}\right)^{|m_r|} \beta(\omega) P_2(\cos(\theta)) + m_r D(\omega) P_1(\cos(\theta)) \right] \quad (3.4)$$

where σ is the cross section, β is the asymmetry parameter and D is the dichroism parameter, that appears only for asymmetric system like chiral one. These dynamical quantities depend on the photon energy ω . P_i is the Legendre polynomial of the i th order, θ is the scattering angle between the photoelectron momentum, light propagation axis and the laboratory frame. The light polarization is described by m_r values (the projection of the photon spin along its momentum), +1 and -1 for circular right-hand and left-hand polarized light and 0 for linear polarized light.

In the case of achiral molecules and linearly polarized light the equation (3.4) becomes:

$$I(\theta) = \frac{\sigma(\omega)}{4\pi} [1 + \beta(\omega)P_2(\cos(\theta))] \quad (3.5)$$

If the molecule is chiral, equation (3.5) can be written as:

$$I(\theta) = \frac{\sigma(\omega)}{4\pi} [1 - \frac{1}{2}\beta(\omega)P_2(\cos(\theta)) + m_r D(\omega)P_1(\cos(\theta))] \quad (3.6)$$

where $P_2(\cos(\theta)) = \frac{3}{2}\cos^2\theta - \frac{1}{2}$ and $P_1(\cos(\theta)) = \cos\theta$.

When photons with one selected helicity interacts with asymmetric molecules of one handedness the angular distribution becomes asymmetric and the photoelectron emission should be different with respect to forward and backward directions of the photon beam; the last term of the equation (3.6) can be gain by a reversal of helicity, emission direction and changing the sample with its opposite enantiomer.

Considering equation (3.6), ARPES intensities are labelled $I^+(\theta)$ and $I^-(\theta)$ for helicity +1 (right-hand) and helicity -1 (left-hand), respectively. The difference and the sum are:

$$I^+(\theta) - I^-(\theta) = \frac{\sigma D}{2\pi} \cos \theta \quad (3.7)$$

and

$$I^+(\theta) + I^-(\theta) = \frac{\sigma}{2\pi} [1 - \frac{\beta}{2}P_2(\cos\theta)] \quad (3.8)$$

Normalizing the difference with the sum, it is possible to remove dependence on the cross-section, obtaining the A_{CDAD} parameter:

$$A_{CDAD} = \frac{I^+(\theta) - I^-(\theta)}{I^+(\theta) + I^-(\theta)} = D \frac{\cos \theta}{1 - \frac{\beta}{2} P_2(\cos \theta)} \quad (3.9)$$

so D is:

$$D = A_{CDAD}(\theta) \frac{1 - \frac{\beta}{2} P_2(\cos \theta)}{\cos \theta} \quad (3.10)$$

At this point D could be determined but β has to be measured as well, depending on the energy. Dependence on β can be removed if $P_2(\cos \theta) = 0$ this is valid when $\theta = \theta_m = 54.7^\circ$.

Thus, choosing

$$\theta = \theta_m = 54.7^\circ \Rightarrow P_2(\cos \theta) = 0 \quad (3.11)$$

as in figure 3.2.

D becomes

$$D = \frac{1}{\cos \theta_m} A_{CDAD}(\theta_m) = \sqrt{3} A_{CDAD}(\theta_m) \quad (3.12)$$

Finally, switching the polarization of the light - $I^+(\theta)$ and $I^-(\theta)$ - this experiment enables to determine D parameter and sign reversal of D parameter is gained measuring with opposite enantiomers.

Moreover, placing detectors opposite each other since $\cos \theta_m = -\cos(\theta_m + 180^\circ)$, as can be seen in the apparatus outline (chapter 4), and maintaining the same polarization, photon energy and enantiomer, A_{CDAD} absolute value remains the same but the sign is opposite, obtaining a symmetrical trend. or switching helicity. This behaviour characterizes chiral systems.

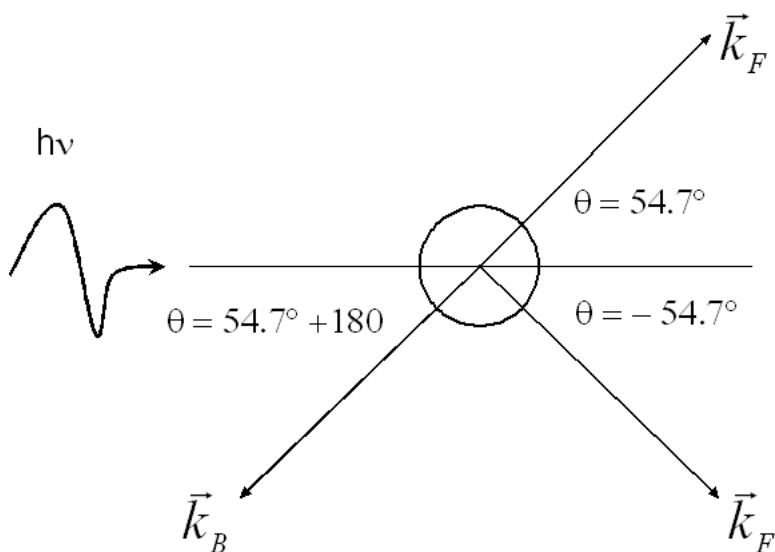


Figure 3.2: In this point placement of the detectors is illustrated.

3.2 Experimental Surface Science Techniques

The study of the adsorption structure of chiral substances adsorbed on surface is essential for heterogeneous enantioselective catalysis. This field is based on using chiral compounds as modifiers of metallic catalysts to achieve what is called enantioselectivity, that is, to provide enantiomerically pure products.

Studies of gas-solid interfaces is the central topic of many areas of pure and applied research (corrosion, electronic device manufacture, heterogeneous catalysis). Here it is reported a short review of the techniques used along this work for solid samples. The study of these topics is a multi-disciplinary field in which many techniques contribute. Local structure details, like chemical nature of the adsorbed species and its bonding can be obtained by X-ray and UV photoelectron spectroscopy (XPS and UPS). The main success in this area is the discovery of the ability of these organic molecules to self-organize and produce remarkably ordered, crystalline-like structures at metal surfaces. Details of these 2D assemblies have been captured by means of low

energy electron diffraction (LEED) and scanning tunneling microscopy (STM) experiments.

Results are presented in Chapter 5, here a short description of the surface science techniques used in this work is illustrated.

3.2.1 Photoelectron spectroscopy: surface case

The photoelectron spectroscopy is one of the most versatile techniques used for chemical analysis of surfaces.

The basis have been illustrated in section 3.1.1 and equation (3.1) in the case of surfaces becomes:

$$KE = h\nu - E_b + \phi_s \quad (3.13)$$

where binding energy is conveniently referred to Fermi level that in the case of metals is always visible in the spectrum. Surface sensitivity is a crucial matter to address since a fraction of a monolayer on a 1 cm^2 sample may contain less than 10^{14} atoms or molecules compare to c.a. 10^{20} in a bulk sample. This technique is extremely sensitive at surfaces and the reason lies in the low mean escape depth for scattered photoelectrons emitted from the substrate. A measure of this parameter is provided by the inelastic mean free path, λ , which has been measured for many solids. The dependence of λ on electron kinetic energy for many solid elements is shown in figure 3.3.

The minimum of $\lambda=5\text{-}10 \text{ \AA}$ at 10-100 eV implies that, under these conditions, only the first few atomic layers of the solid are sampled. Moreover, it is clear from the figure 3.3 that the use of a source of variable photon energy can be used to “tune” the photoelectron kinetic energy to a position in or near the minimum and, thus, to optimize the surface sensitivity.

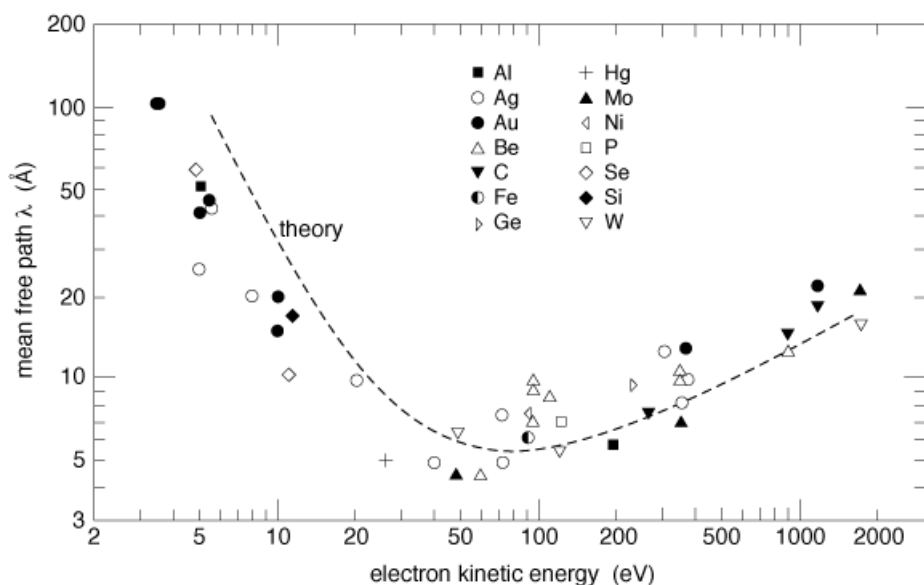


Figure 3.3: The inelastic mean free path for electrons in solids. Dots are measurements and dashed line is calculation [88]

Photoelectron spectroscopy is particularly useful to study adsorbed species on surface owing to the small penetration depth for electrons, thus, photoelectron spectra of surface contain strong bands from adsorbates together with bands characteristic of the substrate, normally the strongest, though modified by adsorption.

After adsorption the atomic energy level might be shifted (or split) and broadened, forming a resonance level. This technique may detect such resonance levels as distinct changes in the local density of states near the surface after adsorption. Comparison of the energy levels of the same atom before and after adsorption, that is, comparison of the gas-phase photoelectron spectra to adsorbate resonance levels, can provide information on the electronic character of the interacting bond which acts in the adsorbate system.

X-ray photoelectron spectroscopy (XPS) is a tool to characterize core levels resulting in high chemical specificity, chemical shifts on adsorbates permit conclusion on chemisorption bonding although interpretation is complicated

by atomic and extra-atomic relaxation. UV photoelectron spectroscopy (UPS) is highly surface sensitive since a very short electron mean free path (5-10Å) for 20-100 eV photon energies. Valence levels involved in bonding or not, are directly observed with high resolution and adsorbate resonance may be identified even if assignment of the features is not unique.

3.2.2 Low energy electron diffraction

Detection of crystallographic order and quality of surface can be performed by means of low energy electron diffraction technique (LEED). In a LEED experiment incident electrons from a monochromatic beam are elastically back scattered from a surface and analysed in the energy range 20-200 eV.

Electrons in this energy range possess inelastic mean free paths of order of few Å and may only travel a few atomic layers into the surface; they possess de Broglie wavelengths of the same order of magnitude as the interatomic distances at surfaces and, hence, may undergo diffraction if the atoms in the surface are arranged periodically.

The interference between elastically scattered waves gives rise to a well-defined diffraction pattern in which the positions of the intensity maxima (which appear as spots in luminescent screen that acts as a detector) are related to the long range periodicity of the lattice. LEED provides informations about the translational symmetry of the system in the reciprocal space, but it is rather readily to obtain information about the real space using the expressions which relate the primitive translational vectors of the reciprocal lattice (\mathbf{a}_1^* and \mathbf{a}_2^*) to those of the real lattice (\mathbf{a}_1 and \mathbf{a}_2):

$$\mathbf{a}_1^* = 2\pi \frac{\mathbf{a}_1 \times \mathbf{n}}{\mathbf{a}_1 \cdot \mathbf{a}_2 \times \mathbf{n}}, \mathbf{a}_2^* = 2\pi \frac{\mathbf{a}_2 \times \mathbf{n}}{\mathbf{a}_1 \cdot \mathbf{a}_2 \times \mathbf{n}} \quad (3.14)$$

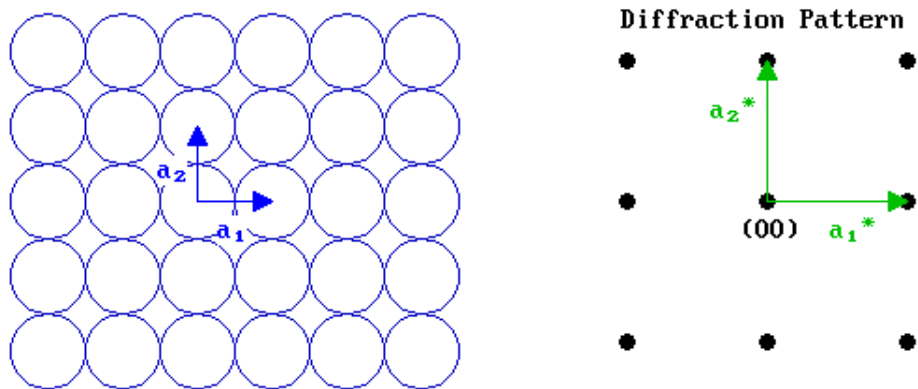


Figure 3.4: Diffraction pattern and real specie for a fcc lattice at 100 surface.

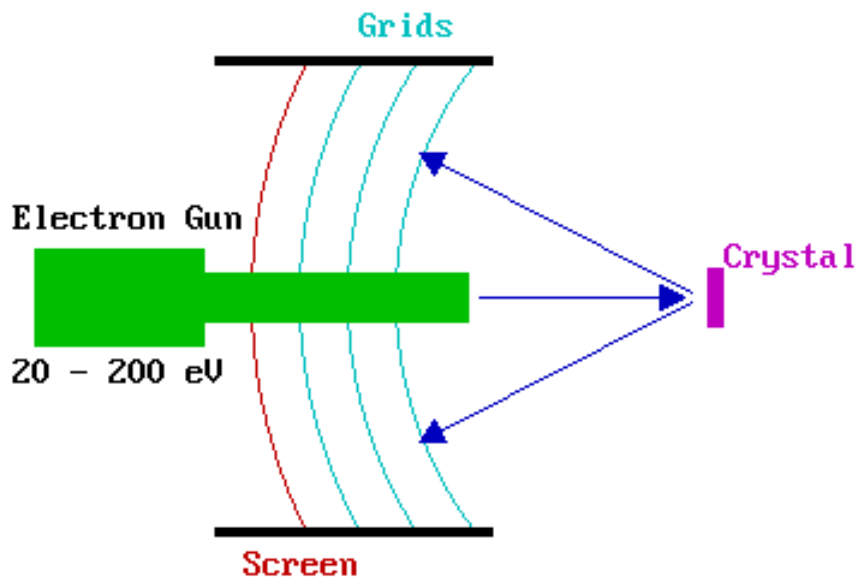


Figure 3.5: LEED outline.

where \mathbf{n} is a unit vector normal to the surface; this is shown in figure 3.4 for an fcc (100) surface.

Figure 3.5 illustrates schematically the experimental apparatus necessary to perform a LEED experiment.

The LEED apparatus ensures that only those electrons of kinetic energy E_b (the primary beam energy) reach the phosphor screen (detector). If an ordered surface array is prepared, discrete electron beams emerge from the

substrate whose spatial distribution reflects the symmetry of the ordered array.

Two dimensional periodicity of surface unit cell size may be deduced from the position of the diffracted beams along with variations in the unit cell size induced by adsorption; when, indeed, the resulting structure of adsorbate-substrate system is ordered (as in the systems studied in this work), this order is usually described by relating its Bravais lattice to that of the underlying solid. The more general way to do this is writing the primitive translation vectors of the surface unit mesh ($\mathbf{a}_1', \mathbf{a}_2'$) as a linear combination of those of the corresponding plane of the underlying substrate ($\mathbf{a}_1, \mathbf{a}_2$), so that:

$$\begin{aligned} \mathbf{a}'_1 &= p_1 \mathbf{a}_1 + q_1 \mathbf{a}_2 \\ \mathbf{a}'_2 &= p_2 \mathbf{a}_1 + q_2 \mathbf{a}_2 \end{aligned}$$

The overlayer can therefore be specified by the matrix:

$$\begin{pmatrix} p_1 & q_1 \\ p_2 & q_2 \end{pmatrix}$$

The vectors of the substrate (overlayer) are always chosen so that $|\mathbf{a}_1| \leq |\mathbf{a}_2|$ ($|\mathbf{a}'_1| \leq |\mathbf{a}'_2|$), the angle between them is $\geq 90^\circ$ and the coordinate system is right-handed.

This is the notation used in Chapter 6 to describe the overlayer formed by the adsorption of alaninol on Cu(100).

3.2.3 Scanning tunnelling microscopy

The scanning tunnelling microscopy (STM) was invented by Gert Binnig and Heinrich Rohrer at IBM, Switzerland, in 1982, [89] for which they received the Nobel Prize for Physics in 1986. An atomically sharp tip is brought within a

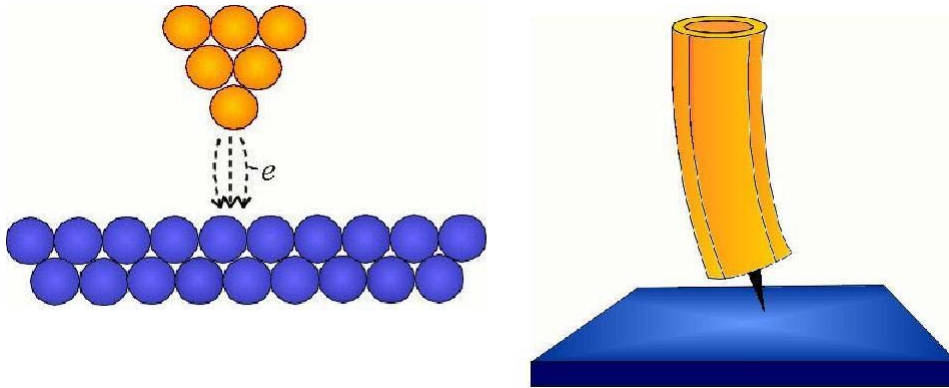


Figure 3.6: STM technique outline

few nanometres of a surface and a small potential difference is applied between the tip and the sample. If the tip is biased positively relative to the sample an energetic incentive is provided for electrons from the sample to flow to the tip, where their potential energy will be lowered.

When a small tip-surface separation is reached, instead of surmounting the activation energy barrier for electron transfer (the work function), electrons are able to pass through the small vacuum gap by a process known as 'electron tunnelling'. Electrons are thus able to flow between the tip and the surface, producing a measurable current. The magnitude of this current is exponentially dependent on the tip-surface separation. The larger the distance between the tip and the surface, the smaller the current. Therefore, by measuring the magnitude of the tunnelling current as the tip is moved across the surface, a topographic image of the surface is obtained. In favourable circumstances, atomic resolution can be achieved.

The tunnelling current (I) depends exponentially on the sample to tip gap (W) and the sample work function (ϕ)

$$I(W) = C \exp(-W \sqrt{\phi})$$

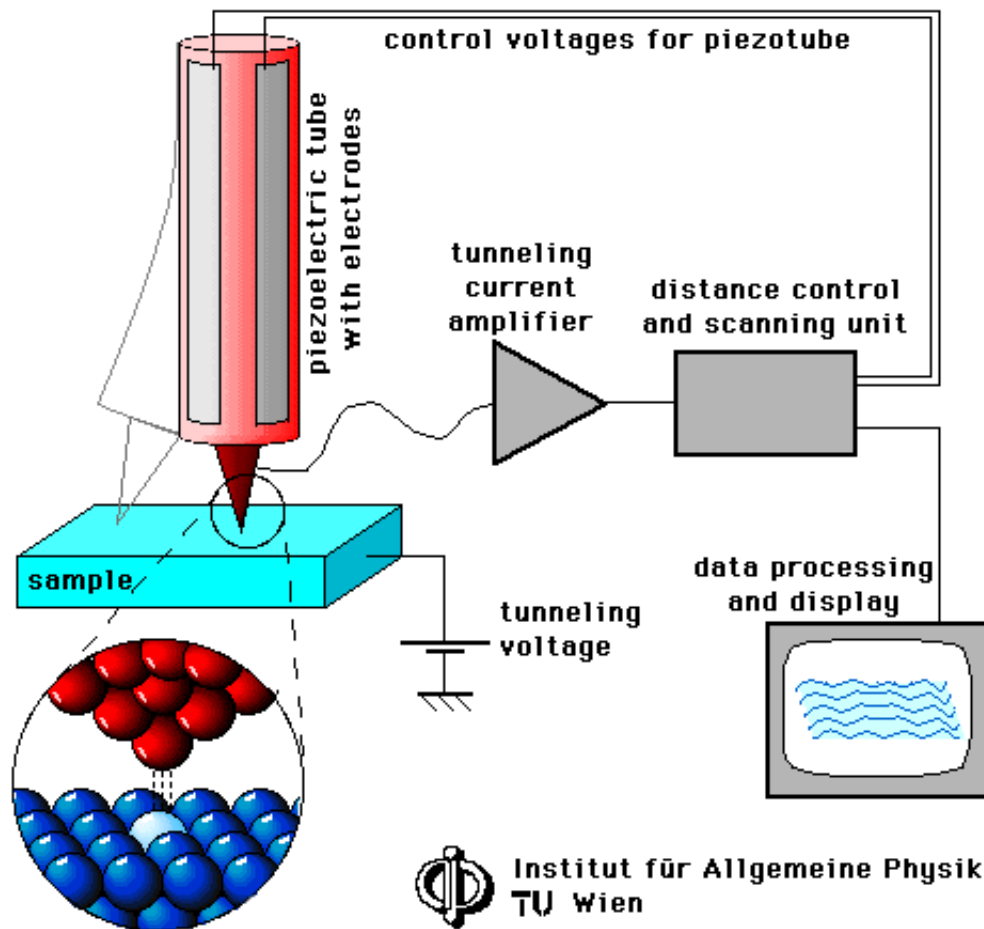


Figure 3.7: STM equipment

where C is a constant. Thus, if a tip is scanned at constant height above a surface the tunnelling current will increase in areas where protrusions exist because of lowering of the gap.

Figures 3.6 and 3.7 illustrate schematically the STM equipment, tips containing a single atom at its apex may be formed by simply cutting a Pt/Ir wire with a sharp pair of scissors. Alternatively, a tungsten wire may be electrochemically etched in an aqueous solution of sodium hydroxide. The tip quality is tested by its ability to produce good atomically resolved images of standard calibrating materials, such as the basal plane of graphite.

Two modes of scanning may be employed, constant height and constant current. In the constant height mode, the tip is scanned in the xy-plane of the surface whilst remaining stationary in the z-direction. This results in variations in the tunneling current associated with changes in W (owing to surface protrusions).

In contrast, for the constant current mode, the value of W is fixed by movement of the tip in the z-direction, while scanning in the xy-plane. Thus a plot of the z-piezo electric voltage versus lateral position will also yield a topographic image of the surface. However, for rough surfaces, the constant current mode is preferred since it avoids tip-surface collisions that would otherwise result in a blunt tip incapable of atomic (or any other) type of imaging.

3.2.4 Synchrotron radiation

Synchrotron radiation is produced when charged particles moving at relativistic velocities are accelerated, an accelerated charged particle emits radiation. Consider a charged particle which is either at rest or in uniform motion through vacuum (i.e. in absence of external electromagnetic fields), this one creates electric field lines that are either at rest or moving uniformly together with the particle; when electric or magnetic fields force it to move with relativistic speeds to follow curved trajectories, they radiate electromagnetic radiation in a narrow cone in the direction of motion as illustrated in figure 3.8.

Synchrotron radiation emitted by electrons in particle accelerators is extremely intense, collimated and extend over a broad energy range from infrared through visible and ultraviolet, into soft and hard x-ray regions of the electromagnetic spectrum.

The most useful and common source is the storage ring that consist of

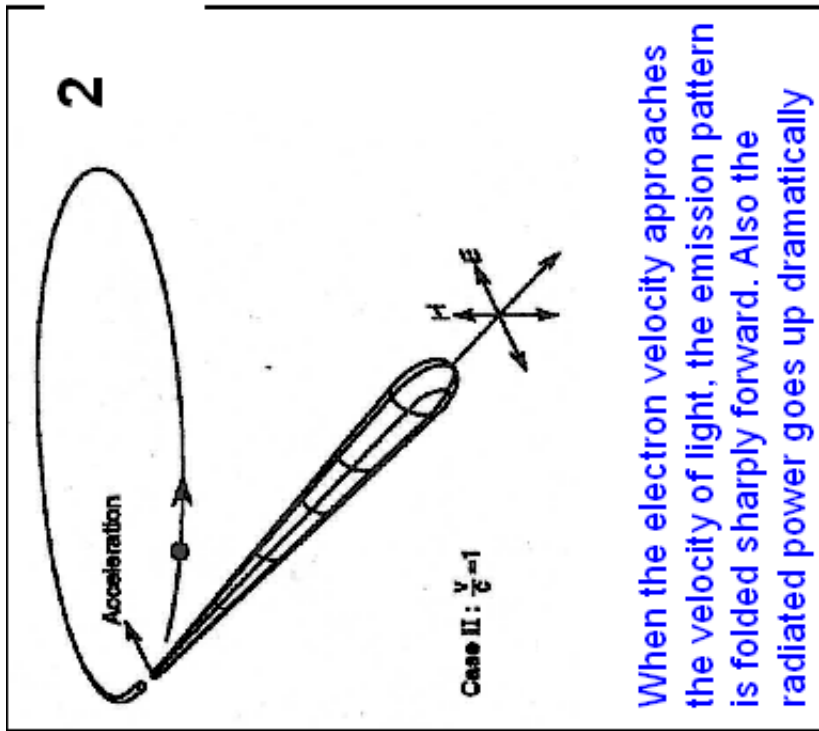
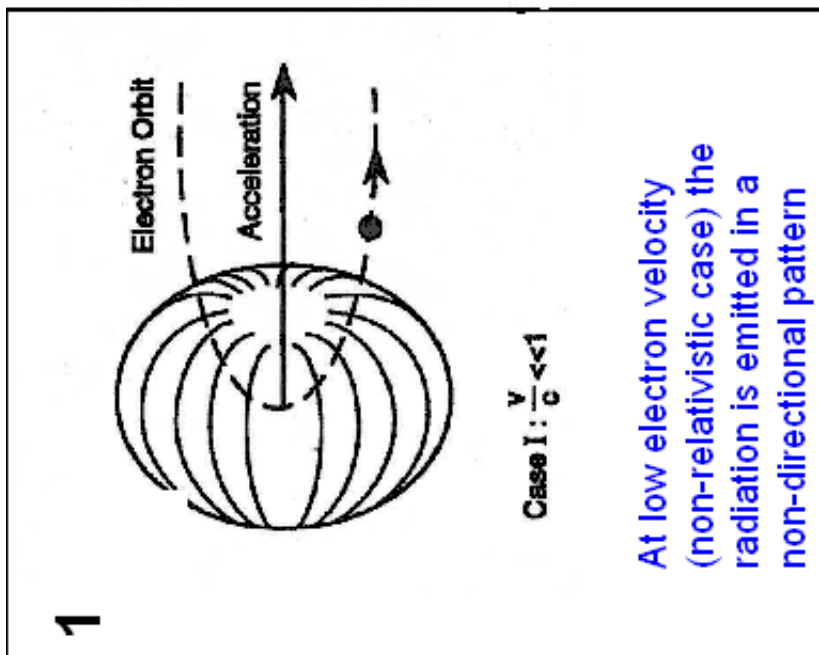


Figure 3.8: 1. When electrons are accelerated (e.g. linear acceleration in a radio transmitter antenna) they emit electromagnetic radiation (i.e., radio waves) in a rather non-directional pattern; 2. Electrons in circular motion are also undergoing acceleration (centripetal).

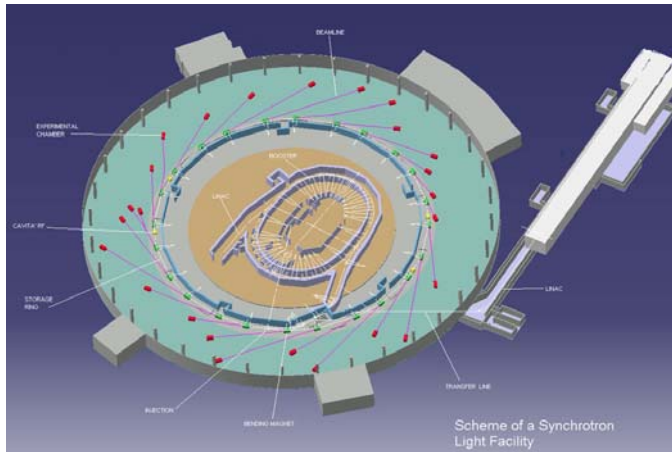


Figure 3.9: A typical storage ring for synchrotron radiation.

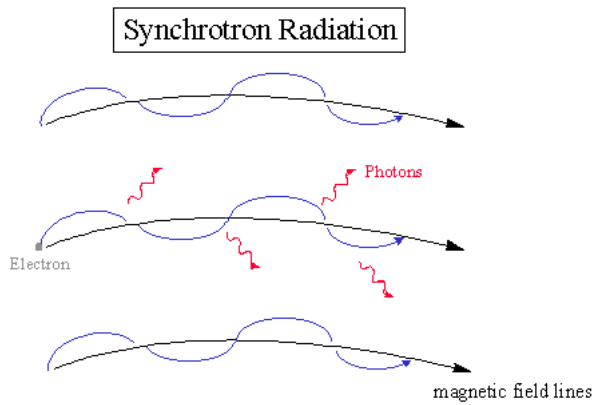


Figure 3.10: A schematic view of synchrotron radiation emission.

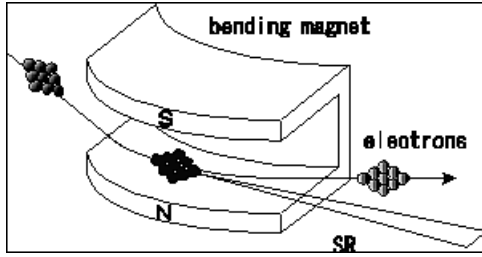


Figure 3.11: A schematic reproduction of a bending magnet.

circular evacuated pipe where electrons are forced to follow circular paths under a magnetic action (bending magnets) and, then, accelerated to higher energies by radio frequency electric fields (RF cavities). In figure 3.9 ELETTRA storage ring is shown.

Bending magnets (figure 3.11) radiation is directed tangentially outward from the electrons trajectory in a narrow cone with an opening angle given by $1/\gamma = mc^2/E_e$, where E_e is the energy of the radiating electron. The radiation spectrum from bending magnets is continuous and very broad analogously to white light.

Insertion devices (ID) are periodic magnetic structures installed in the straight sections of the storage ring to generate more intense synchrotron radiation. Most commonly used are wigglers and undulators (figure 3.12), they consists of permanent magnets or electromagnet array that generate a periodic magnetic field.

Electrons passing through the ID produce a discrete emission spectrum of harmonics whose energy is delimited by the strength of the magnetic field generated by the magnetic arrays. In a wiggler, the magnetic field in the array is so strong, that it bends the electron beam through a large angle compared with the angular width of the natural radiation cone normally associated with

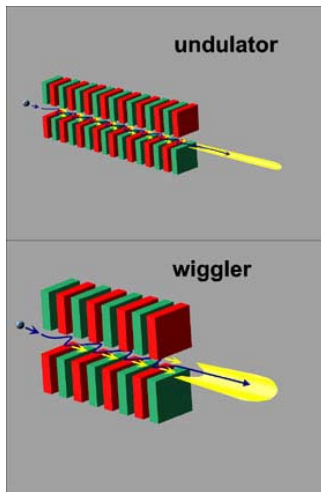


Figure 3.12: Insertion devices: a) Undulator and b) Wiggler.

synchrotron radiation ($1/\gamma$). In a undulator, the magnetic field is relatively weak and the resultant angular path is smaller than mc^2/E_e . Undulator and wigglers may produce linear and circularly polarized light depending on the geometry of the magnetic structure and the observation angle.

Chapter 4

Experimental Apparatus

Dynamics and morphology of growth has been performed in AR-XPS laboratory at ISM - CNR “Tor Vergata” in Rome, Italy; ELETTRA facility provides synchrotron radiation for CDAD measurements and high resolved core and valence band (XPS and UPS) at Circular Polarization (POLAR) and VUV photoelectron beamlines, respectively; STM images were collected using the STM apparatus which is available at Advanced Photoelectric-effect Experiment (APE) beamline.

All the experiments presented were performed in ultra high vacuum chamber. The vacuum conditions for these experiments (base pressure of the order of 1×10^{-10} mbar) were achieved after a careful baking-out of the system and outgassing of the different filaments and of the sample holder, to remove contaminants from vessel surfaces. Pumping of the chambers was obtained with a combination of rotary, turbo-molecular, ion and titanium sublimation pumps.

4.1 AR-XPS Apparatus ISM laboratory

A laboratory XPS apparatus has been used for X-ray photoelectron measurements on Alaninol chemisorbed on Cu(100) and Cu(110) surfaces.

The XPS vacuum system consists of four main chambers and is sketched in figure 4.1:

1) main chamber for XPS is equipped with a X-ray source, hemispherical electron analyzer mounted on a two-axis goniometer to eventually perform angular resolved photoelectron, an electron gun, ionic and titanium sublimation pump;

2) preparation chamber for *in situ* the sample growing, it is equipped with standard tools for cleaning, prepare and characterize surfaces, ion gun for sputtering, a 5 degrees of freedom manipulator with an heater for the sample annealing. Manipulator travels vertically from preparation to main chambers, LEED optics, chemical sample evaporator (figure 4.10) and mass spectrometer to check evaporation. Main and preparation chambers are separated with a gate-valve allowing quick measurement of the dosed surface.

3 and 4) intermediate and introduction chambers to enter in the vacuum up to 14 sample.

Top view of the apparatus is shown in figure 4.1 and two pictures of the equipment follow in figure 4.2.

The hemispherical electron energy analyzer collects electrons and it is able to select the ones with the same kinetic energy and brings them in a counting detector (figure 4.3).

The analyzer consists of two concentric hemispheres of radii R_{in} and R_{out} ($R_{in} < R_{out}$) mounted with a common centre as shown in figure 4.3. A potential V is applied between the spheres so the outer hemisphere has negative

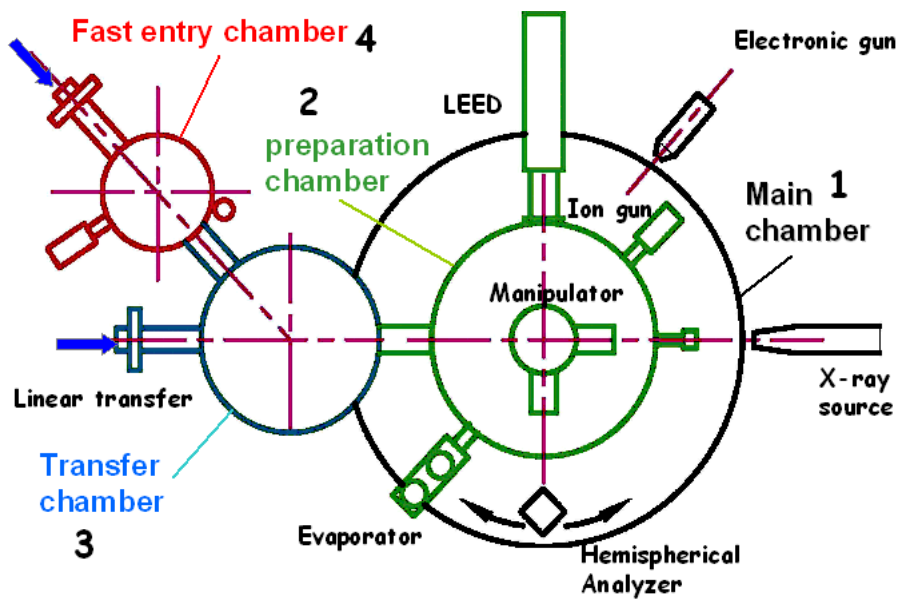


Figure 4.1: An outline of the experimental equipment where all the instrumental tools are indicated.

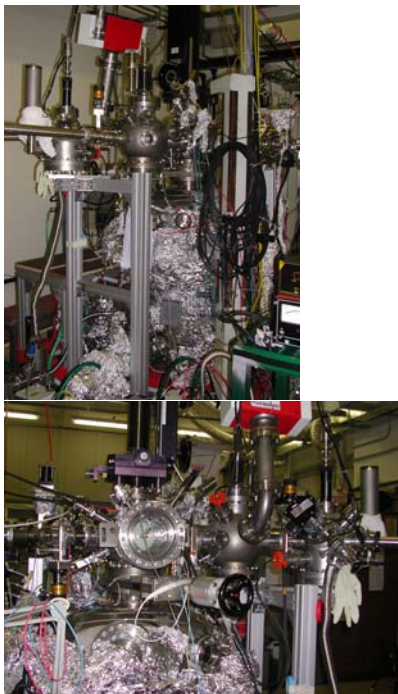


Figure 4.2: Some images of the experimental chambers are presented.

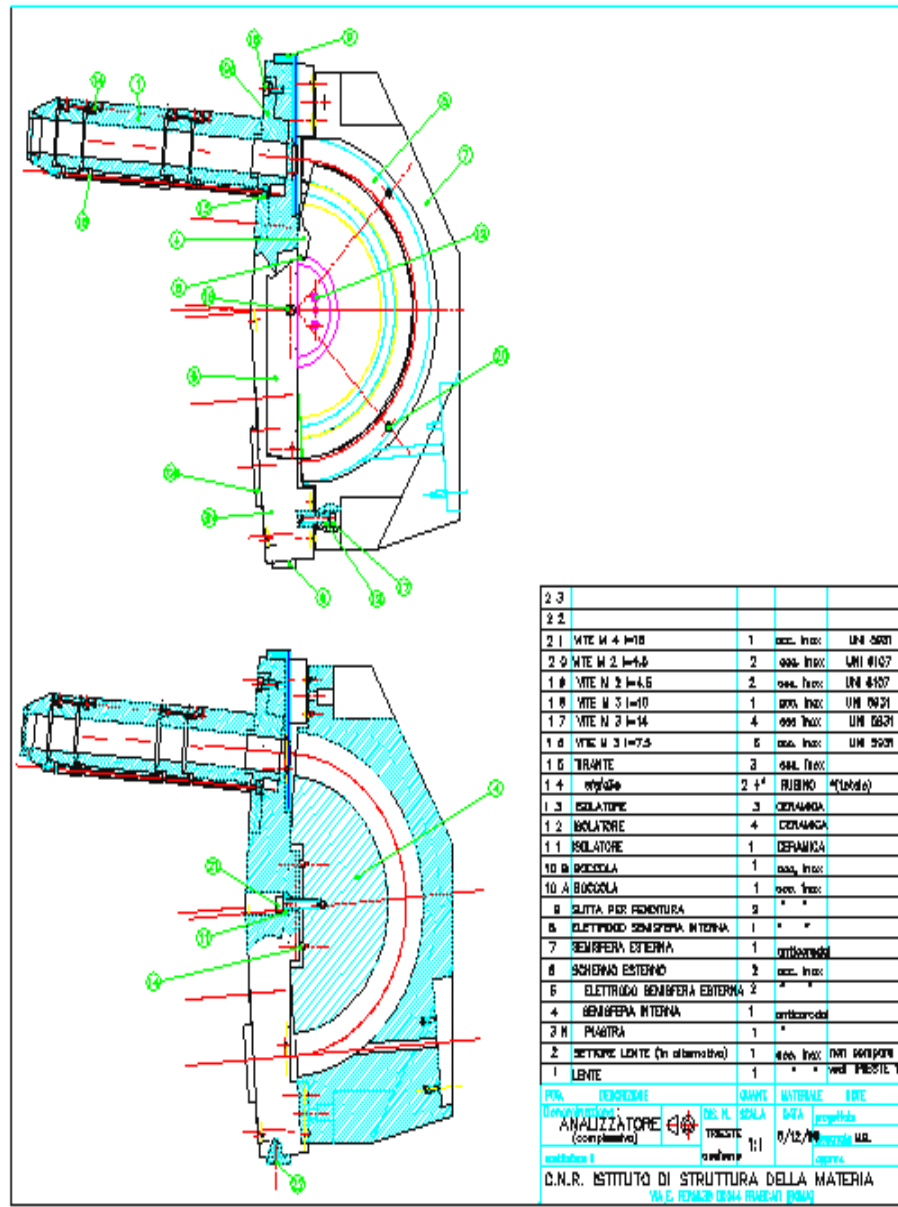


Figure 4.3: Schematic diagram of a hemispherical electron energy analyzer is presented, it is mounted on a goniometer in the main chamber to provide angle-resolved experiments.

potential and the inner one is positive, with respect to V_0 , which is the mean potential surface between the hemispheres. The entrance and exit slits are both centred on R_0 which is the mean radius between R_{in} and R_{out} .

If E_p is the kinetic energy of an electron travelling in an orbit of radius R_0 , then the relationship between E_p and V_0 is given by the expression:

$$eV_0 = E_p \left(\frac{R_{out}}{R_{in}} - \frac{R_{in}}{R_{out}} \right) \quad (4.1)$$

where R_{in} and R_{out} are the radius of the inner and outer hemispheres respectively. The E_p is the Pass Energy (PE).

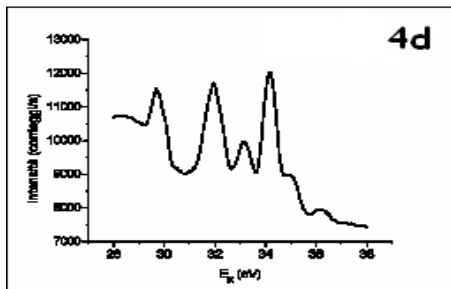
The voltage on the hemisphere is V_i and it is correlated to E_p , R_i (the radius of hemisphere), and R_0 as in the next equation:

$$V_i = E_p \left(2 \frac{R_0}{R_i} - 1 \right)$$

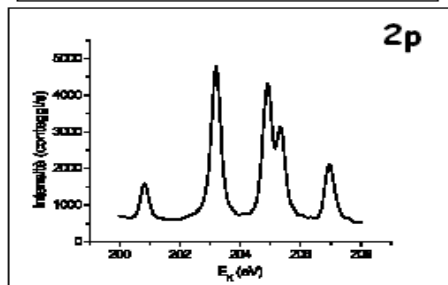
This relationship produces an inverse squared ($1/R^2$) field in the region between the hemispheres.

A series of pre-retardation electrostatic lens system are placed at the entrance of the analyzer to collect iso-energetic electrons and to modify their energy, accelerating or retarding the charged particles, with respect to the pass energy of the analyser. At the exit a channeltron is placed collecting and counting the electrons passed through the analyzer.

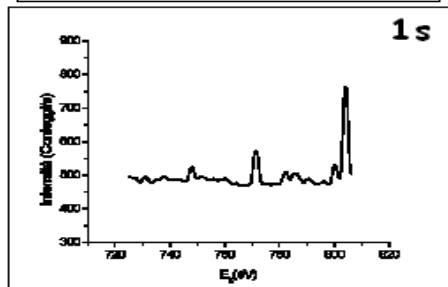
The AR-XPS analyser has been characterized measuring Auger spectrum of Argon, Neon and Xenon that are reported in figure 4.4 and resolution has been estimated as $9 \cdot 10^{-3}$. Since Auger lines correspond to different energy ranges this preliminary experiment was used to calibrate accurately the kinetic energy scale over a wide range.



Xenon
 P : $6.7 \cdot 10^{-6}$ mbar
 E_p : 1000 eV
 PE : 30 eV



Argon
 P : $1.4 \cdot 10^{-5}$ mbar
 E_p : 1000 eV
 PE : 15 eV



Neon
 P : $1.0 \cdot 10^{-5}$ mbar
 E_p : 3000 eV
 PE : 20 eV

Figure 4.4: Characteristic Auger peaks of Xenon, Argon and Neon as function of the kinetic energy at constant pressure (p), incident electron beam energy (E_p) and Pass Energy (PE) are reported. This spectra were collected in order to characterize the AR-XPS hemispherical analyzer and calibrate the kinetic energy scale.

4.2 Circular Polarization Beamline

CDAD measurements of gas phase chiral molecules was performed at “Circular Polarization beamline” taking advantage of circularly polarized low energy radiation (10-30 eV) together with the available gas phase photoemission equipment. Here we report a short description of the insertion device which provides circular polarized light.

4.2.1 Electromagnetic elliptical wiggler (EEW)

The EEW was designed to provide linearly and circularly polarized radiation over a wide range of photon energies, 5-1500 eV, using both undulator and wiggler modes of operation and is shown in figure 4.5[90]. The request for helicity switching led to a fully electromagnetic design which combines the horizontal and vertical periodic magnets into one open-sided structure.

When the electrical parameters correspond to the wiggler mode of operation of the insertion device, EEW operates for different values of the vertical and horizontal magnetic field providing an elliptically polarized radiation and a continuum soft x-ray emission spectrum extending from 40 eV to more than 1000 eV. In addition to the continuum, the EEW emits a spectrum of harmonics in the low photon energy side ($<40\text{eV}$), whose fundamental energy is 4.5 eV when ELETTRA operates at 2.0 GeV. At high harmonic numbers ($n>10$), the series of harmonics merge the continuum emission of the EEW. The degree of circular polarization changes with photon energy in the range from 40% at 8.5 eV to 80% at 575 eV. Full circular polarization condition ($>90\%$) should be achieved when the EEW works as a pure circular undulator i.e. when the horizontal and vertical magnetic fields are equal and less than 0.1T ($B_x=B_y>0.1\text{T}$). Under these conditions the available first harmonic lies in the

photon energy range between 50 eV and 150 eV. Undulator mode of operation of the EEW allows to produce, in addition to the circularly polarized radiation and in the same photon energy range, also linearly polarized radiation with the polarization vector parallel or perpendicular to the orbit plane. In fact switching off the horizontal magnetic field, linearly polarized radiation parallel to the orbit plane is produced, while switching off the vertical coils, the remaining field drive the stored electrons to oscillate in the direction perpendicular to the orbit plane emitting vertical linearly polarized radiation.

In plane linear polarization of the emitted radiation is also available in wiggler mode of operation ($B_x=0$; $B_y=0.5$ T) of the EEW.

The switching of polarization state of the emitted radiation is easily achieved by reversing the horizontal magnetic field, i.e. inverting the current into the horizontal coils. At present modulation of the circular polarization between left and right-hand state is available for wiggler mode of operation, by using a trapezoidal waveform which change the polarization state at 0.1 Hz . The net defined polarization state duration available for measurement is about 4 s. During the switching time (about 1s) dynamic correction are applied to the electron beam stored in order to reduce disturbances to the other users. The correction are applied by means of two independent coils placed at the entrance and exit side of the EEW straight section that are driven following a fast feed forward scheme using a pre-built experimental look-up table.

4.2.2 UPS chamber: CDAD apparatus

The angle resolved photoelectron signals are obtained using an CDAD end-station, equipped with twin hemispherical electron energy analysers set at the magic angle θ_m with respect to the synchrotron light propagation direction

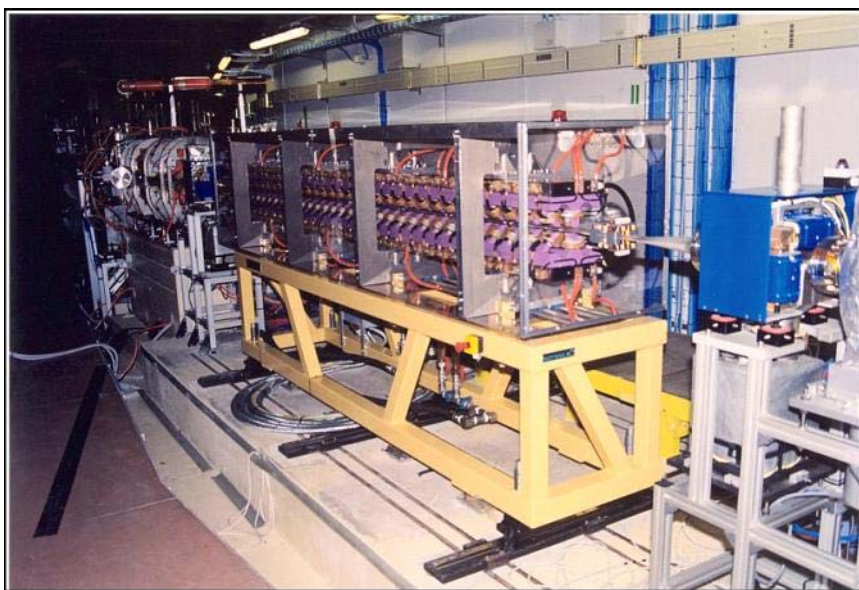


Figure 4.5: Wiggler source at Circular Polarization beamline at ELETTRA, Trieste, Italy.

with 180° angle between them in forward-backward geometry (figure 4.6). The analyzer operates at 25 eV and 15 eV pass energy to have high count rates. The effusive gas source is mounted normal to photoelectron detector and light propagation directions; the sample is introduced in the vacuum chamber via a pipe through a needle (1 mm of diameter), the gas pipe and the source is thermalized with a water recirculation system (around 40°C). The pressure during the experiment is kept dynamically constant at $1 \cdot 10^{-6}$ mbar pumping with a scroll and turbo-molecular pumps.

Electron signal counts is normalized measuring the incident photon intensity by recording the current on the last beamline mirror. Total instrumental energy resolution, analyzers and photon band-pass, is about 200 meV, and the analyzers acceptance angle is $\pm 3^\circ$. The transmission functions and kinetic energy calibrations of the two twin analysers are systematically determined by 3p band photoelectron of Argon (Ar) and C 1s line of carbon monoxide (CO), throughout the experiment.

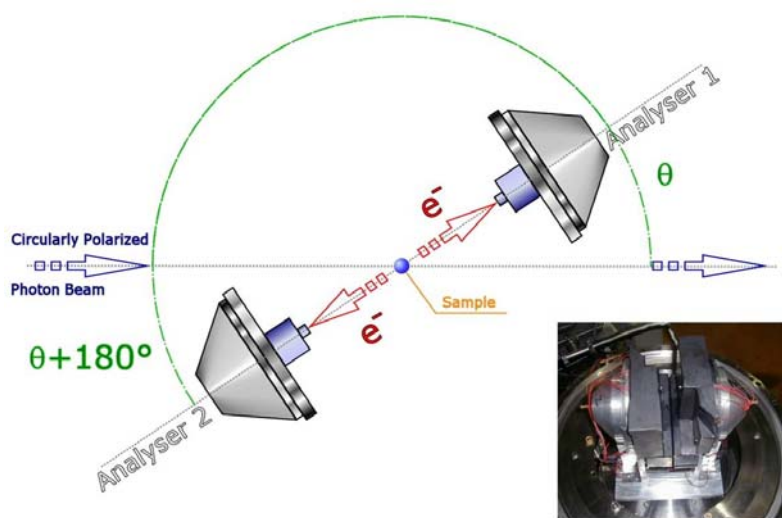


Figure 4.6: Outline of ARPES apparatus at POLAR beamline. Analyzers are placed at θ and $\theta+180^\circ$. In the inset is presented a view of the inside of the chamber, the analyzer can be seen.

4.3 VUV Photoelectron Beamline

VUV photoelectron beamline was used to measure the chemisorbed phase of Alaninol on Cu(100) whose results are presented in chapter 4; this beamline has been designed for surface and solid state experiments involving high resolution photoelectron and some technical details of the beamline are here presented.

The light source is an undulator with a range of 25 eV to 900 eV at electron beam energy of 2.4 GeV.

4.3.1 Experimental set up

The experimental station is equipped with an angle-integrated and angle-resolved electron analyzer and has facilities for sample preparation and fast entry (figure 4.7).

An Omicron EA125 Angle-integrated analyzer was used for this experiment, with an acceptance angle of $\pm 8^\circ$ and it is equipped with five channeltron

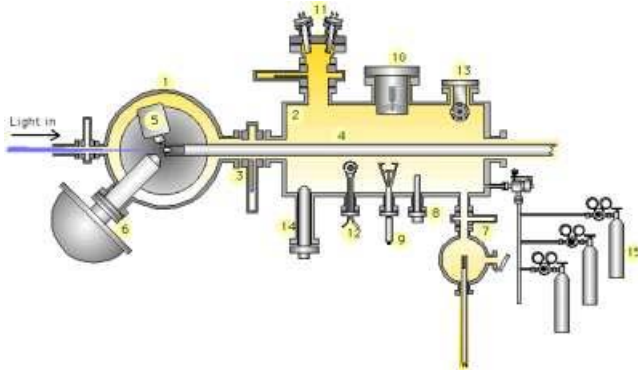


Figure 4.7: Vacuum system

electron multipliers to achieve high count rates.

A horizontal 5 degree of freedom manipulator is available for experiments with a minimum sample temperature of about 100 K.

The preparation chamber is equipped with a fast entry lock system, to interchange samples without breaking the vacuum. Samples are transferred between the preparation chamber and the analysis chamber using the manipulator itself, and they can be heated to about 1300 K or cooled down to 100 K; this chamber guests the evaporators and it also permits sputtering, annealing and LEED detection in the same way as in AR-XPS laboratory.

4.4 STM Apparatus at Advanced Photoelectric-effect Experiment (APE) Beamline

STM images were collected at APE - STM end station (figures 4.8 - 4.9), equipped with LEED system and a room temperature scanning tunneling microscope (UHV-STM) which routinely provides images with atomic resolution.

The base pressure of the chamber is better than 1×10^{-10} mbar with an ion sputtering pump and a Ti sublimation pump. The electronics and software for

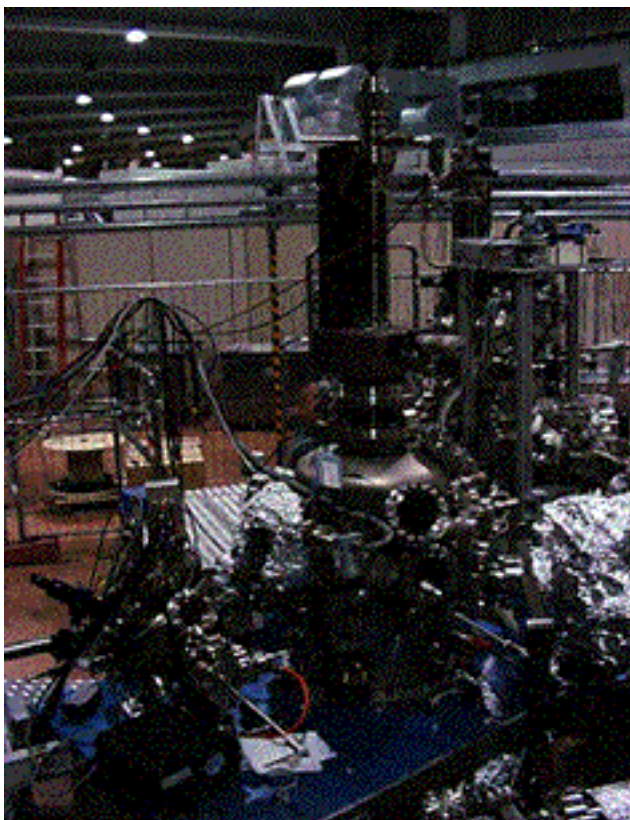


Figure 4.8: STM equipment at APE beamline.

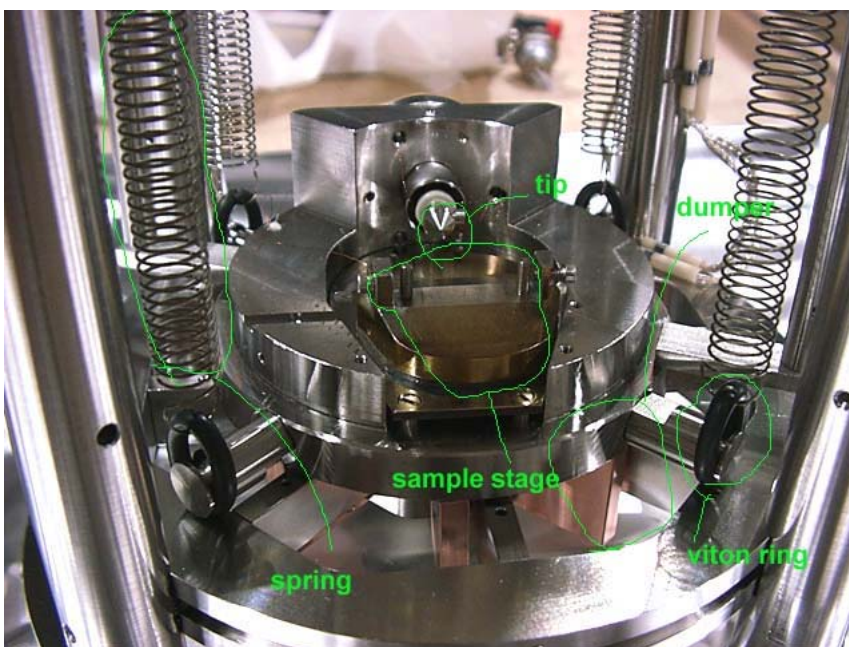


Figure 4.9: STM view in detail.

image acquisition are the products of East Coast Scientific Ltd.

The most important part of STM for obtaining atomically resolved images is an anti-vibration system. The anti-vibration system is composed of two isolators and a damper. The STM stage is suspended by four long metallic springs which cut low frequency vibration noise. There is also one viton ring between the STM stage and each spring as an isolator. The viton ring cuts a high frequency noise. There is an Eddy current damping system below the STM stage in order to attenuate the oscillation of the stage.

The type of approaching system is a slider approaching system. One pulse to the piezo electric element of the slider moves the sample about 100nm. The tip is mounted horizontally and the sample surface is set vertically. The sample holder is staying on the horizontal plane and the slider can move the sample holder in the horizontal plane: forward and backward to the tip, and also to left and right.

The tip is mounted on the piezo electric tube whose scan range is $\pm 300\text{nm}$ for X and Y direction (sample surface in plane) and $\pm 200\text{nm}$ for Z direction, respectively.

The tip-sample bias voltage is supplied to a sample and the tunneling current is measured through the electrode which is connected to the tip. The tunneling current is first amplified by a pre-amplifier ($\times 10^8$) and converted to a voltage and is measured with a 16 bit AD converter. The feedback loop changes the voltage for the piezo electric tube (changes the distance between the tip and the sample) keeping the tunneling current constant.

A W tip is used and it is cut with electrochemical etching (NaOH 1N solution) and cleaned in the UHV chamber by annealing and Ar ion sputtering.

4.5 Sample Preparation: Procedure

D- and L-Alaninol (R-(-) and S-(+)-2-Amino-1-Propanol) are a Sigma-Aldrich product with a chemical purity of 99% and enantiomeric purity of 97%. Alaninol boiling temperature is $T_{\text{boil}}(1 \text{ atm}) = 72^{\circ}\text{C}$ and is liquid at room temperature. No treatments are performed before entering the vacuum but few hours are needed to free the sample from H_2O , that is the main contaminant, this cleaning is made in a separate chamber pumping the sample and checking the residual vacuum with a mass spectrometer.

The method used for obtaining a clean copper surface, is argon ion bombardment. This method consists of the physical removal of surface material by bombardment of the surface with a beam of high energy argon ions (commonly 1000-2000 eV). Upon striking the surface, energy and momentum transferred from the argon ions to the substrate causes surface atoms to break their bonds with the substrate and desorb into the vacuum (this is called sputtering). Because of the nature of the process, argon ion bombardment leaves a pitted and rough surface. Therefore, annealing of the substrate to 400°C is essential, both to facilitate surface diffusion (and hence the removal of defect sites so that a flat, clean surface is produced) and, also, to desorb argon atoms embedded in the substrate itself. Argon etching needs to be repeated for several cycles, since annealing leads to segregation of impurities from the bulk of the sample to the surface. Clean surface was checked monitoring the most common contaminants, such as C 1s and O1s lines, by photoelectron or Auger spectroscopies.

After cleaning the surface and outgassing the organic sample, deposition can be performed, Alaninol enters, through a leak valve and the evaporator reported, in figures 4.10 and 4.11, into the preparation chamber.

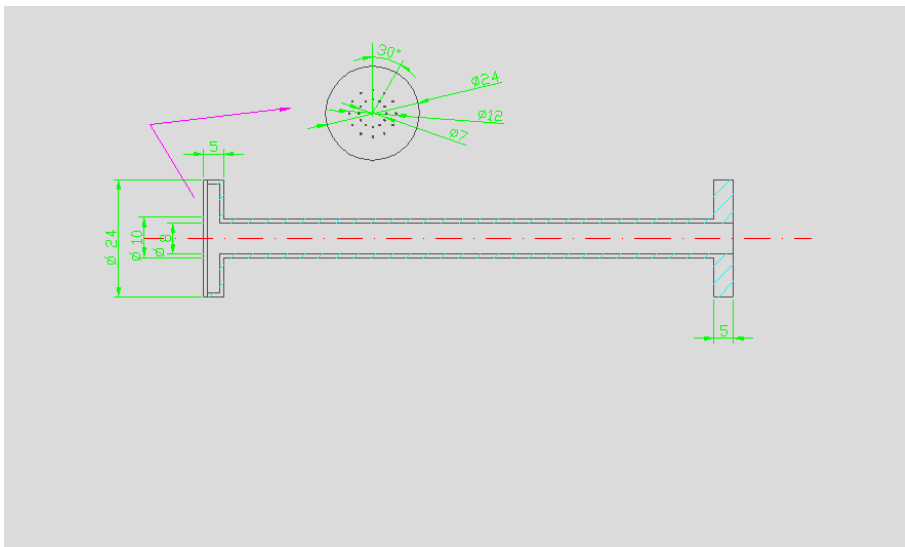


Figure 4.10: Evaporator outline: a stainless steel tube with at one limit a “shower”; vapour sample flows trough the holes, shown in the inset into the vacuum, the other end is weld on a flange connected to a leak valve, a linear travel allows to move the evaporator close to the surface.

(a)



(b)

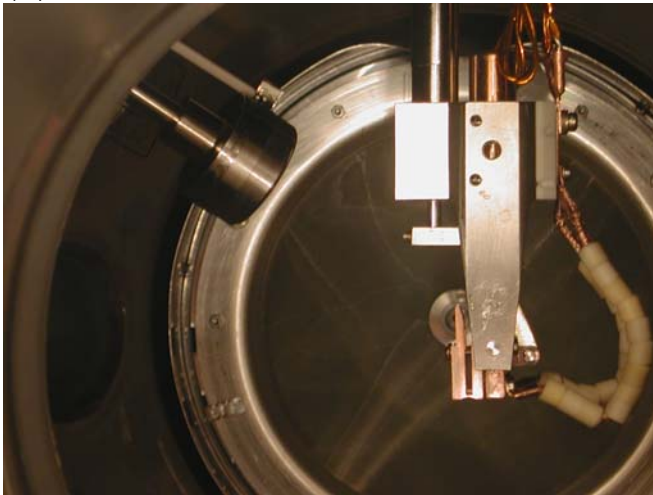


Figure 4.11: Pictures of the evaporator itself (a) and mounted on the preparation chamber at ISM laboratory in Roma (b). In (b) the manipulator is also shown.

Chapter 5

Circular Dichroism in Angle

Resolved Photoelectron

Spectroscopy in Gas Phase: D-

and L-Alaninol

Chiral discrimination is at the base of recognition processes, this pervades nature and can be investigated by means of circular dichroism (CD) in photoelectron spectroscopy as previously described. This technique allows to characterize the chiral properties asymmetric molecules with the unique chance to investigate the connection between structural and electronic properties with dichroic effects with subsequent important involvements in the understanding of the origin of homochirality and the interaction of asymmetric biological and catalytical active molecules with circularly polarized light. In this chapter photoionization spectra and CDAD studies of Alaninol free molecule are presented.

5.1 Photoelectron Spectroscopy of L-Alaninol in Gas Phase

Studies turned toward gas phase represents an interesting tool to understand fine molecular mechanism in the gas phase as those involved in molecular recognition. For these results chiral properties have been investigated with CDAD.

The valence electronic structure and C 1s core line of S-(+)-2-Amino-1-Propanol (L-Alaninol) have been studied experimentally by synchrotron radiation photoelectron spectroscopy (PES) in the gas phase; the investigated system is a reduced derivative of alanine but more stable and so it is a good model for aminoacid-like structures. The experimental results are interpreted with the help of theoretical calculations: the ionization potentials have been predicted at DFT level and compare with measured values. In all the spectra in this section successive scans recorded with right- and left-circularly polarized light are summed together to cancel any residual intensity variations which arise with an enantiomerically pure molecular sample. Set-up has been presented in section 4.2, it is the same as for circular dichroism in angular distribution (CDAD) measurements shown in the next section.

Computational details The ground state equilibrium geometry and ionization potentials have been computed by *ab initio* density functional (DFT) calculation with the standard 6-31G** basis set using Gaussian 03 code [91].

Amino alcohols present several conformations in isolated conditions which have been recently studied and classified by Fausto et al. [10]. Poor literature is available [9], and in this, theoretical methods, mostly used, are MP2 or DFT, the latter was, then, chosen since it considers electron correlation describing

better this molecular system.¹

IE's values are computed with Koopman's theorem [92], the exact Kohn-Sham eigenvalue of the highest occupied molecular orbital (homo) corresponds, with opposite sign, to the ionization potential (IE). Kohn-Sham eigenvalues of inner orbitals are actually approximations to the IEs and, therefore relative ionization energies are meaningful [93]. Kohn-Sham orbitals energy underestimate the experimental values, for this reason results are generally shifted in energy.

An hybrid functional, B3LYP, which includes a mixture of Hartree-Fock exchange with DFT exchange-correlation, has been used. Becke's 3 parameter functional [94] with this form was chosen:

$$A * E_x^{Slater} + (1 - A) * E_x^{HF} + B * \Delta E_x^{Becke} + B * \Delta E_c^{VWN} + C * \Delta E_c^{non-local},$$

where the non-local correlation is provided by LYP² [95, 96] and VWN³ expressions [97]. The constant A, B and C are those determined by Becke by fitting to the Gaussian-1 database of Pople and coworkers [94]. LYP includes

¹In Hartree-Fock theory, the energy has the form:

$$E_{HF} = V + \langle hP \rangle - 1/2 \langle PJ(P) \rangle - 1/2 \langle PK(P) \rangle$$

where V is the nuclear repulsion energy, P is the density matrix, $\langle hP \rangle$ is the one-electron (kinetic plus potential) energy, $1/2 \langle PJ(P) \rangle$ is the classical coulomb repulsion of the electrons and $-1/2 \langle PK(P) \rangle$ is the exchange energy resulting from the quantum (fermion) nature of electrons.

In density functional theory, the exact exchange for a single determinant is replaced by a more general expression, the exchange-correlation functional (Kohn and Sham), which can include terms accounting for both exchange energy and the electron correlation which is omitted from Hartree-Fock theory:

$$E_{KS} = V + \langle hP \rangle + 1/2 \langle PJ(P) \rangle + E_x[P] + E_c[P]$$

where $E_x[P]$ is the exchange functional and $E_c[P]$ is the correlation functional.

Hartree-Fock theory is really a special case of density functional theory, with $E_x[P]$ given by the exchange integral $-1/2 \langle PK(P) \rangle$ and $E_c = 0$. The functionals used in density functional are integrals of a function f of the density and the density gradient, such as:

$$E_x[P] = \int f(\cup \rho \alpha(r), \rho \beta(r), \nabla \rho \alpha(r), \nabla \rho \beta(r)) dr$$

An hybrid methods support exchange functional as linear combination of the Hartree-Fock exchange and a functional integral of the above form.

²Lee, Yang and Parr correlation functional.

³Vosko, Wilk and Nusair correlation functional, it fits the Random Phase Approximation (RPA) solution to the uniform electron gas, often referred to as Local Spin Density (LSD) correlation; from paper [97] the functional used is III.

both local and non local terms so the correlation functional used is actually: $C * E_c^{LYP} + (1 - C) * E_c^{VWN}$. In other words, VWN is used to provide the excess local correlation required, since LYP contains a local term essentially equivalent to VWN [97].

Five different conformational states have been observed in matrix-isolation infrared spectroscopy (MI-IR) in Ar and Kr and their relative total energy was evaluated with *ab-initio* (6-31G* at MP2 levels of theory), these are found to represent 95% of the total predicted population assuming a Boltzmann distribution. The first and the second lowest energy forms exhibit a strong intramolecular hydrogen bonding (OH...N), the other three are characterized by a weaker intramolecular bond (NH...O). The conformational preference of alaninol can, however, be modified by the surroundings, for example in liquid phase, resulting in a competition between intra- and intermolecular OH...N interactions. Computational analysis for this work has been performed only for the conformer with the minimum total energy and predominant at room temperature, a complete study could be done in the future.

Valence photoelectron spectra Experimental valence band structure of L-Alaninol, reported in figure 5.1, was recorded at incident photon energy of 50 eV.

The spectrum is characterized by two resolved lower states, an unconvoluted band and five resolved lines at higher energy, no more states appear at higher photon energy. Ionization potentials (IE) of the deconvoluted peaks are reported in table 5.1, these values come from a fitting procedure using Voigt functions (see figure 5.1).

The discrepancy of experimental ionization energy (IE) of the HOMO orbital (labelled 21 in figure 5.2) and the computed value is of 3.2 eV, so all the

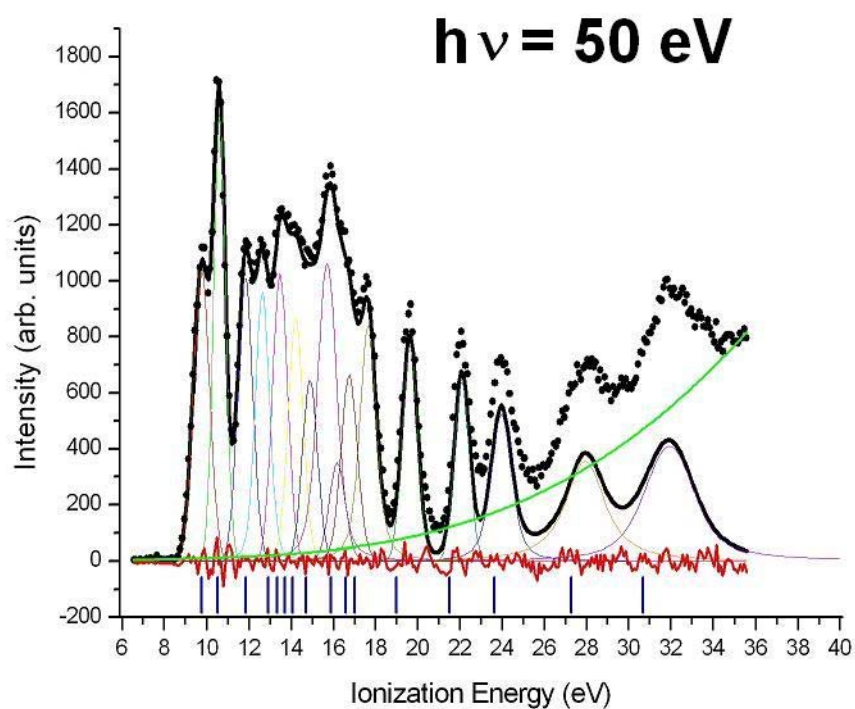


Figure 5.1: Photoionization spectrum of Alaninol recorded at 50 eV; black spots are the experimental results, background and all 16 components are shown, residuals of the fit are presented in red at the bottom ; bars represent computed IEs.

MO	IP(eV)	IPcalc(eV)
21	9.75	9.75
20	10.60	10.50
19	11.82	11.86
18	12.64	12.90
17	13.47	13.33
16	14.21	13.69
15	14.89	14.07
14	15.71	14.7
13	16.18	15.90
12	16.76	16.59
11	17.65	17.02
10	19.62	18.98
9	22.10	21.51
8	23.97	23.64
7	27.95	27.30
6	31.94	30.69

Table 5.1: IEs for 16 valence states from experimental spectrum and DFT evaluation. Molecular Orbital labels (MO) are those in figures 5.2 and 5.3.

computed IE have been shifted up to this amount and, then, reported in figure 5.1, as bar diagram, and summarized in table 5.1. These are derived as the negatives of the MO eigenvalues of the DFT evaluation taking the molecule at the equilibrium geometry.

It can be seen that the two outer-states are estimated from the calculation in agreement with the experimental IEs, getting inner this harmony becomes less and less satisfactory as indicative of the increased importance of electron correlation for these deeper lying orbitals.

Computational details permits to assign the orbitals. From figures 5.2 - 5.4, where computed molecular orbital iso-surfaces are reproduced. It can be observed that the lower states 21 (HOMO) and 20 are the non-bonding orbitals of nitrogen and oxygen respectively, while the other orbitals appear to be delocalized on the molecule.

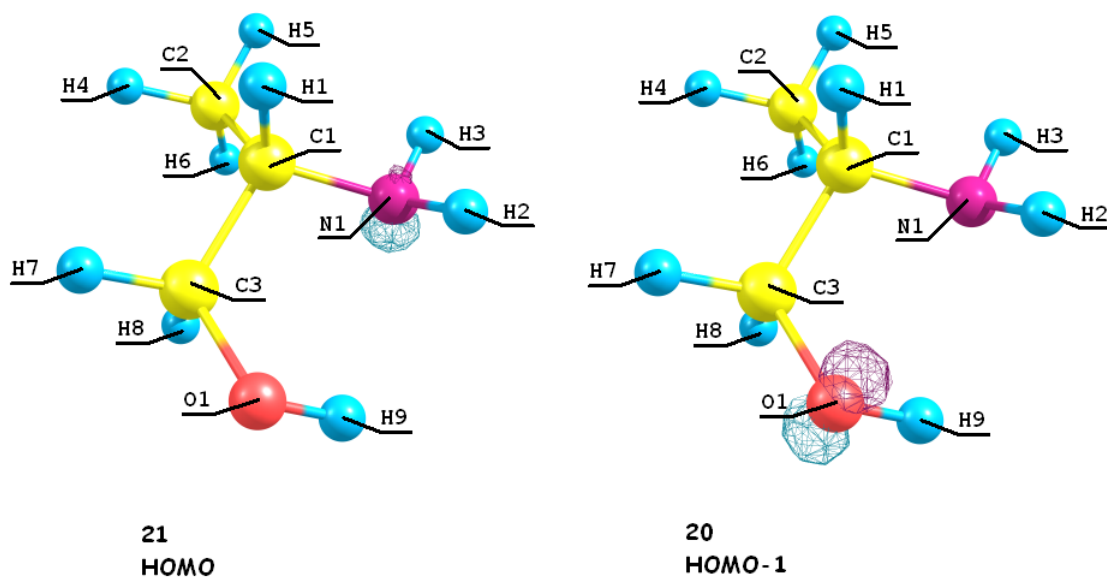


Figure 5.2: DFT/6-31G** Molecular orbitals representation. 21 is HOMO, mostly p_z character, located on the lone pair of nitrogen atom and 20 is HOMO-1, mostly p_z and p_x character, located on the lone pairs of oxygen atom.

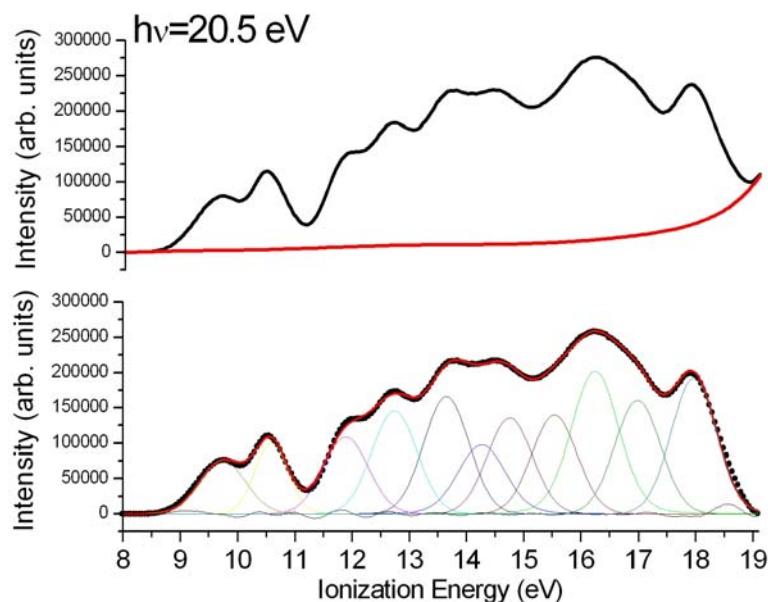


Figure 5.5: Photoionization spectra of Alaninol recorded at 20.5 eV; First panel: black lines are the recorded spectra and red lines indicate the background to be subtracted. Second panel: black spots are spectra subtracted, red line is the fit reproduction and colored lines shows the components for each band, residuals from the fit are displayed in the black thin line.

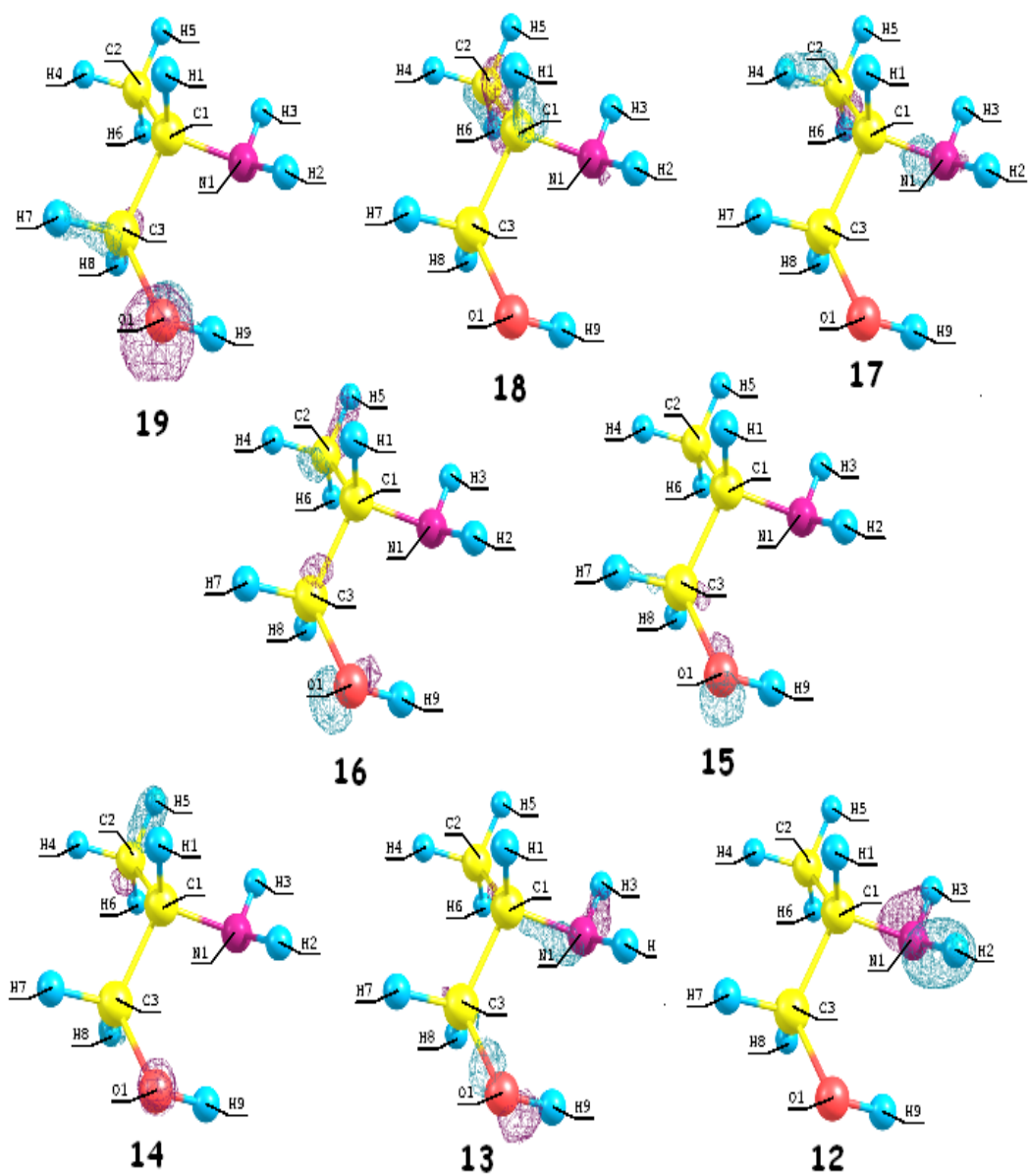


Figure 5.3: DFT/6-31G** Valence orbitals for the minimum energy molecular structure. The orbital labeling indicates the relative ordering of Ionization Energy and is the same as in table (continue...)

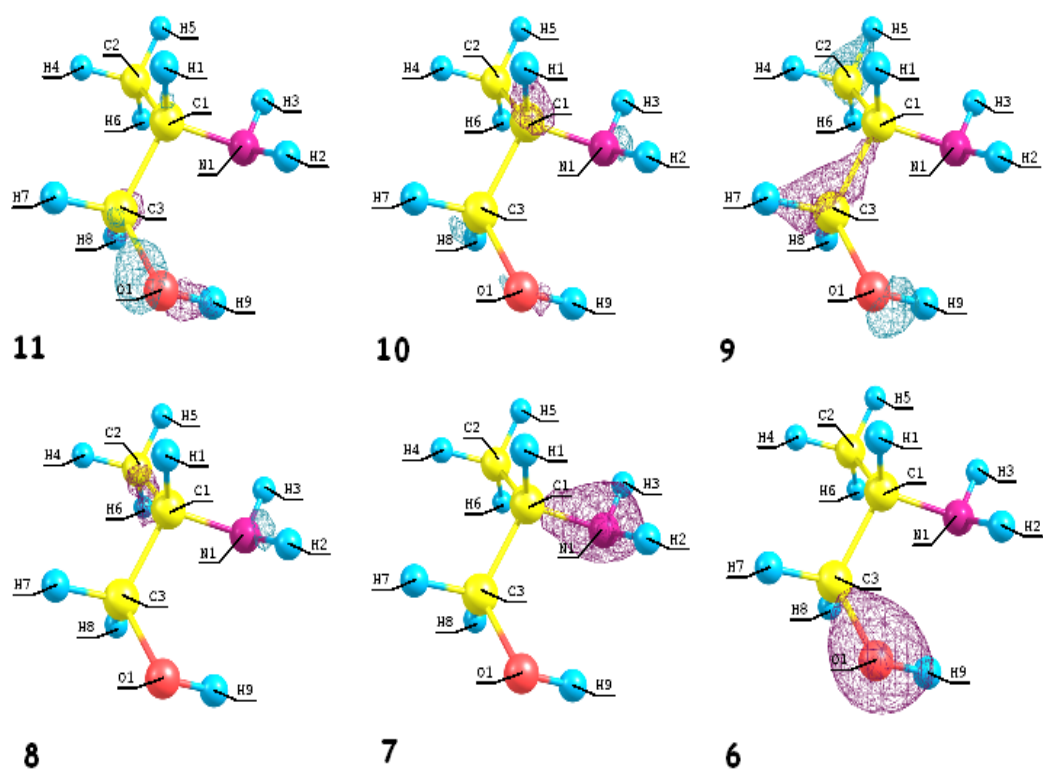


Figure 5.4: (...continue) DFT/6-31G** Valence orbitals for the minimum energy molecular structure. The orbital labeling indicates the relative ordering of Ionization Energy and is the same as in table .

Photoelectron spectra were recorded also at several photon energy in the range $h\nu = 16.6 - 28.5$ eV (figures 5.5-5.8) with the monochromator entrance and exit slits setting of $200 \mu\text{m}$, and analyzer pass energy at 15 eV for $h\nu = 50$ eV (fig.5.1) and at 25 eV for spectra reported in figures 5.5-5.8 corresponding to an estimated overall resolution of 300 meV. The energy scale of the analysers shown in figures 5.1 and 5.5-5.8 was calibrated by introducing Argon into the chamber and recording a photoelectron spectrum of 3p atomic states at each photon energies.

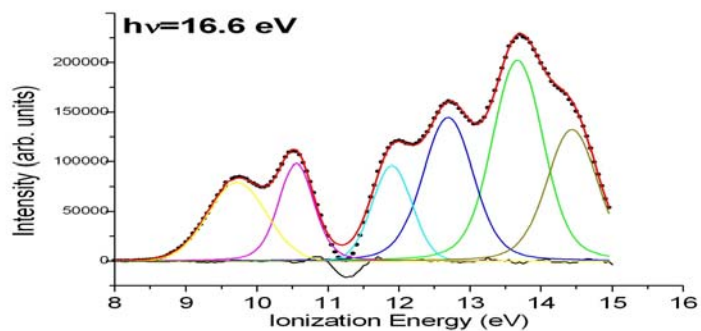
At photon energy higher than 20 eV outer-states still appear intense, almost of the same order of the adjacent broad band indicating a significant oxygen and nitrogen atomic 2p character, associated with these orbitals.

All the spectra are normalized to the incident photon flux measuring photoelectron current collected at the gold surface of the focusing mirror.

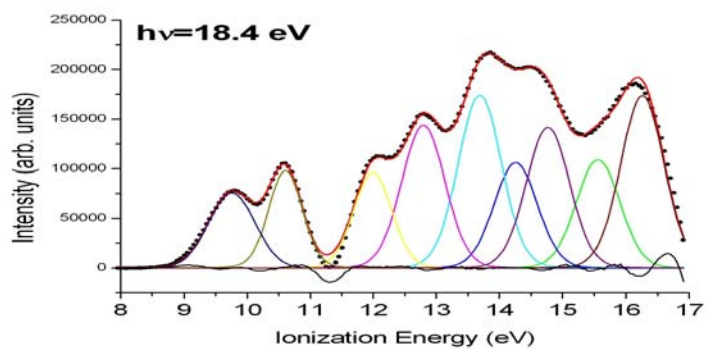
Background signal due to the secondary photoelectrons from the needle, shown in figures, was measured before and after introducing the sample for each photon energy and then interpolate with a polynomial spline and, finally, subtracted.

Comparison of gas-phase investigation of Alaninol with Alanine performed by Powis et al.[98] shows an interesting similitude of IE's values, spectrum shape and orbital assignment (figure 5.9 from this reference). This support the use of amino-alcohols as aminoacid-like samples especially for next dichroic studies.

(a)



(b)



(c)

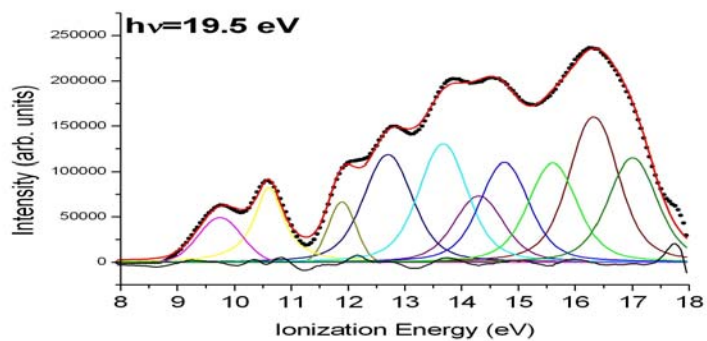
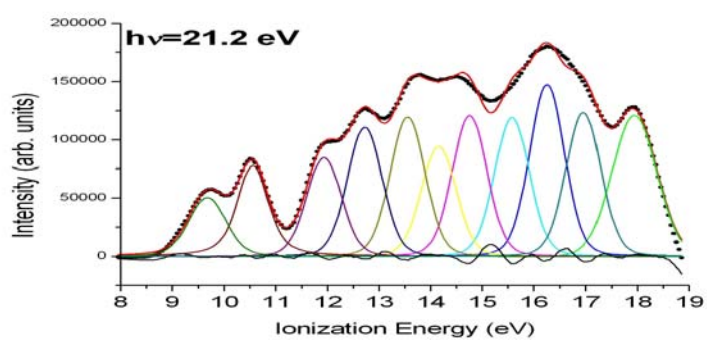


Figure 5.6: Photoionization spectra of Alaninol recorded at a) 16.6 eV, b) 18.5 eV and c) 19.5 eV after background subtraction as in figure 5.5 (continue ...).

(d)



(e)

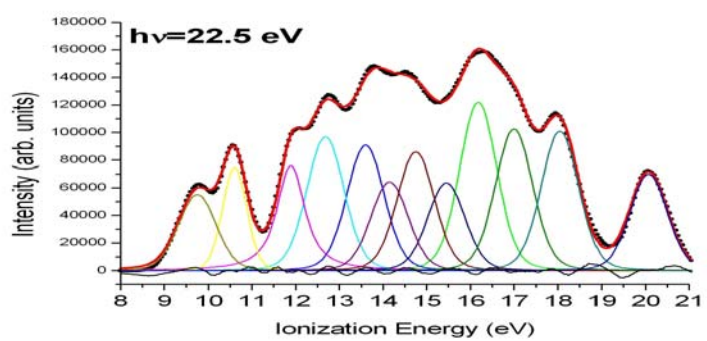
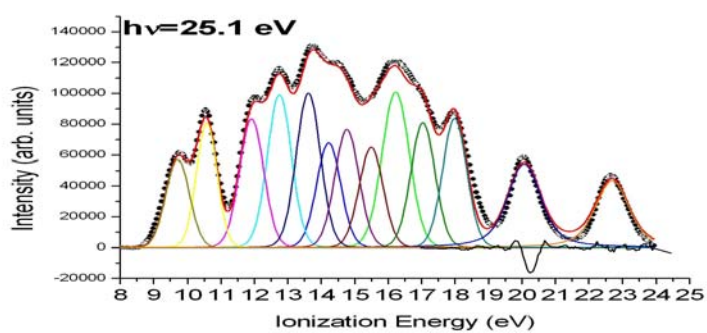


Figure 5.7: (... continued) Photoionization spectra of Alaninol recorded at d) 21.2 eV, e) 22.5 eV after background subtraction as in figure 5.5.

(f)



(g)

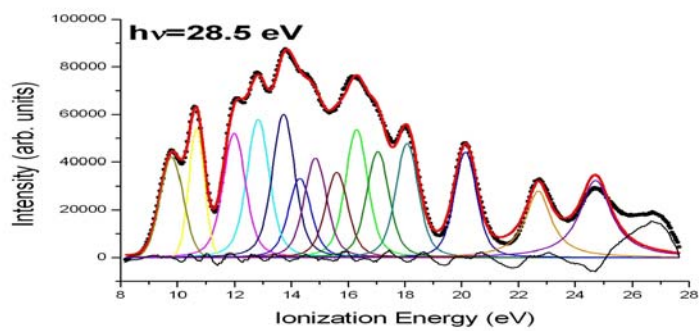


Figure 5.8: (... continue)Photoionization spectra of Alaninol recorded at f)25.1 eV and g) 28.5 eV after background subtraction as in figure 5.5.

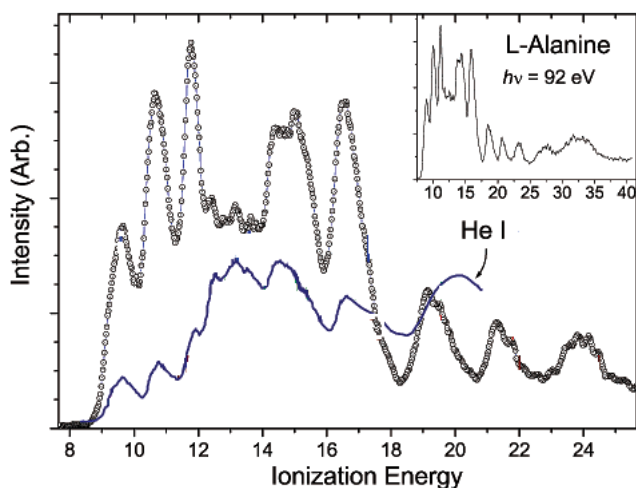


Figure 5.9: Alanine measured at $h\nu=92$ eV by Powis et al.[98]. The inset shows a full-range scan including the complete inner-valence region. A He I spectrum is included [99].

C 1s core spectrum The C 1s experimental photoelectron spectrum of D-Alaninol recorded at 310 eV of incident photon energy together with the best fit performed with three Voigt functions are presented in figure 5.10.

The ionization energies, amplitudes and widths of the three Voigt functions were chosen equal for all the components. The background, residuals and calculated bar diagram for the three non-equivalent carbons are also reported to allow an easier interpretation of the experimental results.

The experimental spectrum appears as a broad band, the fit procedure provides binding energy for the three carbons which are resumed in table 5.2 together with computed IE values. A arbitrary offset of the Koopman's energies has been applied to align the theoretical and experimental peak positions to an approximate coincidence.

Assignment of each carbon has been done with the help of theoretical calculation (see previous paragraph) and is shown in figure 5.11. -C(-O) is the one at higher ionization energy (292.1 eV), the middle one (291.4 eV) is -C(N...)

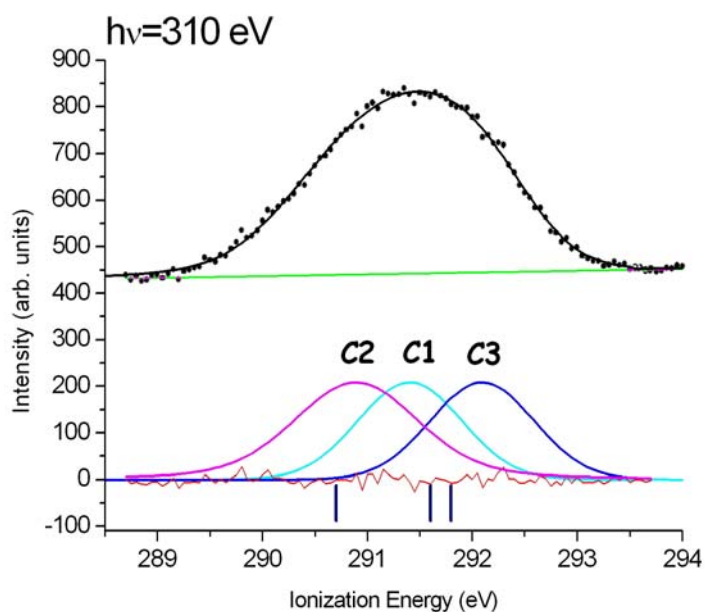


Figure 5.10: Experimental spectrum of C 1s core line of Alaninol (black spots) recorded at 310 eV; with fit, three inequivalent components, background, residuals; blue bars represent computed IEs.

and finally methyl group carbon has lower ionization energy (290.7).

This assignment is also in good agreement with previous studies of gaseous ethanol [100], 2-Butanol [101], alanine [98], glycine [102, 103] and other aminoacids [104], where $E_b = 291.83$ eV is assigned to $-C(OH)$, whereas $-C(-N)$ lies at $E_b = 292.3$ eV, $-CH_3$ at $E_b = 291.2$ eV and $-C(-OO)$ at $E_b = 295.3$ eV.

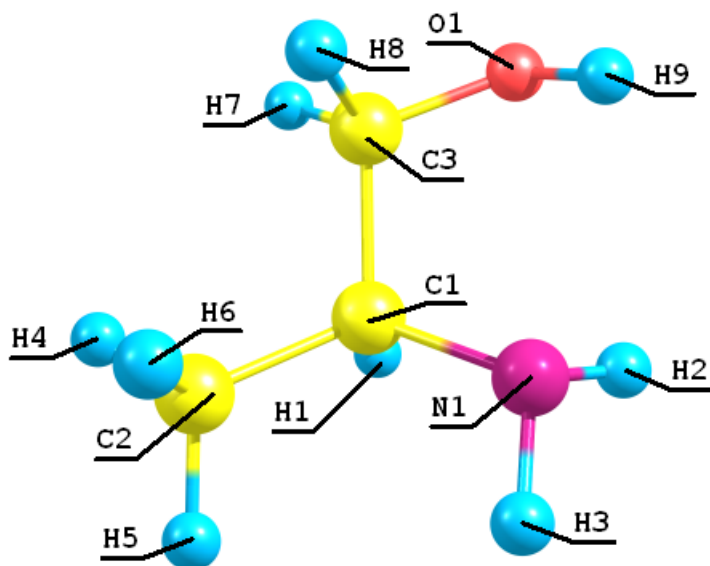


Figure 5.11: Equilibrium structure of L-Alaninol with all atoms labelled.

Atom	$IE_{\text{exp}}(\text{eV})$	$IE_{\text{DFT}}(\text{eV})$
C2	290.7 (0)	290.7 (0)
C1	291.4 (0.7)	291.6 (0.9)
C3	292.1 (1.4)	291.8 (1.1)

Table 5.2: IE_{exp} from the fit and computed IE_{DFT} of the three non equivalent carbons shown in figure 5.10 are reported. Carbons are labelled as in figure 5.11 and the relative energy to the lowest value is shown in parenthesis.

A good overall agreement is found even if in the theoretical treatment is not considered the molecular relaxation due to the ionic environment of the final state, that is, the state left back from the ejected photoelectron.

5.2 Circular Dichroism (CDAD) of D- and L-Alaninol

The photoionization process of randomly oriented molecules in the gas phase is described, at one-particle level, with each orbital corresponding to a line in

the photoelectron spectrum, by the expression 3.4 which describes the angle-dependent differential cross-section that, at fixed detection angle, depends on three energy-dependent parameters (σ , β and D) which are molecular properties. When the light is linearly polarized the term dependent on D vanishes since $m_r=0$ and the coefficient of the second Legendre polynomial is β . In the presence of circularly polarized light ($m_r=\pm 1$) the term dependent on D gives a contribution which changes sign according to the sign of circular polarization and dichroism effect arise. Moreover, $D \neq 0$ only when the molecule is chiral as can be found in Ritchie [87]. At a special detection angle called “magic angle”, $\theta=54.7^\circ$, using circular polarization light the term containing β vanishes, so intensity is only related to the photoionization cross-section and the dichroic parameter D .

Valence photoelectron spectra of the enantiomers of L-Alaninol (S-(+)-2-Amino-1-Propanol) have been recorded at different photon energy in the range 16.6-25.1 eV, and have been presented in the previous section. Spectra were taken using left and right polarized light and collected at two analyzer site at $\theta=54.7^\circ$ (magic angle) from the light propagation direction and $\theta+180^\circ$, that is, backward and forward detection angles and corrected for the amount of the circular polarization. Test measurements have been accomplished by checking for sign reversal of dichroic effect by enantiomer exchange and backward-forward detection angle swap.

D parameter was estimated for each state, the valence spectra was fitted as displayed in figure 5.5, the same Voigt functions were used to reproduce the difference spectra (I_+-I_-) by leaving the amplitude as a free parameter, keeping fixed peak positions and widths. The D_i coefficient for a selected channel is obtained using the photoelectron peak area obtained with two different helic-

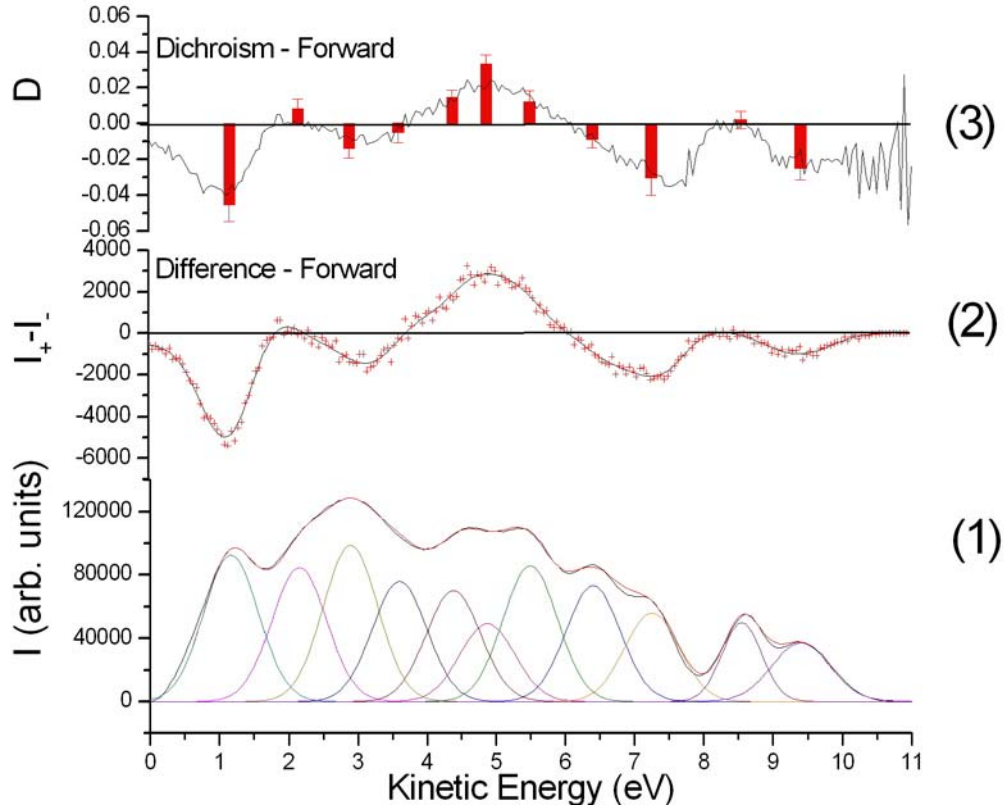


Figure 5.12: Procedure used to determine D for each line in the PES spectrum: (1) PES spectrum for left and right plane rotation recorded at 20.5 eV at forward detection with fit and components as in figure 5.5 d); (2) Difference ($I_+ - I_-$) and fitting procedure; (3) $\frac{A_{CDAD}}{\cos\theta_m}$ along the spectrum and, in red bars, D_i for each band are displayed.

ities. Several sets of spectra have been recorded for each photon energy value by switching light helicity thus allowing to estimate the experimental uncertainty of the measured dichroism coefficient which is reported as error bar in the figures. In figure 5.12 procedure to estimate D is illustrated, I_+ and I_- are the intensity of spectra taken at left and right circular polarization of the radiation respectively.

Figure 5.13 reports the asymmetry A_{CDAD} obtained from sequential measurements with both helicity for L-alaninol taken at 19.5 eV photon energy at the magic angle using the two analyzer placed in the backward and forward

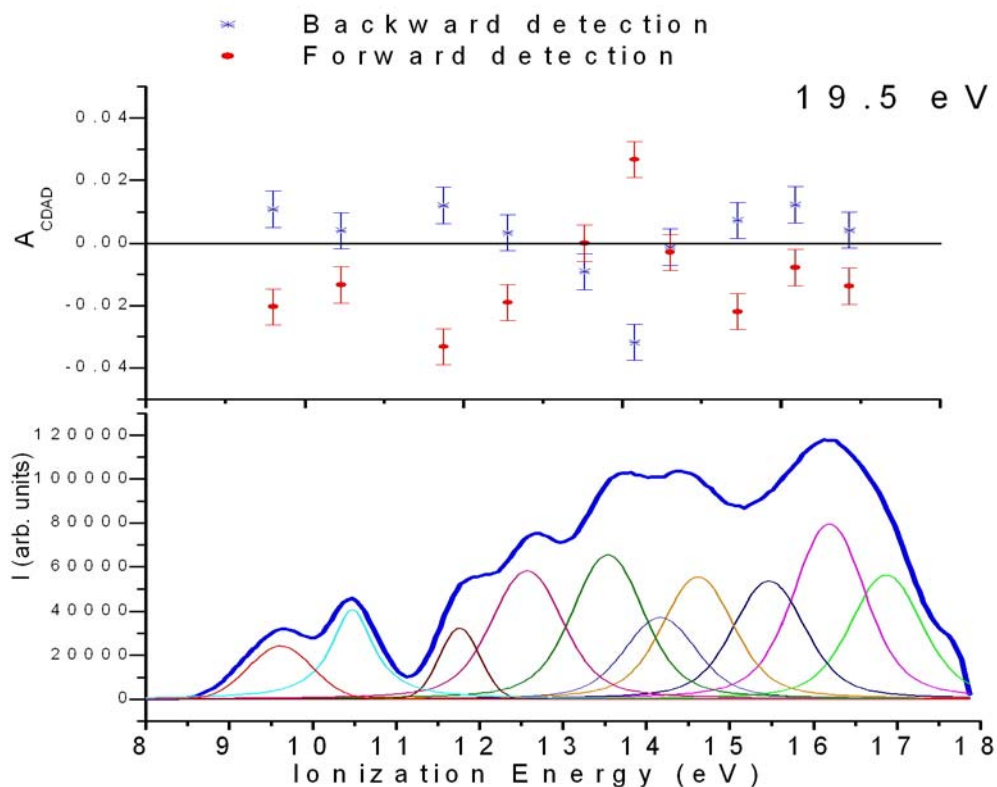


Figure 5.13: A_{CDAD} of D-Alaninol. In the bottom panel the valence spectrum at 19.5 eV at forward detection, is presented and in the top panel asymmetry parameter of L-Alaninol at the forward (red spots) and backward (blue spots) detection angle for 19.5 eV photon energy is reported.

directions. Opposite trends are observed for the same enantiomer at opposite directions, according to equation (3.6). D-Alaninol was measured to point out the change sign for D- and L-form, and $(I_+ - I_-)$ for D- and L-Alaninol are reported in figure 5.14.

The data in figures 5.13 and 5.14 demonstrate that for the chiral molecule, here examined, an energy-dependent asymmetry of up to $\pm 3\%$ exists and that the sign changes for two enantiomers.

The experimental D values appear strongly dependent on the specific orbital considered and the photon energy. In principle, by electron spectroscopy each initial state orbital can be analyzed separately to extract dynamical in-

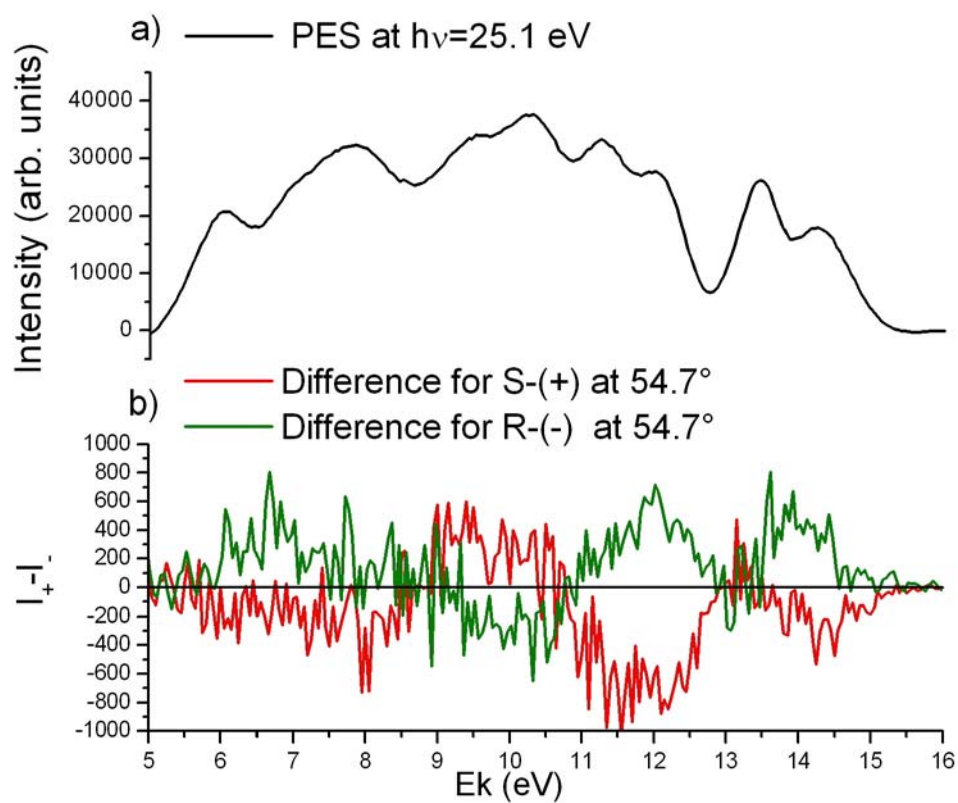


Figure 5.14: a) PES (black line) recorded at 25.1 eV as function of kinetic energy (E_k) is reported together with b) the difference ($I_+ - I_-$) for D-Alaninol (green line) and L-Alaninol (red line) for spectra taken at $\theta = 54.7^\circ$.

formation on the ionization process. Peaks at ionization energy 9.75 eV and 10.60 eV originates from single orbitals with an electron distribution localized on nitrogen and oxygen atoms. In contrast bands over 11 eV are overlapped together so many different orbitals contribute to the photoionization intensity. The corresponding dichroism, thus, has to be viewed as the net result of several orbitals with fairly delocalized electron density spread over large regions of the molecule. A deeper insight in qualitatively understanding of correlation between asymmetry, sign and strength of D factor is to analyze its dependence on kinetic energy from electrons photo-emitted from each state. The dichroism coefficient for valence photoionization channels has been reported as a function of the electron kinetic energy in figures 5.15 and 5.16. It is possible to identify different trends which can be partially explained according to the previous assignment (figures 5.2 - 5.4). Panels “21” and “20” corresponds to orbitals 2p on nitrogen and oxygen, respectively, and show a pronounced dichroic character, which decays with the kinetic energy. The other orbitals are less localized though they show strong dichroism. D tends asymptotically to zero at high kinetic energy and this can be explained considering that the fast escaping electrons become less and less sensitive to the asymmetry of global potential of the molecular ion as the kinetic energy increases. These measurements confirm D as a sensitive probe for structural and electronic properties determination of chiral molecules and point it as an able tool to map the whole molecular effective potential, i.e. the environment which contains the ionized orbital, especially considering the delocalized nature of the scattered photoelectron continuum orbital.

This experimental method has been used for S-(+)-methyl-oxirane [7] and S-(+)-3-Hydroxytetrahydrofuran [80] and found out to work properly in ac-

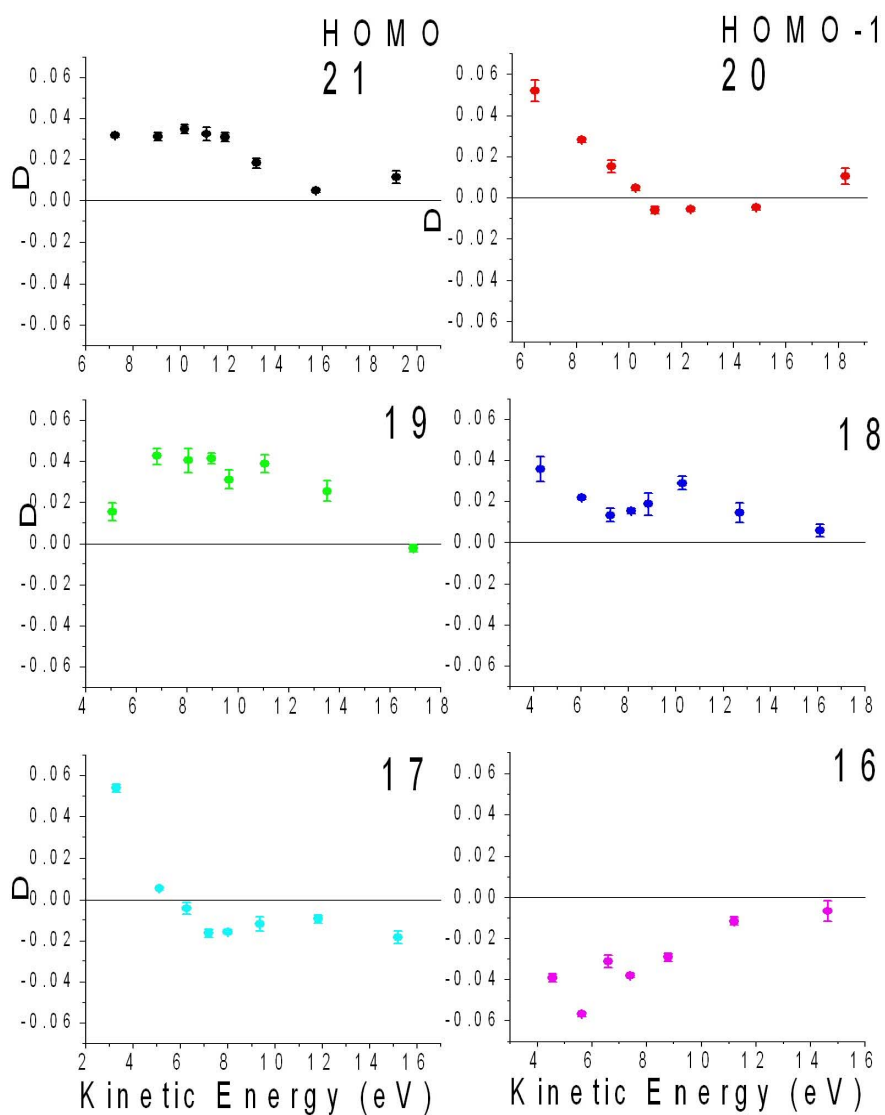


Figure 5.15: CDAD parameter D , derived by averaging the results obtained for both helicity for L-Alaninol as a function of $h\nu$ for fist six orbitals; 21 and 20 are labelled as HOMO and HOMO-1 they are located on nitrogen and oxygen lone pairs respectively.

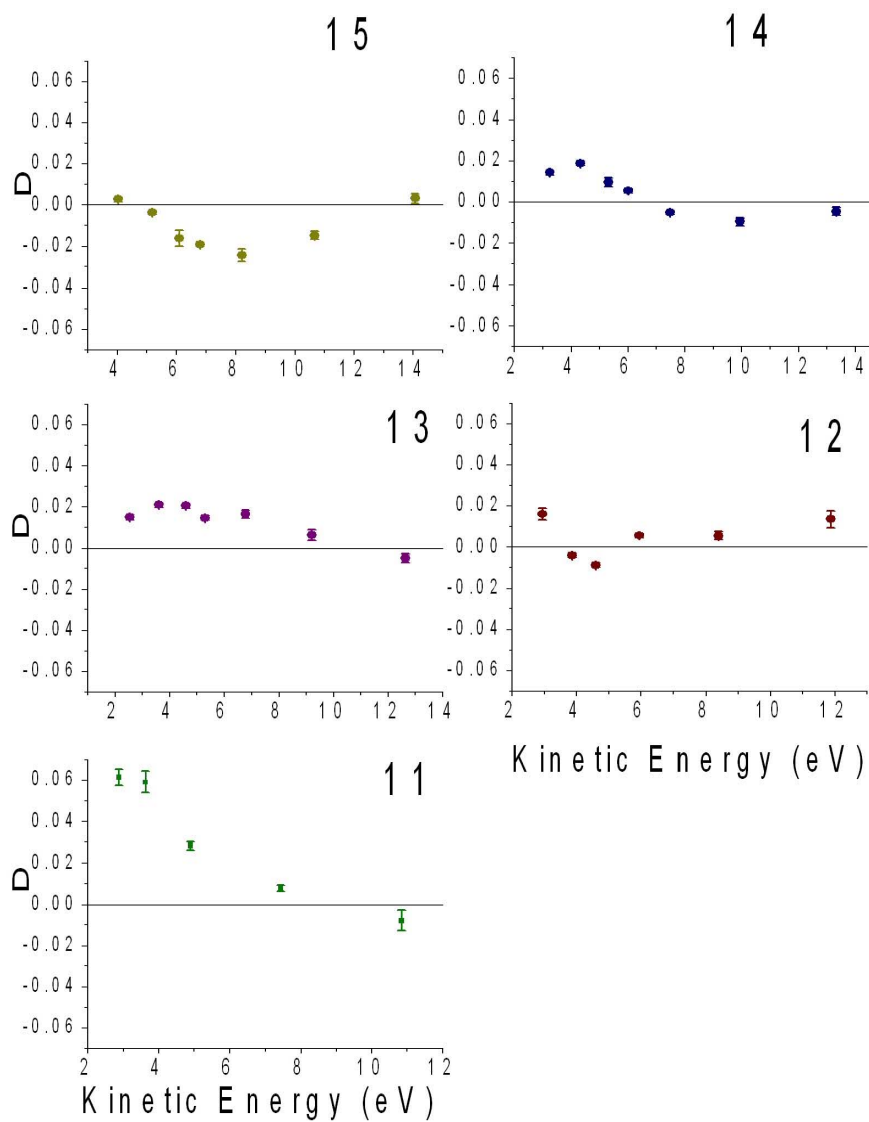


Figure 5.16: (...continue) CDAD parameter D , derived by averaging the results obtained for both helicity for L-Alaninol as a function of $h\nu$ for other five orbitals.

cordance with theoretical results.

In figure 5.17 D parameter profiles of the molecular orbitals of L-Alaninol (S-(+)-2Amino-Propanol), S-(+)-3-Hydroxytetrahydrofuran and S-(-)-methyl-oxirane corresponding to the oxygen lone pairs are plotted. Particularly, HOMO and HOMO-1 of S-(+)-3-Hydroxytetrahydrofuran are placed prevalently on the ring and hydroxilic oxygen respectively and in the case of S-(-)-methyl-oxirane HOMO is the orbital localized on the ring oxygen. Comparison among different molecules is meaningful, because it puts in evidence that the oxygen lone pair, in the examined cases, in a similar chemical environment, keeps its trend. HOMO-1 for S-(+)-3-Hydroxytetrahydrofuran and HOMO-1 of L-Alaninol (S-(+)-2Amino-Propanol) both correspond to the hydroxilic group and both are positive at lower kinetic energies and tend asymptotically to zero at higher energies. The same trend can be observed also for HOMO of S-(-)-methyl-oxirane and S-(+)-3-Hydroxytetrahydrofuran but they show an opposite sign. Moreover, a strong dichroic effect can be detect on HOMO-1 of L-Alaninol and HOMO of S-(+)-3-Hydroxytetrahydrofuran orbitals which are not bonded to the chiral center indicating that the photoemitted electron is sensitive to the whole molecular potential, and to the global asymmetry, felt while escaping. This becomes less important as much as kinetic energy increases.

A computational code, based on LCAO β -SPLINE DFT has been implemented so far by Decleva et al.[105]. In his papers Decleva has predicted cross section (σ), asymmetry parameter (β) and dichroic parameter D values for a fixed geometrical form of different conformers of a molecular compound and, also, changing substituents of a specific molecule. He observed that D parameter changes significantly while cross section (σ) and asymmetry parameter (β)

remain almost unperturbed, thus, dichroic parameter D appears to be highly sensitive to the whole structure. This code gives very satisfactory results for S-(+)-methyl-oxirane in comparison with experimental data, [7] since methyl-oxirane exists at the experimental conditions in one conformer, and partially for 3-Hydroxytetrahydrofuran which instead, presents, more conformers [106]. A correspondence between experimental and computed values would be gained considering all the conformers existing at the working conditions.

Anyway, a larger set of experimental system studies would be necessary to identify more precisely the importance of conformational, structural and electronic effects on dichroic properties.

5.3 Conclusions

The study of the dichroic effects of chiral molecules is an important tool to investigate the electronic structure of chiral systems. The circular dichroism in photoelectron spectroscopy of randomly oriented chiral molecules gives the opportunity to find, via the odd-even mixing of the wave function, a fingerprint of the strong connection between asymmetry and electronic properties. This technique is very sensitive to the electronic structure of the system as demonstrated by a wealth of structures exhibited by the behavior of D parameters as a function of photoelectron kinetic energy obtained for each band of the spectrum. Also, D trends deserve attention, since they behave a rich dynamic, they are measured to decay rapidly with the photoelectron energy, it can be supposed that the faster escaping electrons become less sensitive to the asymmetric global potential of the molecular system. Finally it permits a direct correspondence between lines in the spectra and D parameter so it is possible to understand structural and electronic influences on the chiral

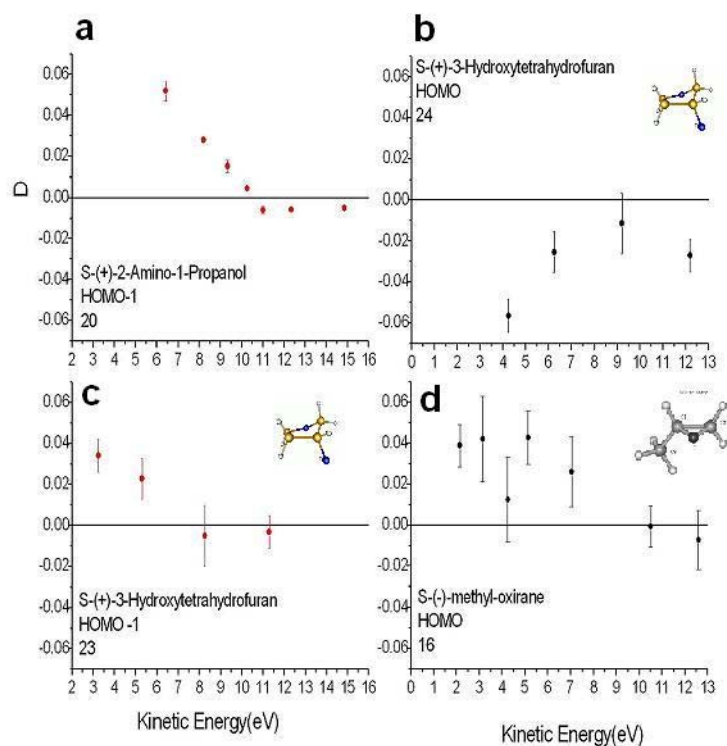


Figure 5.17: D parameter as a function of $h\nu$ for **a.** S-(+)-2-Amino-1-Propanol where HOMO-1 (20) located on the hydroxilic oxygen; **b.** and **c.** S-(+)-3-Hydroxytetrahydrofuran where HOMO (24) and HOMO-1 (23) orbitals are located on lone pair belonging to the epoxidic oxygen, far from the chiral center; and hydroxilic oxygen. In the inset the structure is shown where oxygen is represented in blue, carbon in yellow and hydrogen in white; **d.** S-(-)-methyl-oxirane where HOMO (16) and the molecular structure is shown with oxygen in black, carbon in grey and hydrogen in light grey.

recognition process. Moreover, the CDAD technique represents an interesting enantioselective spectroscopy which might be used to resolved the absolute configuration of asymmetry carbon atoms in organic compounds.

The general characteristics of the observed photoelectron circular dichroism, particularly the asymmetry of the chiral distribution parameter with respect to exchange of the handedness of either molecule or light or detector and the relatively large magnitude of the dichroism (3% - 5%), confirm the theoretical predictions and expectations of an effect based purely in the electric dipole approximation.

The present study sheds light on a new capability of photoelectron dichroism which appears to be sensitive not only to electronic factors, but also to structural, and conformational factors.

Chapter 6

D-Alaninol Adsorption on Cu(100) and Cu(110)

Organic and biological molecules are important tools to introduce complex reactive functionalities and superstructures at a metal surface with new property of symmetry. An organic layer provides new activities such as passivation or selectivity functions. Organic functionalisation of a metal surface has important applications in catalysis, sensors, corrosion inhibition, molecular recognition, optoelectronics and lithography.

A review had been published in 2003 by Barlow and Raval [2] which reports on adsorption of complex organic molecules at metal surface. From this review it can be underlined the complexity of organic/metal interface and the need of complementary and combined surface spectroscopies to disentangle it.

Experimental results concerning the attempt of decorating copper surfaces with chiral organic molecules (D-Alaninol) are presented in the following chapter.

6.1 Single Crystal Copper Surfaces

An ideal surface is the sudden truncation of the translational 3D symmetry of a solid and maintains the structure of a lattice plane. Real surfaces consists of a mixture of flat regions (called terraces) and defects (steps, kinks and point defects). Since the local distribution of atoms around each of these individual surface sites is different, the electronic properties will be different as well. Hence, each surface site will exhibit its own singular surface chemistry and physical response. Therefore, in order to obtain reproducible results on a particular type of solid surface, it is necessary to precisely define the chemical and structural state of the substrate under investigation. The most simplified system is a surface containing an high ratio of terrace to defect sites (flat surface) and consisting of just one type of atom, such surfaces are referred to as being well-defined. This approach resolves all the myriad structure/composition combinations down to just a single type of site. Greater complexity can be introduced into the system by adding controlled amounts of coverages of adsorbates. To ensure that experiments are performed on well-defined surfaces, single crystals are invariably used as substrates. This is because a given cut through such a crystal will expose a particular crystal plane that can be labelled with Miller index like Cu(100) and Cu(110) and, thus, they represent a good model structure.

Figure 6.1 shows the principal low index planes (with Miller index contain only 0 and 1) of fcc crystal; the important crystallographic directions within each plane, the interatomic separations in terms of the bulk lattice constant a and the primitive surface unit mesh associated with each plane are shown as well.

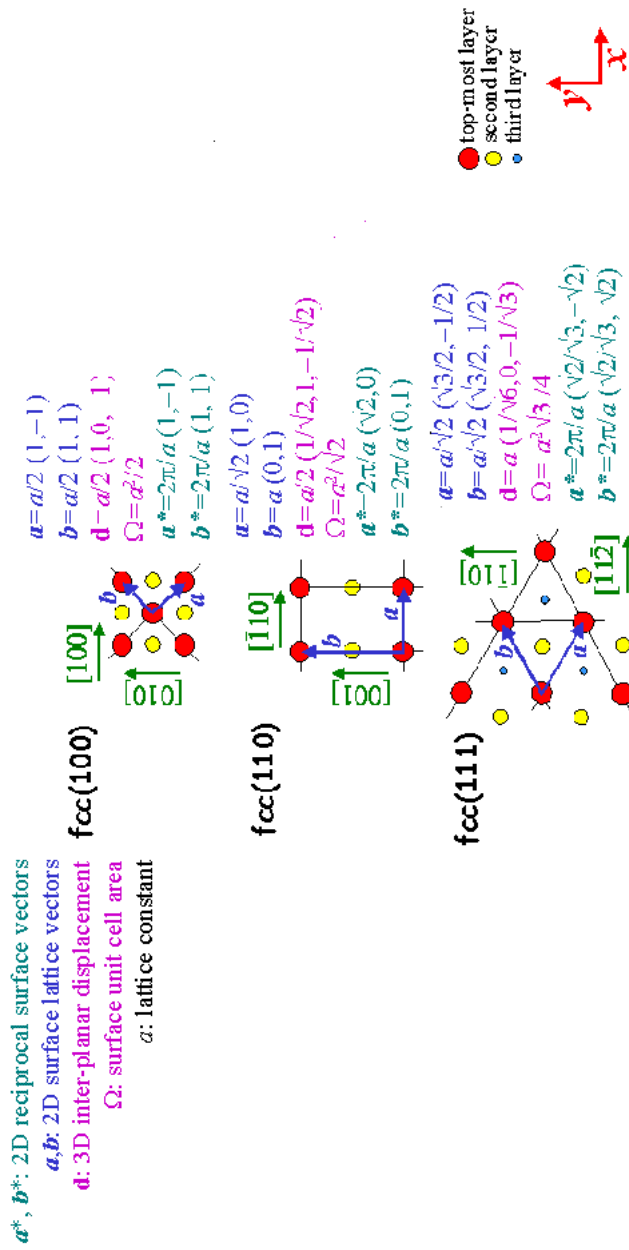


Figure 6.1: The (100), (110) and (111) plane of fcc crystals.

The five possible surface unit cells of Bravais lattices in two dimensional systems (four primitive and one centered) are described in figure 6.2.

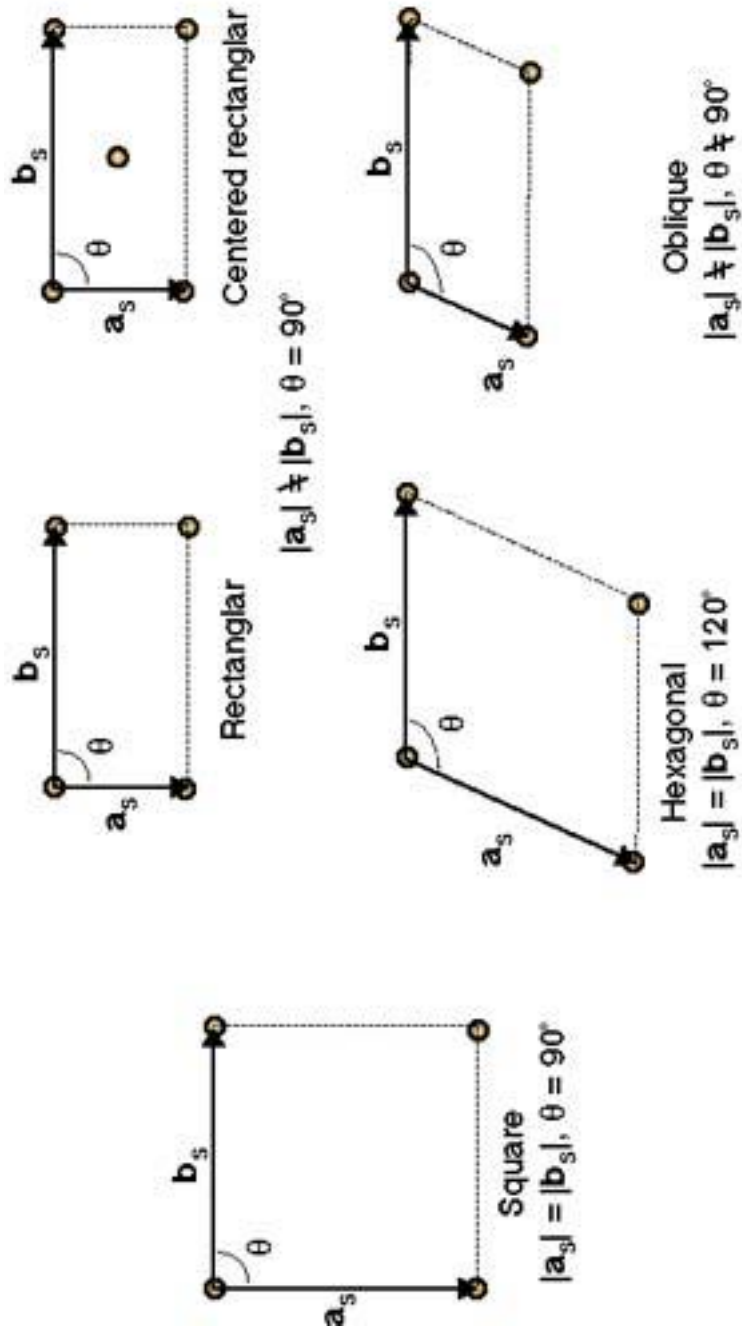


Figure 6.2: The five Bravais surface lattices.

Simple truncation of a bulk single crystal should produce a well-defined

atomic periodicity in the exposed plane. This cut causes a loss of coordination of atoms at the vacuum-solid interface in order to achieve a lower surface energy it may undergo a 'surface relaxation' in the form of an oscillatory change in the interplanar spacing and also gross restructuring of the surface plane. Metal surfaces do not suffer from this phenomenon so the cut leads to a surface with crystallographic characteristics equal to the bulk.[88, 51, 107]

6.1.1 Clean Cu (100) and (110)

Copper is a noble metal, whose crystalline structure is described by a face centered cubic lattice (fcc). The lattice parameter is $a_0 = 3.61\text{\AA}$.

The two dimensional lattices projected on a surface are shown in figures 6.3 and 6.4.

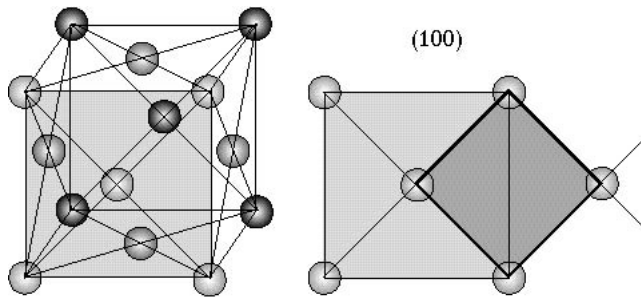


Figure 6.3: (100) plane of fcc copper crystal. 3D and 2D structure are reported.

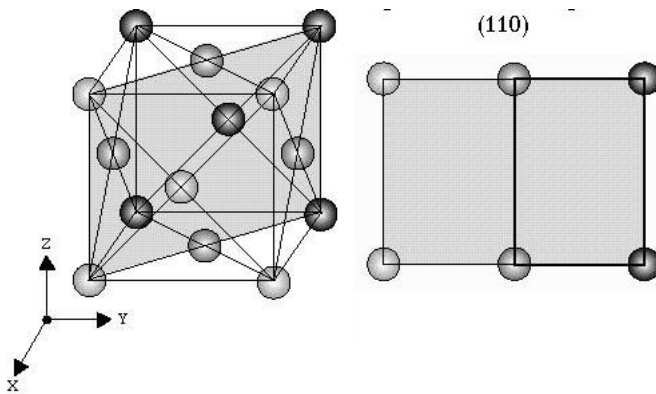


Figure 6.4: Cu(110) plane of fcc copper crystal. 3D and 2D structure are reported.

In figures 6.5 and 6.6 LEED pattern for clean Cu(100) and Cu(110) at 50 eV and 80 eV are presented, together with real lattice scheme.

Cu(100) primitive cell has side $a = a_0\sqrt{2} = 2.55\text{\AA}$. The surface reciprocal lattice has a square primitive cell, clearly distinguishable in the LEED pattern from the clean surface, the side is $l = \frac{2\pi}{a_0\sqrt{2}} = 2.46\text{\AA}^{-1}$ (Figure 6.5).

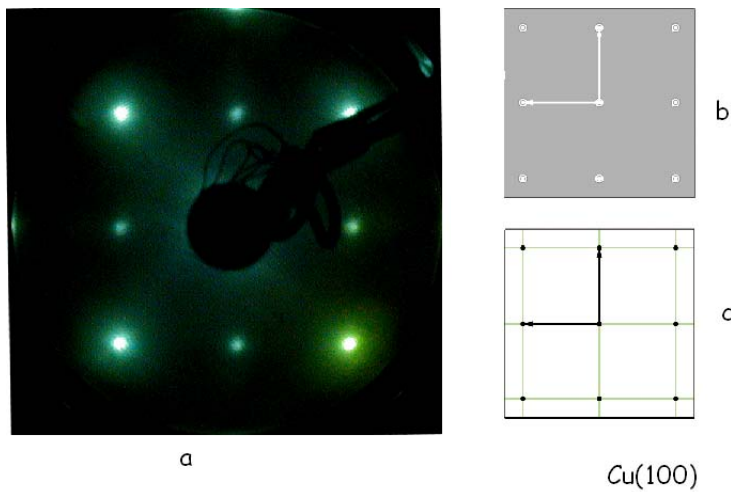


Figure 6.5: Cu(100) a. LEED pattern, recorded at 50 eV; b. reciprocal lattice outline; c. real lattice outline.

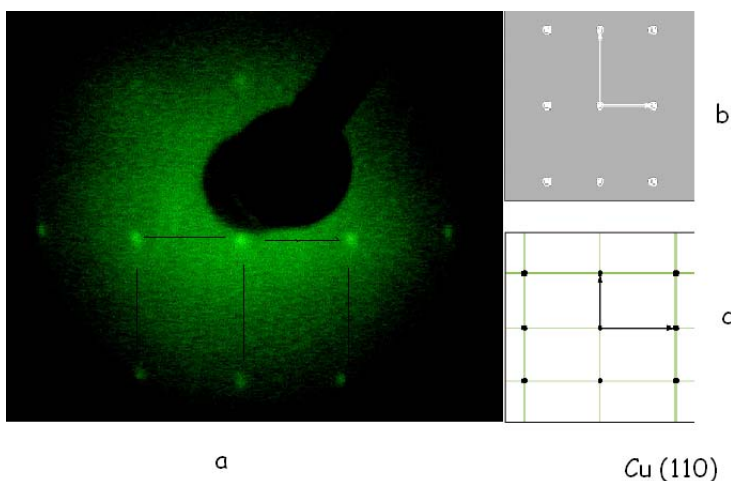


Figure 6.6: Cu(110), a. LEED pattern, recorded at 80 eV; b. reciprocal lattice outline c. real lattice outline.

Cu(110) crystallographic parameter is $a = a_0 = 3.61 \text{ \AA}$, the reciprocal lattice has primitive cell has $l = \frac{2\pi}{a_0} = 1.74 \text{ \AA}^{-1}$, as shown in figure 6.6.

The actual 2D surface lattice coincides with that of the truncated surface since no reconstruction phenomena occurs after the cut.

6.2 D-Alaninol on Cu(100) Surface: Results

6.2.1 Adsorption: growth morphology

Growth of D-alaninol on Cu(100) surface has been investigated by means of XPS and LEED. A set of photoelectron spectra are shown in figure 6.7 recorded at increasing exposure of D-alaninol on Cu(100) at room temperature. Exposure is expressed in Langmuir (L) which expresses the coverage in term of exposition resulting after 1s at 10^{-6} torr, assuming the sticking factor equal to 1. Photoelectrons is excited by an X-ray source at 1487.6 eV (Al K α) at normal incidence and analyzed with an hemispherical electron analyzer with a pass energy of 70 eV corresponding to an estimated resolution of 300 meV.

Detector is placed at 65° from the surface normal. Binding energy scale is calibrated by means of Cu 2p core line and Fermi level.

C 1s, O 1s and N 1s regions have been monitored starting from a clean Cu surface. Figure 6.7 shows that above 15L no substantial changes are observed in spectral intensities, suggesting that a saturation coverage is reached. C 1s and O 1s do not change significantly along the growth while in N 1s region after 15L a second line appears at about 2 eV higher binding energy.

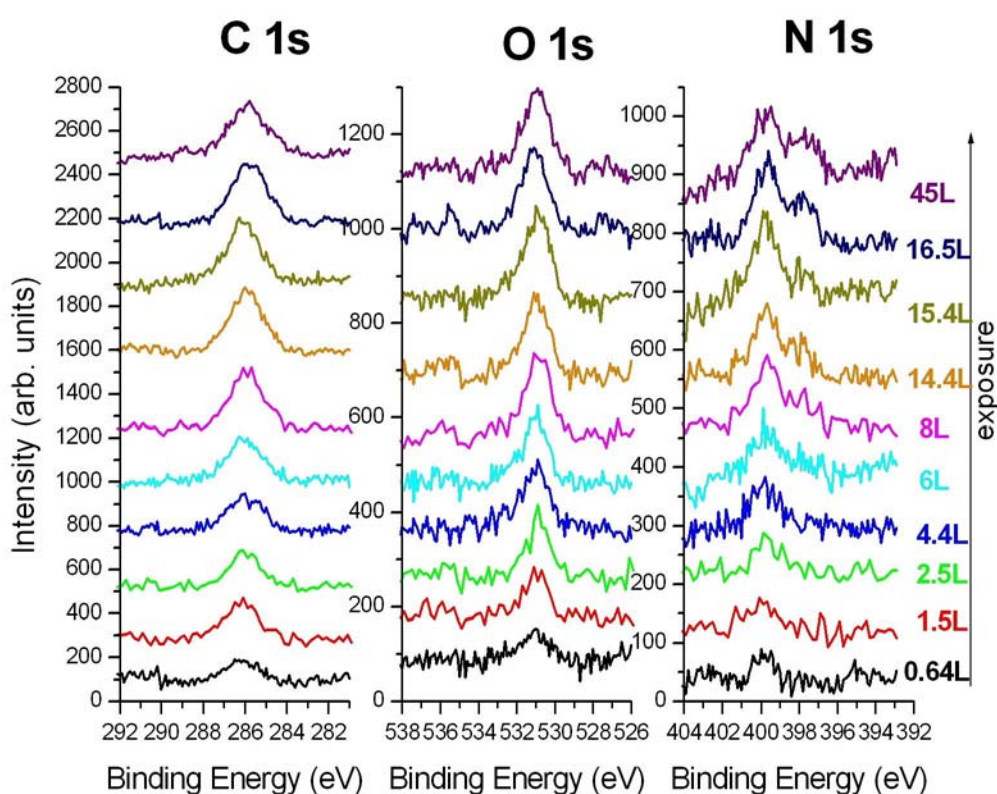


Figure 6.7: C1s, O1s and N1s lines of Alaninol on Cu(100) as a function of the exposure. Background have been subtracted and spectra are vertically displaced.

This system achieves saturation coverage forming a monolayer after which no significant modifications appear. This trend was checked following the ratio between the peak area of C 1s and Cu 2p photoemission lines (I_{C1s}/I_{Cu2p}) as

a function of the exposure, which at constant pressure, is proportional to the exposure time. This behaviour, shown in figure 6.8, is described by Langmuir law (chapter 2) whose parameter are reported in figure as well.

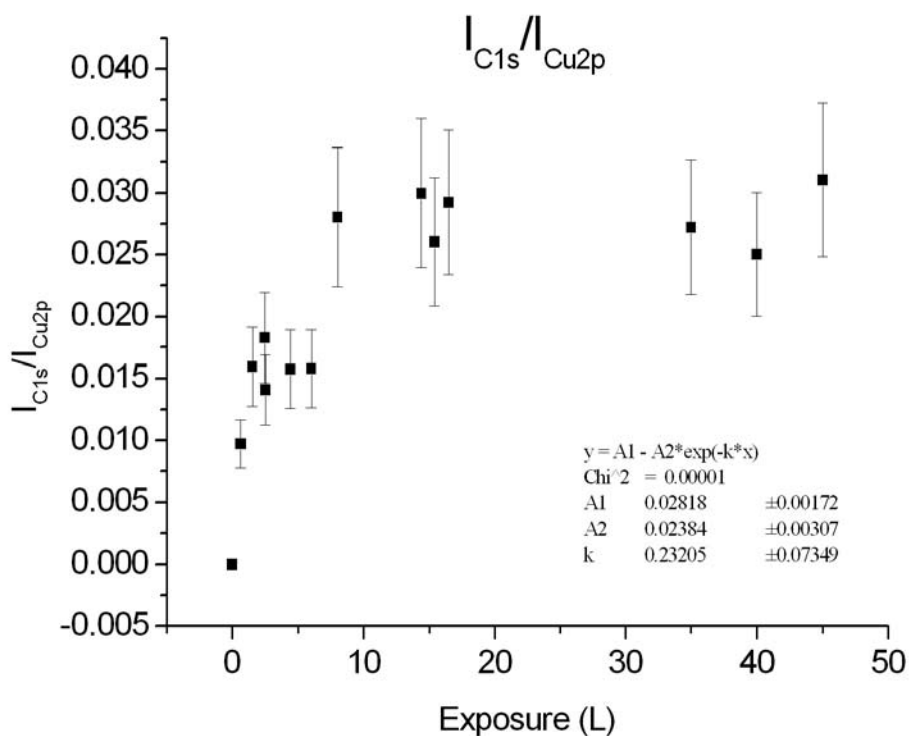


Figure 6.8: For the growth of D-alaninol on Cu(100), ratio I_{C1s}/I_{Cu2p} was followed along the increasing exposure. Uncertainty is estimated as 20% both for the ratio and for the exposure; uncertainty on the ordinate is displayed with bars while for abscissa is not reported for clarity. Langmuir fit parameters are reported in the inset.

In conclusion D-alaninol saturates forming a monolayer, two different phase are detected at low coverage (below 15L) and at high coverage (above 15L), whose difference is mainly due to a change in the interaction between $-NH_2$ and the copper surface.

More insight has been gained with LEED and by using synchrotron radiation which allows a more precise and resolved analysis of core lines and valence

states.

6.2.2 Low energy electron diffraction (LEED)

From XPS spectra we got that a saturated monolayer is formed on Cu(100), LEED was monitored along the growth of D-alaninol on Cu(100) to find out a long range order on the surface due to the chemisorbed species.

LEED pattern was detected when saturated coverage was reached above 15L and the result is presented in figure 6.9. This is indicative that D-Alaninol forms a long range ordered structure when it chemisorbes on the Cu(100), self-assembling on the surface. LEED pattern exhibits an overlayer that can be represented in matricial form as follows:

$$\begin{pmatrix} 4 & -1 \\ 1 & 4 \end{pmatrix}$$

Reciprocal and real lattice outline is reproduced in figure 6.10. This scheme shows that the overlayer has a square structure rotated from Cu real lattice, the corresponding reciprocal space is shown too and diffracting unit are found to be aligned on a direction 14° degrees apart from Cu [011] direction.

Supramolecular assembly of the adsorbate D-alaninol units produces a unique direction, creating an oblique chiral unit mesh belonging to the C₂¹ space group such as glycine, alanine, cysteine and tartaric acid [2].

Although the electron beam current was kept at a minimum setting, the pattern degraded in about 10 minutes. To avoid sample damage due to electronic excitations progressive shifting of the sample to adjacent positions resorts the missing pattern.

¹Schoenfleis notation.

The arrangement of the D-Alaninol on Cu(100) was explored also with scanning tunneling microscopy and results are reported in section 6.2.4.

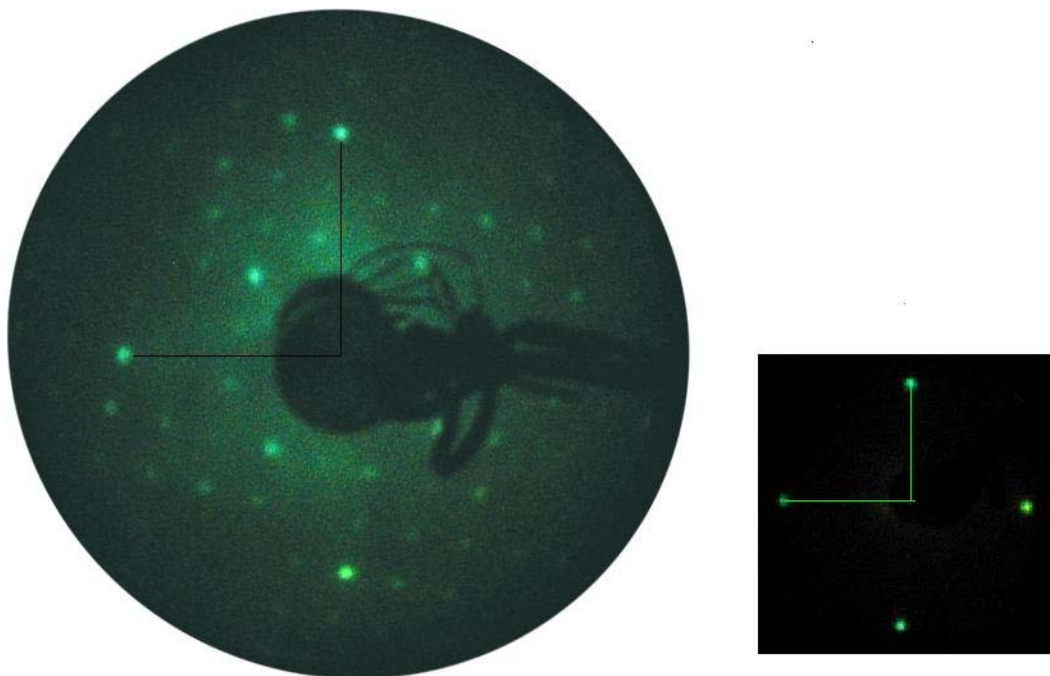


Figure 6.9: LEED pattern observed at 37 eV for the ordered (4 -1, 1 4) D-Alaninol on Cu(100). The inset presents LEED pattern of clean Cu(100).

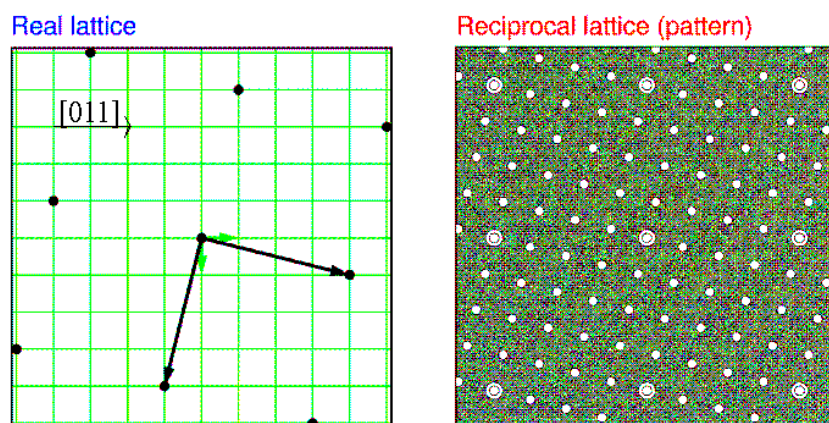


Figure 6.10: Reciprocal and real space outline of D-Alaninol on Cu(100); in the real lattice green net represents substrate atoms while the black spots are the unit of the adsorbate. The reciprocal lattice, that is, the LEED pattern, small white spot are from the adsorbate and big ones are from the Cu atoms.

6.2.3 Photoelectron spectroscopy results

Synchrotron radiation photoelectron spectroscopy is a powerful tool due to the possibility of tuning the photon energy, it allows to reach high flux with high resolution and, consequently, follow small changes in binding energy changing coverage.

Core lines and valence states were investigated and results are presented here. Angle-integrated hemispherical analyzer was used and placed at normal incidence.

Binding energy scale was calibrated using as reference the Cu 3p line and the Fermi level. Intensities were normalized to photo-current from a gold mesh placed at the entrance of the end station.

Core spectra C1s, O1s and N1s lines were measured for low (below 15L) and high (above 15L) coverage. In figure 6.11 C1s line is presented, at $h\nu=320$ eV, this line is well represented by the deconvolution in three Voigt functions; the line at binding energy 285.70 eV is typical of carbon involved in C-C bond, such as the methyl group as for ethanol and acetic acid, the other two components are superimposed at 286.06 eV and 286.09 eV due to C-NH₂ and C-OH, these assignments are in analogy with glycine, alanine, cysteine and ethanol studied on copper surfaces [102, 103, 108, 109]. C1s spectrum does not change significantly increasing the coverage, small shifts of the same order of the experimental uncertainty can be detected (-CH₃ from 285.70 eV to 285.67 eV; C-NH₂ from 286.06 to 286.04; C-OH from 286.09 to 286.11 eV). A small component on the spectra can be seen at lower binding energy (284.8 eV) due to a molecular photo-induced damage, this component increases with exposure to the radiation. In figure 5.10 and table 5.2, the C1s spectrum recorded in gas

phase is reported. A band at 290.8 eV, typical of methyl group, considering the work function for copper (4.7 eV), it shows a small shift to lower binding energy of $\Delta E = 0.4$ eV. The other two bands ascribed to -C(-NH₂) and -C(-OH) shift of $\Delta E = 0.6$ eV and $\Delta E = 1.3$ eV, respectively. This two core lines superimpose interacting with the surface indicating a more intense interaction of the oxygen with the surface since its carbon related peak suffers from a larger modification.

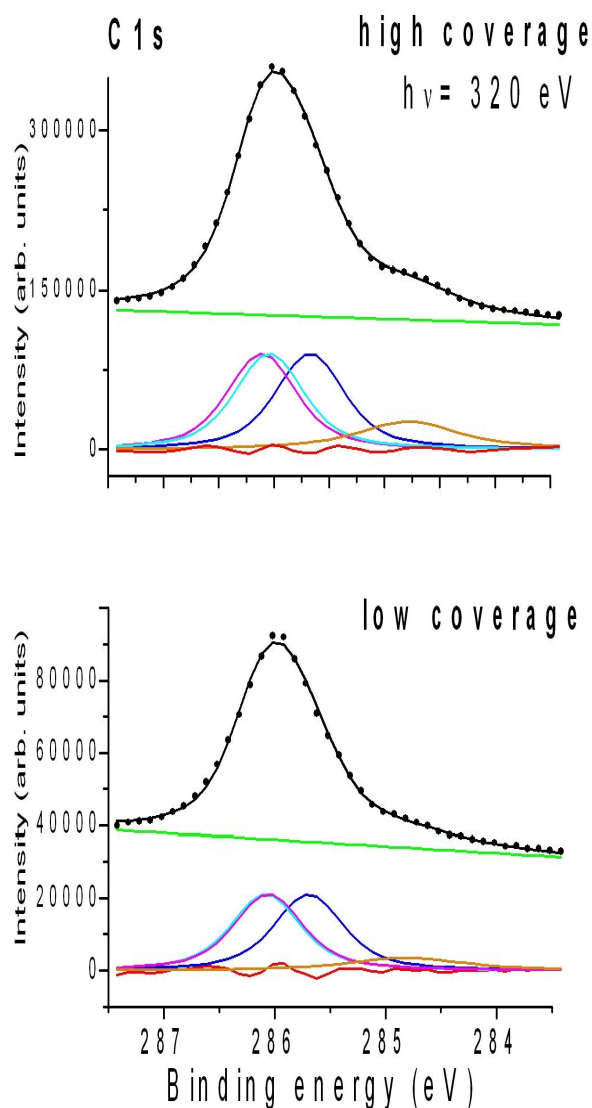


Figure 6.11: C1s for low and high coverage, recorded at $h\nu= 320$ eV incident photon energy with an overall resolution of 50 meV. Background (green line), residuals (red line) and Voigt functions are presented; another component at 284.5 eV can be seen which is associated to a contamination or photo-induced damage.

One component can be detected in O1s spectrum located at 530.81 eV, like for ethanol [108] and acetic acid on single crystal metal surface typical of a bond to the metal. O1s line is found at 530.81 eV for low coverage, it moves at 530.48 eV at high coverage (figure 6.12), this small shift indicates a change

in the chemisorption interaction which, anyway, does not involve -OH group directly; these spectra are recorded at photon energy, $h\nu = 620$ eV.

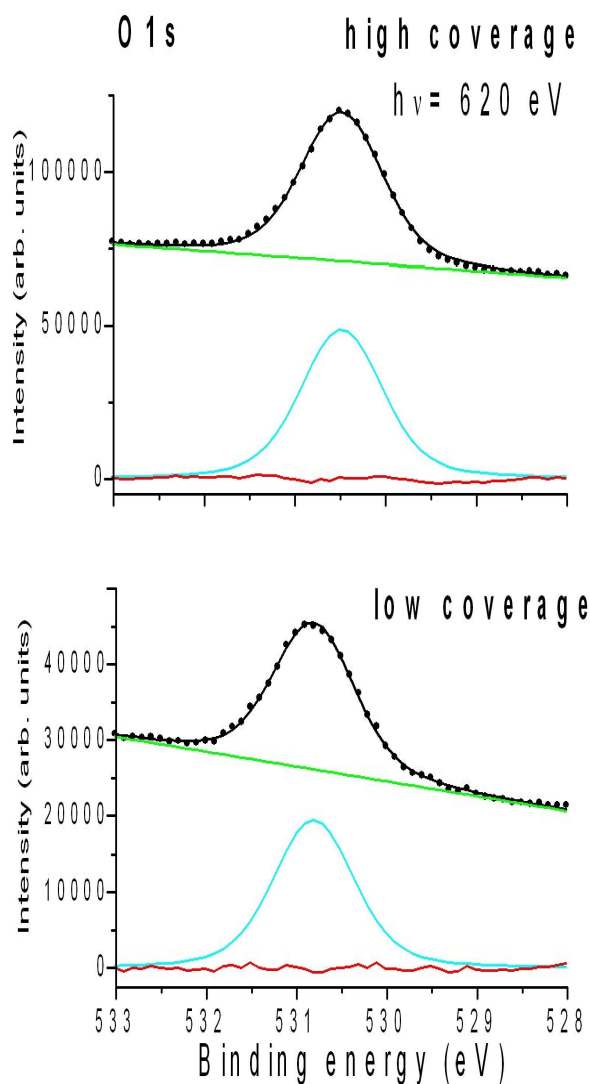


Figure 6.12: O1s for low and high coverage, recorded at $h\nu = 320$ eV incident photon energy with an overall resolution of 50 meV. Background (green line), residuals (red line) and Voigt function are presented.

N1s is recorded at 508 eV photon energy, figure 6.13 reveals that two different nitrogen species are formed upon Alaninol adsorption. At low coverage only one component, at 399.58 eV, results from the spectra; this line is as-

sociated with -NH_2 in analogy with cysteine and glycine [110]. It shifts at 399.43 eV for high coverage while at 397.52 eV a second band appears when a monolayer is formed and can be associated to the -NH_2 coordinated to copper atoms. This shift of 1.91 eV is close to what is found for glycine whose amino group bonds copper surface or copper ion complexes [111]. Thus, this second peak is due to bonding of the molecule through the nitrogen.

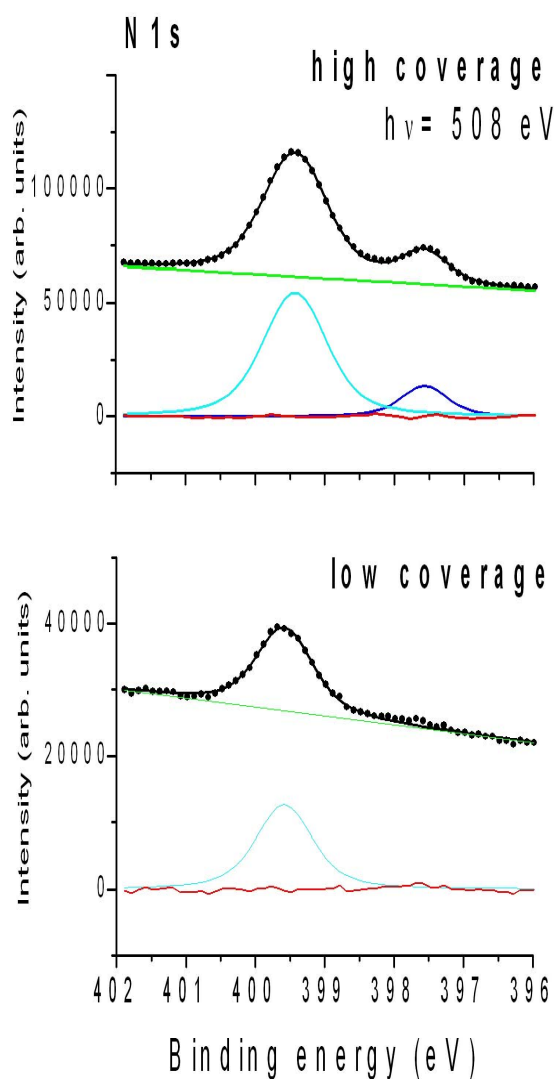


Figure 6.13: N1s for low and high coverage, recorded at $h\nu= 320$ eV incident photon energy with an overall resolution of 50 meV. Background (green line), residuals (red line) and Voigt functions are presented.

The core level analysis reveal an overall change in binding energies of O1s and N1s increasing the coverage, thus, D-Alaninol on Cu(100) seems to have at least two active functional groups -OH and -NH₂.

Valence band Valence band of D-alaninol on Cu(100) surface is presented in figure 6.14. It is recorded at 50 eV with an overall resolution of 50 meV and is reported at low coverage (below 15L) and at high coverage (saturated level). The insets display in details the observed relevant features . Close to *d* orbital of copper a shoulder appear at low coverage at binding energy 2.05 eV (a), which rises increasing the coverage. Another structure appears at 13.53 eV (c), for a low coverage deposition, which remains unperturbed at high coverage. The valence photoelectron spectrum of saturated coverage reveals a wealth of new structures at 15.78 eV and 18.24 eV and a broad band between 7 eV and 11 eV, while line (a) moves toward lower binding energy and become broader.

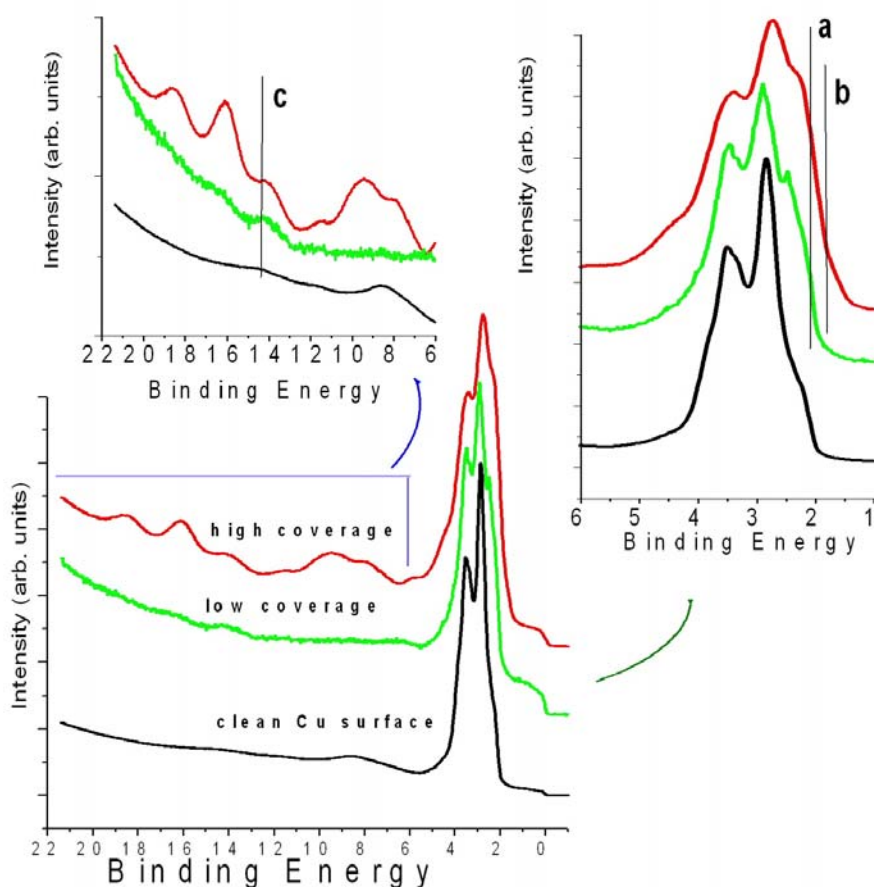


Figure 6.14: Valence band spectra of D-alaninol on Cu(100) recorded at 50 eV photon energy with an overall resolution of 20 meV; black line is valence band of clean Cu(100); the green line and the red line are the valence band for low coverage and high coverage, respectively. Insets displays more particularly range at lower binding energy and at higher to give a better view of the new structure induced from chemisorption.

An attempt to assign this new structures superimposed to the Cu electronic states can be done by comparison with gas phase spectrum of the adsorbate, considering only “initial state effects” and, so, in Koopman’s approximation. In this view the new line appearing at 2.05 eV (a) can be assigned to the orbital 20 (HOMO-1 shown in figure 5.2) which is located on the oxygen atom.

At the beginning of the growth molecule arrangement on the surface is disordered, the original discrete levels of the adsorbate will shift to lower energy

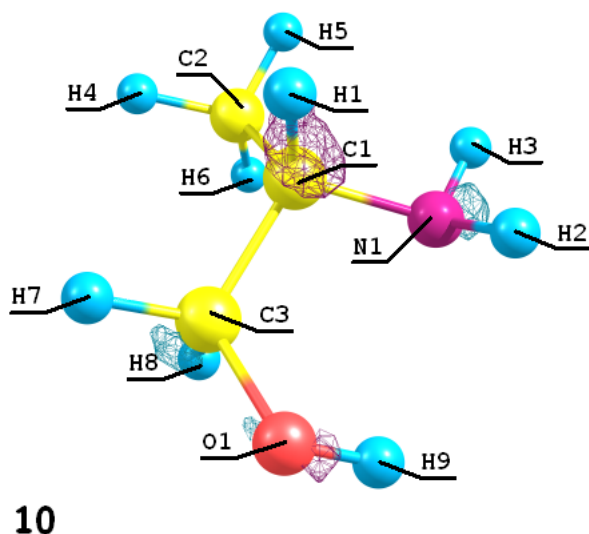


Figure 6.15: Orbital 10, already reported in figure 5.4, is repeated here.

(orbital 20) owing to the chemical interaction with the metal and the whole spectrum will appear broadened, therefore adsorbate-induced states are hard to be detected in the low coverage stage being less intense. Only line (c) - at 13.53 eV - is clearly resolved, this state is associated with orbital (10) in figure 6.15 and appears to be delocalized on the whole structure.

A 'difference spectra' enables to better understand what happens increasing coverage, figure 6.16 illustrates UPS difference spectra from D-Alaninol adsorbed on Cu(100) between low and high coverage and the corresponding gas phase spectrum of D-alaninol at 50 eV. Valence band D-Alaninol on Cu(100) of is aligned against the Fermi level, gas phase valence band is aligned against vacuum level, so this was shift to take into account the gap between Fermi level and vacuum level for surfaces [112]. From this figure a shoulder at 1.67 eV (b) appears, in figure 6.14 and 6.16, this line is due to the HOMO of D-alaninol which is the lone pair located on the nitrogen atom. Differential shifts of a line can be taken as evidence that this is primarily responsible for the

chemisorption bond to the surface.

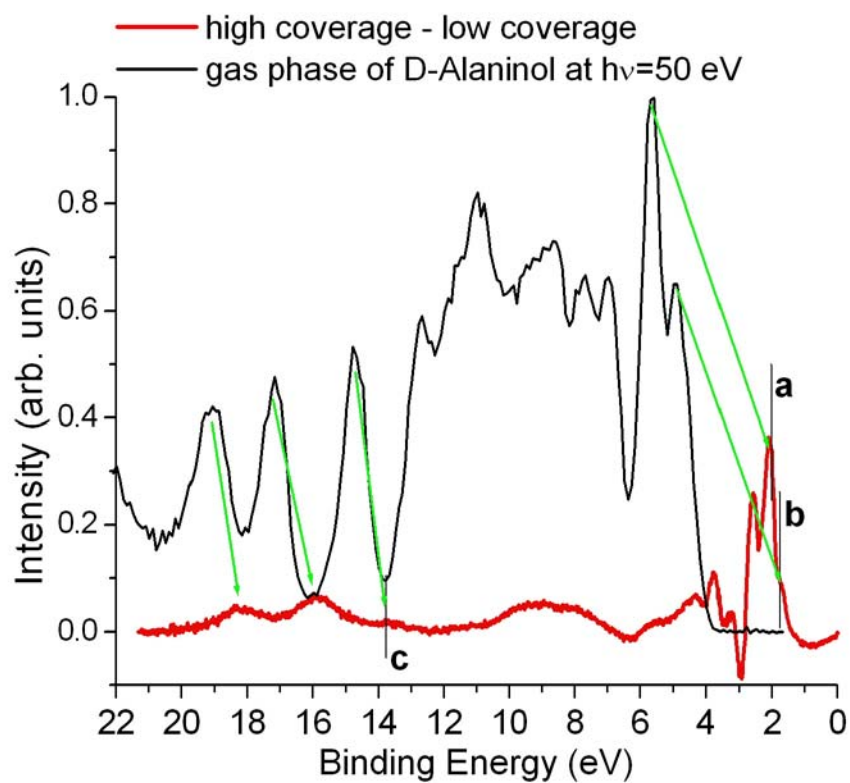


Figure 6.16: Valence band difference between high coverage and low coverage spectra of D-alaninol on Cu(100); black line is the gas phase valence band of D-alaninol.

The spectrum of D-alaninol chemisorbed agrees well with the gas phase spectrum indicating that the adsorbate maintains its molecular integrity when adsorbed, as can be seen in figure 6.17. Thus, conclusion is that D-alaninol adsorbs as a whole, that is, without dissociation and it is bonded through the oxygen at low coverage while at high coverage both oxygen and nitrogen lone pairs bond to the Cu surface.

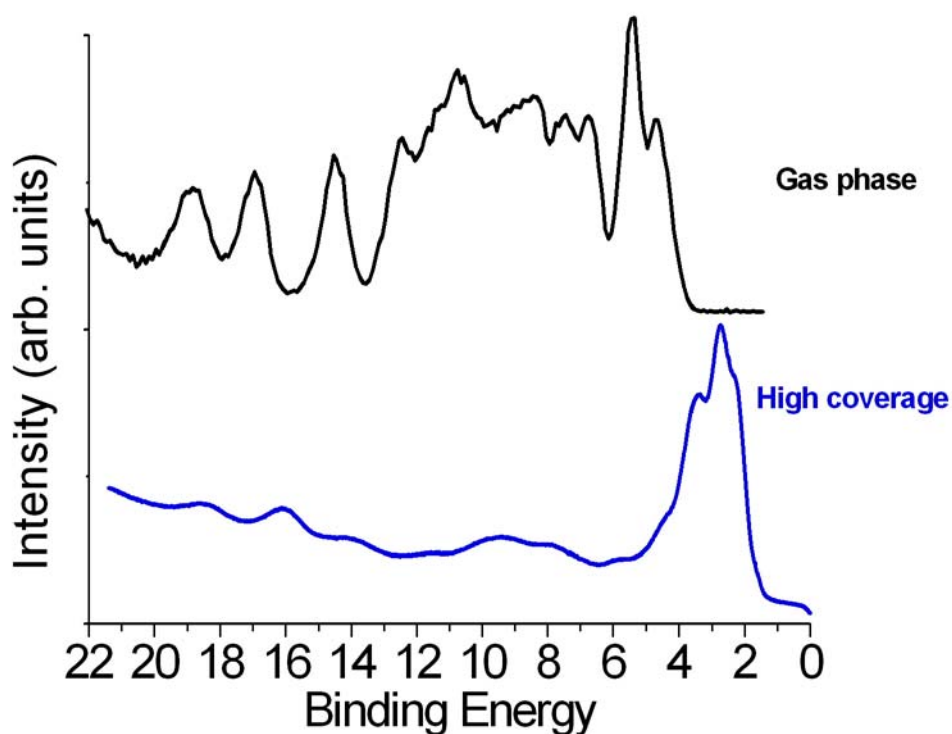


Figure 6.17: Valence band of D-alaninol in gas and chemisorbed ordered phase on Cu(100).

A photo-induced damage was observed during the whole experiment after one hour of irradiation, spectra are restored shifting the sample. This makes difficult to perform an angle resolved photoelectron experiment due to time needed according to the available apparatus.

The photon sensitivity of the studied system brought us to use the scanning tunneling microscopy to investigate the ordered monolayer structure formed on Cu(100) in order to avoid photolysis.

6.2.4 Scanning tunneling microscopy images

LEED and PES results show that D-alaninol self assembles into an ordered (4 -1, 1 4) saturated phase coordinating with oxygen and nitrogen lone pairs

and creating a 2D chiral template. STM image of this phase is presented in 6.18, the diffracting unit is revealed to be formed by two molecules and the presence of the long-range order is confirmed, yielding an oblique $(4 -1, 1 4)$ repeat surface unit mesh, with dimension $10 \times 8 \text{ \AA}$, each unit cell appear chiral and contains two protrusions indicating two molecules, such as alanine [113] and glycine [114], with a fractional coverage of about $1/8$ with respect to the number density of surface metal atoms.

Since amino and hydroxyl groups are present simultaneously in the same molecule and both are able to act as a H-bond donor and acceptor, molecules can package and form chains connected by hydrogen bonds N-H...O and O-H...N, aligning along a direction at 14° from $[011]$ direction (as in LEED pattern) allowing a chiral self-assembly. The molecular growth direction destroys all the symmetry elements of the underlying metal, leading to a creation of a chiral surface that is non-superimposable on its mirror image.

The images, shown here, were obtained in the constant current mode, brighter regions in the images correspond to a retraction of the STM tip and darker regions to a movement of the tip toward the surface. Thus, 'bright' regions correspond to topographical protrusions while 'dark' regions correspond to topographical depressions. Since STM is a local surface probing technique, the surface was oversampled widely, that is, many positions were randomly observed both on clean and on the deposited surfaces, respectively, a series of images are shown in figure 6.19.

In figure 6.20 profiles are presented. In profile 1 pairs of peaks show a mean difference in intensity of about 20% indicating a line of molecules aligned; while in profile 2 peaks difference is less than 5%, thus, it confirm that pairs of peaks correspond to pairs of molecules aligned with same termination on which profile

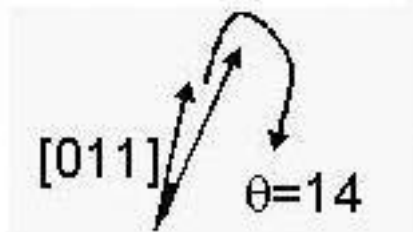
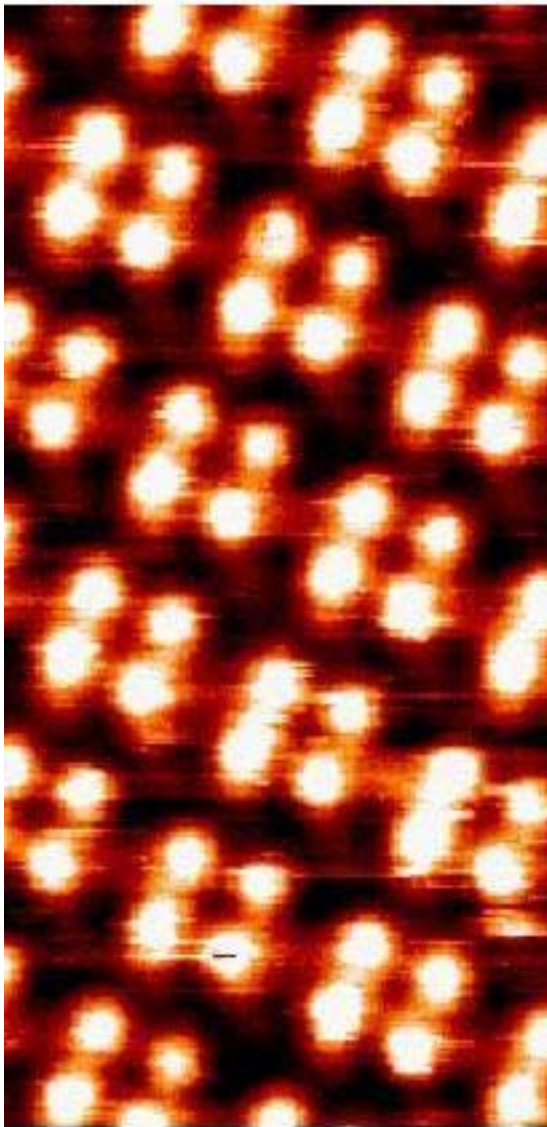


Figure 6.18: Molecular resolution topography, $65 \times 29 \text{ \AA}$ of a saturated coverage of D-alaninol on Cu(100) at constant current ($V_{\text{tip}} = 200 \text{ mV}$, $I_{\text{tip}} = 0.1 \text{ nA}$). It shows an ordered $(4 \ -1, \ 1 \ 4)$ phase, direction of the substrate $[011]$ is shown as well.

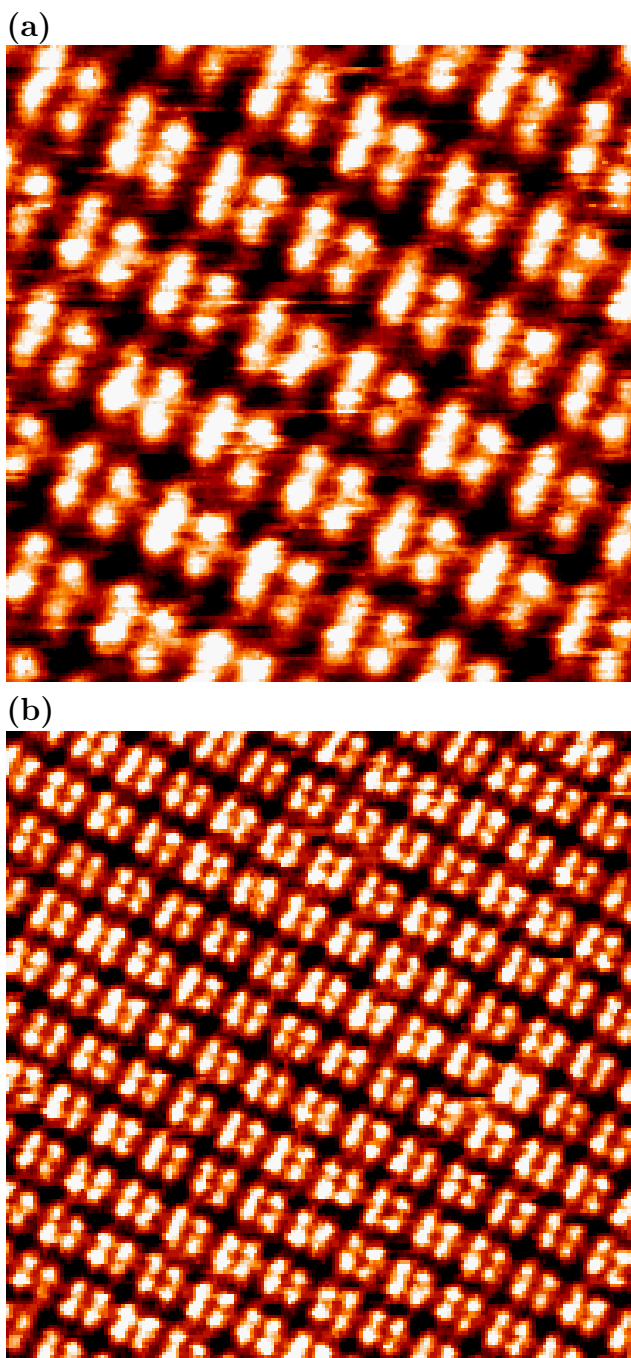


Figure 6.19: STM images of a saturated phase of D-alaninol on Cu(100); **(a)** $57 \times 57 \text{ \AA}$, $V_{\text{tip}} = 600 \text{ mV}$, $I_{\text{tip}} = 0.1 \text{ nA}$; **(b)** $128 \times 128 \text{ \AA}$, $V_{\text{tip}} = 300 \text{ mV}$, $I_{\text{tip}} = 0.1 \text{ nA}$. Different images in different position of the same sample demonstrate that ordered phase found is global confirming LEED results.

is taken.

Image of clean Cu(100) surface are presented, these were used to calibrate the apparatus and confirm orientation for the chemisorbed reconstruction shown in figures 6.18 and 6.19. Clean Cu(100) surface can be seen in figure 6.21.

This technique, therefore, permits to investigate deeper the adsorption structure displaying the shape of the adsorbate without damage it, because the molecular systems appeared to be photo-sensitive, as also reported in literature for butandiol, acetic acid and alanine.

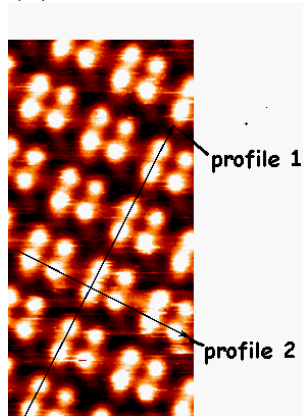
6.2.5 Conclusions: Adsorption Structure

We have succeeded in the formation of the two-dimensional structure in the self-assembled monolayer (SAM) made from gas deposition of D-alaninol. Chiral assemblies formed by adsorption of D-Alaninol on Cu(100) has been demonstrated by LEED and STM images, below 15L no ordered structure appears and adsorption is made with oxygen lone pairs, after 15L, D-Alaninol self-assembles into an ordered superstructure, with a LEED pattern detected, bonding with both oxygen and nitrogen aligning in long chains similarly as others systems like alanine [113].

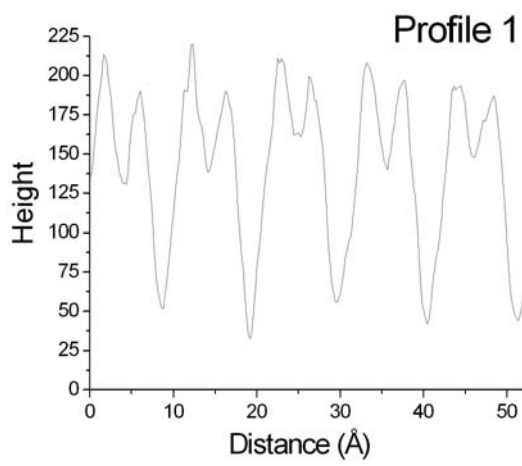
STM images of alanine [113] and glycine [114] on Cu(100) reported from original works are presented in figure 6.22 to investigate analogy with the present system.

In this two similar structures unit cells are made of two protrusions indicating two molecules that are connected by N-H-O hydrogen bonds to form chains in the [130] direction. Glycine studies reveal that it adsorbs on Cu(100) at low coverage with oxygens and then increasing coverage saturates into a

(1)



(2)



(3)

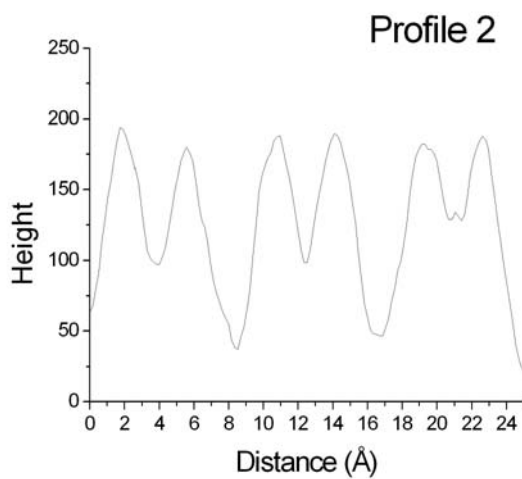


Figure 6.20: (2) and (3) are line profiles for (1) image 6.18 in which profile are labelled.

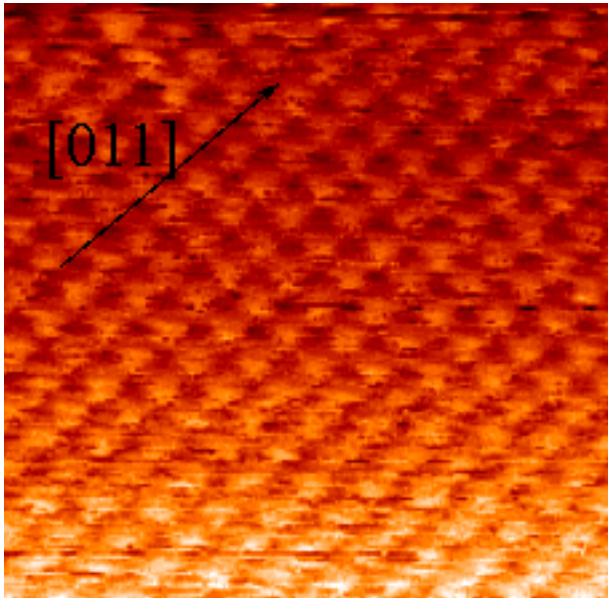
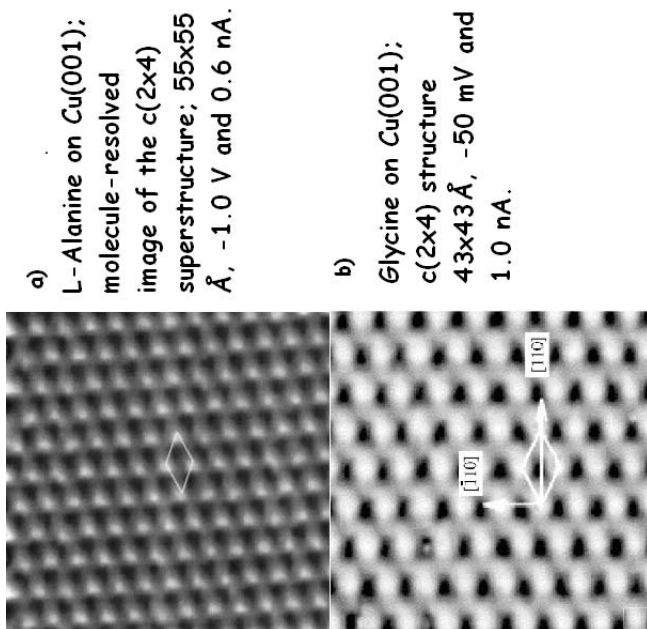


Figure 6.21: A 36x36 Å STM constant current image of Cu(100); $V_{\text{tip}} = 80$ mV, $I_{\text{tip}} = 1$ nA; copper atoms are clearly resolved and (100) structure is easily seen as illustrated in figure 6.3.



a) L-Alanine on Cu(001); molecule-resolved image of the c(2x4) superstructure; 55x55 Å, -1.0 V and 0.6 nA.

b) Glycine on Cu(001); c(2x4) structure 43x43 Å, -50 mV and 1.0 nA.

Figure 6.22: Alanine and glycine on Cu(001) [113] and [114].

monolayer, chiral motifs created are only locals since homo- and hetero-chiral domains - $c(2 \times 4)$ and $p(2 \times 4)$, respectively - co-exist. Adsorption of alanine saturates forming a chirally oriented monolayer, the homochiral domain is illustrated in figure 6.22, and bonds are formed through both carboxylic and amino terminations.

The fundamental study on tartaric acid by Ortega Lorenzo et al. [40] suggests that heterogeneous enantioselectivity can be induced by adsorbing chiral molecules onto catalytically active surfaces. Adsorption of chiral molecules creates chiral templates exposing metal atoms and this chiral substrate spaces are responsible for imparting enantioselectivity to the newly functionalized surface.

Finally, a model for chemisorption structure is presented in figure 6.23 considering directions and shapes deduced from LEED and STM images of the saturated phase.

6.3 D-Alaninol on Cu(110): Growth Dynamics

D-alaninol was also deposited on Cu(110) to understand how different surface symmetry can influence the growth and creates properties of the functionalized surface which are illustrated in figure 6.27 and in section 6.1.

Photoelectron spectra are presented in figure 6.24. Spectra were recorded at $h\nu=1253.6$ eV ($MgK\alpha$), radiation is incidence at 20° , with a pass energy of 70 eV corresponding to an estimated resolution of 300 meV. Detector is placed at 40° from the normal to the surface. Binding energy scale is calibrated against Cu 2p core line and Fermi level.

This system achieves a saturation coverage at 0.3L. C 1s line does not change along the growth, instead, both N1s and O1s structures appear more

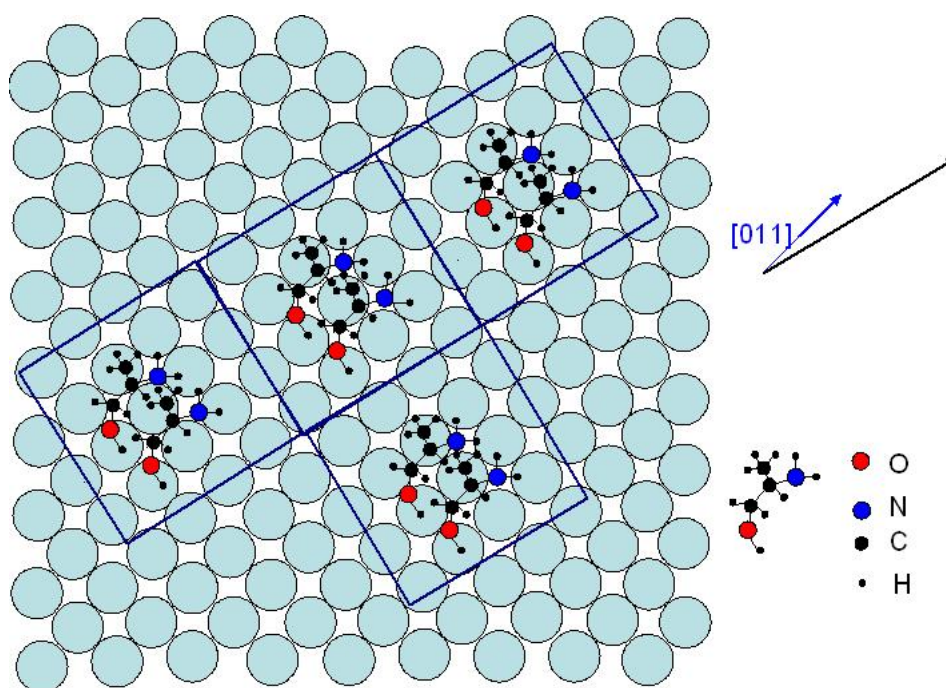


Figure 6.23: A model for chemisorption of D-Alaninol on Cu(100) is, here, presented. Blue and red circles represent oxygen and nitrogen atoms, respectively; carbon is shown in small black spot and hydrogen are neglected for clarity. Blue square are indicative of the diffracting unit in order to show the alignment direction.

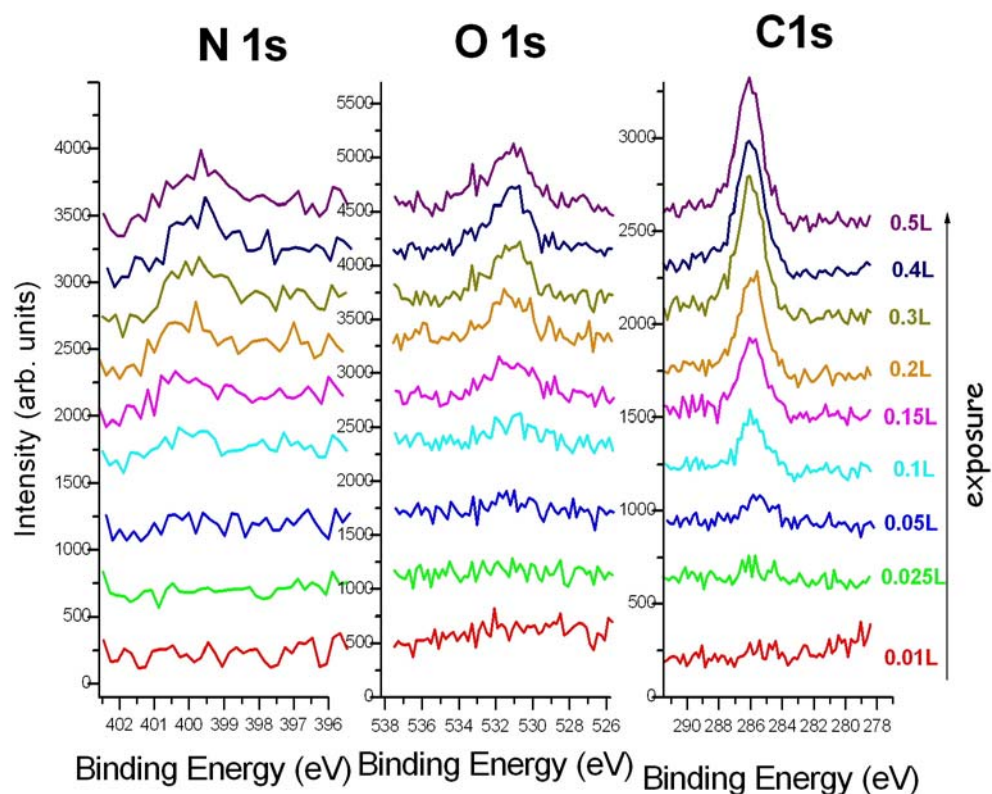


Figure 6.24: C1s, O1s and N1s lines of Alaninol on Cu(110) as a function of the exposure L. All spectra are vertically stacked and background has been subtracted.

and more complex at increasing coverage.

Growth of D-Alaninol on Cu(110) results to follow Langmuir law and reaches a saturation coverage into a monolayer at room temperature. This behaviour is investigated as for deposition on Cu(100), and is presented in figure 6.25 with fitting details as well. Saturation coverage is reached much faster than for Cu(100) this can be explaining considering that Cu(110) surface has a lower density of atoms than Cu(100)(about $\sqrt{2}$ times less).

An higher resolution spectra of N1s and O1s was recorded at saturation coverage and is shown in figure 6.26. N1s spectra is reproduced with two components at 397.2 eV and at 399.5 eV while O1s has two lines at 530.4 eV

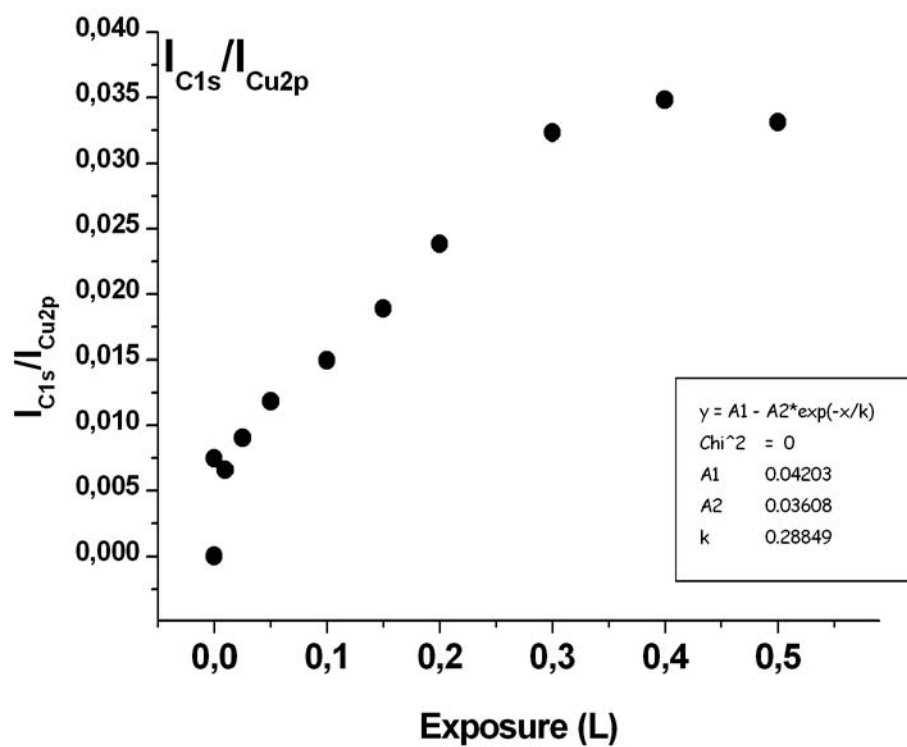


Figure 6.25: Growth of D-Alaninol on Cu(110). Uncertainty is estimated as 20% both for ordinate and abscissa. Inset displays Langmuir fit parameters.

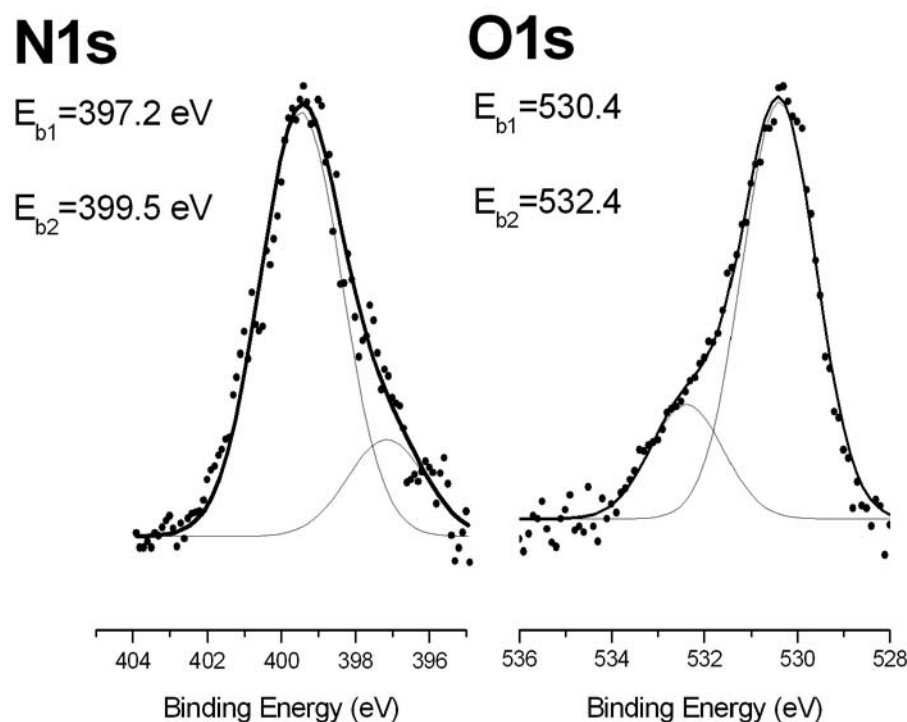


Figure 6.26: High resolution spectra of N 1s and O 1s core line and 532.4 eV.

Conclusion and perspectives Dynamic of the growth of D-alaninol on Cu(110) has been investigated by means of XPS. This system reaches a saturated coverage forming a monolayer and respecting growth law of Langmuir; moreover both $-\text{NH}_2$ and $-\text{OH}$ are involved in bonding.

A more complex bonding structure is formed in comparison to Cu(100) this can be due to a different crystallographic order of the surface atoms which are illustrated in figure 6.27. Literature on chemisorption on Cu(110) is wide and often it shows a more complicated phase diagram than adsorption on Cu(100).

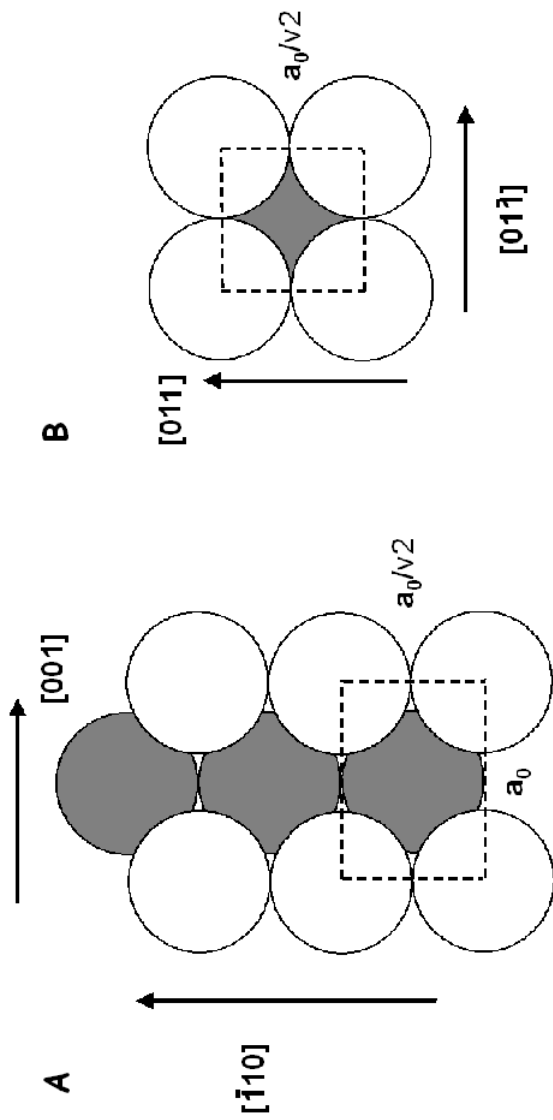


Figure 6.27: Surface structure of A) Cu(100) and B) Cu(110).

More essential informations can be obtained from LEED and STM experiments.

Chapter 7

Conclusions and Future Development

Since the last century chirality has attracted a general interest because of the surprising homochirality found in biological and abiogenic systems. In the last decades huge funding has been provided to this field, due to the wide potential applications of chiral compounds and, as they are promising tools to modify chemical and physical properties of surfaces.

This thesis work has been focused on the evolution of chiral properties, first determined through the measure of molecular dichroism via CDAD and how these molecules can modify a metal surface through adsorption and spontaneous aggregation in ordered assembly.

D- and L-Alaninol has been taken as a model system for a wide class of molecules, containing amino and hydroxilic groups, giving rise to self-assembled monolayers. Investigation of CDAD was carried out in an innovative experimental set-up developed in the last few years. A surface science study was performed with standard tools to develop a reproducible procedure of thin film growth on metal surfaces characterized by a chiral template assembly in a

controlled way. The use of complementary research tools - photoelectron spectroscopy, diffraction and microscopy - has been addressed as a fundamental issue to reveal the adsorption mechanism, chiral ordering and the electronic properties of the Alaninol/Cu(100) interface.

A relevant part of this work has been devoted to set up and progressively improve the AR-XPS apparatus previously described. It has been devised for characterization of low-dimensional systems (organic and inorganic) at room temperature by angular-resolved X-ray photoelectron spectroscopy and low energy electron diffraction.

Hereafter, the main results of the experimental investigations are summarized.

CDAD was measured for L- and D-Alaninol in gas phase and it results to be a very promising tool for chiral discrimination and for investigation of the dichroic parameter as a sensitive probe for structural and electronic properties. An ordered chemisorption phase has been identified for the D-Alaninol/Cu(100) system deposited at room temperature and characterized by photoelectron spectroscopies, LEED and STM showing both amino and hydroxilic functionals driving the adsorption by acting as “hook” to the surface. Thus, D-Alaninol is found to form an ordered superstructure in consequence of adsorption being driven from hydrogen bonds between the two functionals.

As a possible perspective, the multi-technique approach outline may be extended using the CDAD to study chiral surface systems. Attention has to be directed to the fact that spatially fixed systems have been proved (theoretically and experimentally) to induce a CDAD effect also for linear, and thus non chiral, molecules. This effect vanishes when \mathbf{k} and \mathbf{q} are in a substrate symmetry plane as illustrated in figure 7.1.[115]

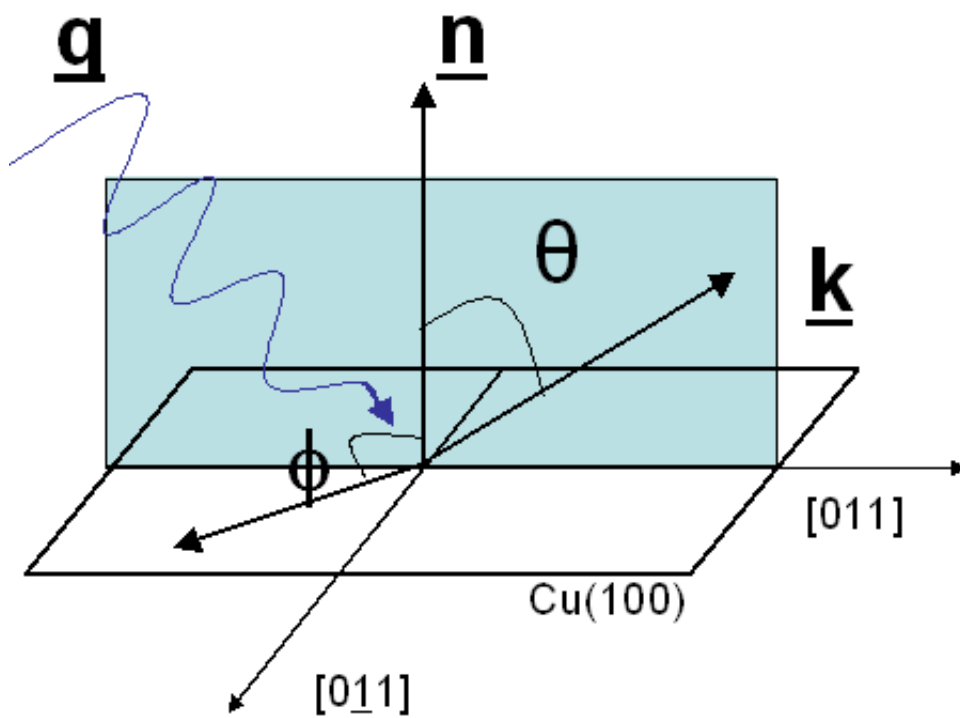


Figure 7.1: Proper geometry must be chosen to disentangle the CDAD effect due to chiral molecule oriented on surface and the orientational effect. Schematic view of the experimental geometry is illustrated, three vectors define the systems: \underline{n} is the normal to the surface, \underline{q} is the direction of light incidence, and \underline{k} is the direction of electron emission. CD effect is supposed to emerge scanning emission angles θ and ϕ .

This analysis is in a preliminary stage and few contributions are already available [116, 117] and still no definitive conclusions could be drawn. Such technique can be used in the future to discriminate between enantiomers of chiral substance oriented in space by having them adsorbed on a surface in a direct way as it is used in the gas-phase case.

Moreover, angle-resolved apparatus available can provide a complete band mapping of the D-Alaninol/Cu(100) in the valence region. The band mapping can bring into evidence the existence of interface electronic levels derived from chemisorption which are expected to present a dispersion, $E(k_{||})$. Alaninol/Cu(100) was found to be damaged both from light and electron beams. Light-induced damage appears in a hour so a conventional angular analyzer such as that described in section 4.1 is inadequate since it requires many hours to perform a complete map. New types of analyzers have recently come out, which permit the collection of collect an intensity map of photoelectrons on a bidimensional detector as a function of energy and angle in such a way as to gain for each kinetic energy the \mathbf{k} dispersion. Such kinds of analyzer allow us to collect data quickly with a low signal/noise ratio. It thus minimizes the time needed to obtain reliable measurements.

These new generation angle-resolved detectors are useful for CDAD measurement for adsorbed/substrate systems as well, since these experiments require repeated measures for left- and right-polarization and an high statistic to determine the dichroic parameter whose magnitude is expected to be of the order of a few percent.

Furthermore, the fruitful interchange between experimental and theoretical investigations is crucial to elucidate the interplay between geometric structure and electronic response for oriented and non oriented systems. For this

purpose a deep computational study on the randomly oriented Alaninol and chemisorption phase of Alaninol on metal surfaces would be a useful tool to corroborate the experimental results. A preliminary investigation of D-Alaninol on Cu(100) has been performed with Quantum-Espresso code [118], based on density-functional theory which uses a Plane Wave basis set and pseudopotential, at this stage a predicted structure is not yet available.

Finally, an intimate understanding of the mechanism beneath homochirality, chiral discrimination and chiral assembling, the chemical and physical properties at the interface, is a fundamental step toward the development of sophisticated nanotechnologies.

Acknowledgements

This work was supported by a CNR Ph.D fellowship, I gratefully acknowledge the ISM staff for their support, especially, Dott. Tommaso Prospero, Dott. Nicola Zema, Dott. Giorgio Contini and Dott. Stefano Turchini for their constant help and teaching. A special acknowledgement is made, also, to Mario Capozzi and Massimo Brolatti for their technical support. The assistance of Paolo Moras, Corrado Crotti and Jun Fujii at ELETTRA SRF are acknowledged.

The research reported in this theses made use of the CASPUR workstations and I wish to thank Prof. F.A. Gianturco, Dott. Nico Sanna, Dott. Andrea Grandi, Dott. Andrea Pieretti and Dott. Amedeo Palma.

Bibliography

- [1] J. M. Hicks, editor, *Chirality: Physical Chemistry*, American Chemical Society, Washington, DC, 2002.
- [2] R. Raval and S. M. Barlow, *Surf. Sci. Rep* **50**, 201 (2003).
- [3] F. Rosei et al., *Progr. Surf. Sci.* **71**, 95 (2003).
- [4] S. F. Mason, *Molecular optical activity and the chiral discriminations*, Cambridge University Press, 1981.
- [5] L. Alagna et al., *Phys. Rev. Lett* **80**, 4799 (1998).
- [6] N. Bowering et al., *Phys. Rev. Lett* **86**, 1187 (2001).
- [7] S. Turchini et al., *Phys. Rev. A* **70**, 014502 (2004).
- [8] S. Nakagawa, A. Tai, T. Okuyama, and T. Sugimura, *Topics in Catalysis* **13**, 187 (2000).
- [9] K. L. Barbu, F. Lahmani, and A. Zehnacker-Rentien, *J. Phys. Chem. A* **106**, 6271 (2002).
- [10] R. Fausto, C. Cacula, and M. Duarte, *J. Mol. Struct.* , 365 (2001).
- [11] H. Y. A. Hannun and R. M. Bell, *Science* **243**, 500 (1989).

- [12] S. Canepari, V. Carunchio, P. Castellano, and A. Messina, *Talanta* **44**, 2059 (1997).
- [13] S. F. Mason, *Chemical Evolution*, Oxford University Press, 1991.
- [14] L. Pasteur, *Researchs on molecular asymmetry*, volume 14, Alembic Club Reprint, 1948.
- [15] E. Fisher, *Ber. dtsch. chem. Ges.* **27**, 2985 (1894).
- [16] E. Fisher, *Z. Physiol. Chem.* **26**, 60 (1898).
- [17] E. Fisher, *J. Chem. Soc.* **91**, 1749 (1907).
- [18] E. Fisher, *Ber. dtsch. chem. Ges.* **24**, 2683 (1891).
- [19] M. H. Engel and B. Nagy, *Nature* **296**, 837 (1982).
- [20] M. H. Engel and S. A. Macko, *Nature* **389**, 285 (1997).
- [21] J. R. Cronin and S. Pizzarello, *Science* **275**, 951 (1997).
- [22] A. Cotton, *Ann Chim. Physique* **8**, 347 (1896).
- [23] W. Kuhn, *Z. physik. Chem. B* **31**, 23 (1936).
- [24] W. Kuhn, *Trans. Faraday Soc.* **26**, 293 (1930).
- [25] A. Franklin, *Stud. Hist. Philos. Sci.* **10**, 201 (1979).
- [26] T. D. Lee and C. N. Yang, *Phys. Rev.* **88**, 101 (1956).
- [27] J. Bailey et al., *Science* **281**, 672 (1998).
- [28] F. Arango, *Mém. Classe Sci. Math. Phys. Inst. Impér.* **12 I** (1812).
- [29] J. B. Biot, *Ann. Chim. Physique* **4**, 90 (1817).

- [30] L. Pasteur, *Ann. Chim. Phys.* **24**, 442 (1848).
- [31] L. Pasteur, *C. R. hebd.Séances Acad. Sci.* **28**, 477 (1849).
- [32] L. Pasteur, *C. R. hebd.Séances Acad. Sci.* **29**, 297 (1849).
- [33] L. Pasteur, *Ann. Chim. Physique* **28**, 56 (1850).
- [34] J. A. L. Bell, *Bull. Soc. chim.* **22**, 337 (1874).
- [35] J. H. Van't Hoff, *Bull. Soc. chim.* **23**, 295 (1875).
- [36] R. S. Cahn, C. K. Ingold, and V. Prelog, *Angew. Chem.* **78**, 413 (1966).
- [37] L. Chen-Hsing, L. Ching-Erh, C. Chia-Chong, and L. Li-Fang, *J Chinese Chem.Soc.* **48**, 1069 (2001).
- [38] R. M. Hazen and D. S. Sholl, *Nature Materials* **2**, 367 (2003).
- [39] R. Raval, *J. Phys.: Condens. Matter* **14**, 4119 (2002).
- [40] M. O. Lorenzo, C. J. Baddeley, C. Muryn, and R. Raval, *Nature* **404** (2000).
- [41] A. Kuhnle, T. R. Linderoth, B. Hammer, and F. Besenbacher, *Nature* **415**, 891 (2002).
- [42] K. H. Ernst et al., *Nanotechnology* **10**, 1 (1999).
- [43] V. A. Davankov, *Chirality* **9**, 99 (1997).
- [44] G. Somorjai, *Surface Chemistry and Catalysis*, Wiley, New York, 1994.
- [45] G. Ertl, *Surf. Sci* **299/300**, 742 (1994).
- [46] F. Besenbacher et al., *Science* **279**, 1913 (1998).

- [47] D. A. King, *Stud. Surf. Sci. Catal* **109**, 70 (1997).
- [48] J. D. Van der Waals, *Doctoral Dissertation*, Leiden, 1873.
- [49] J. D. Van der Waals, *Chem. Rev.* **88** (1988).
- [50] J. D. Van der Waals, *Chem. Rev.* **94**, 7 (1994).
- [51] G. Attard and C. Barnes, *Surfaces*, Oxford University Press.
- [52] A. S. Duwez, *J. El. Spectr. Rel. Phen.* **134**, 97 (2004).
- [53] F. Schreiber, *Prog. Surf. Sci.* **65**, 151 (2000).
- [54] R. Fowler and E. Guggenheim, *Statistical Thermodynamics*, Cambridge University Press, Cambridge, UK, 1965.
- [55] S. Curtarolo, G. Stan, M. W. Cole, M. J. Bojan, and W. A. Steele, *Phys. Rev. E* **59**, 4402 (1999).
- [56] D. M. Young and A. D. Crowell, *Physical Adsorption of Gases*, volume 10, Butterworths, London, 1962.
- [57] C. D. Bruce, T. R. Rybolt, H. E. Thomas, T. E. Agnew, and B. S. Davis, *J Colloid Interface Sci.* **194**, 448 (1997).
- [58] I. Langmuir, *J. Am. Chem.Soc.* **39**, 1848 (1917).
- [59] I. Langmuir, *Trans. Faraday Soc.* **15**, 62 (1920).
- [60] S. Canepari, V. Carunchio, and R. Schina, *Polyhedron* **18**, 3263 (1999).
- [61] A. H. Jr Merrill et al., *J. Biol. Chem.* **261**, 2610 (1986).
- [62] M. Faucher, N. Girones, Y. A. Hannun, R. M. Bell, and R. J. Davis, *J. Biol. Chem.* **263**, 5319 (1988).

- [63] L. A. Speizer, M. J. Watson, and L. Bruton, *Fed. Proc.* **46**, 2065 (1987).
- [64] Y. A. Hannun and R. Bell, *Science* **235**, 678 (1987).
- [65] E. Wilson, M. C. Olcott, R. M. Bell, A. H. Merrill Jr, and J. D. Lambeth, *J. Biol. Chem.* **261**, 12616 (1986).
- [66] G. M. Gragg, D. J. Newman, and K. M. Snader, *J. Nat. Prod.* **60**, 52 (1997).
- [67] Y. Z. Shu, *J. Nat. Prod.* **61**, 1053 (1998).
- [68] E. L. Eliel, S. H. Wilen, and L. N. Mander, *Stereochemistry of Organic Comounds*, Wiley, 1994.
- [69] J. M. Bijvoet, A. F. Peerdeman, and A. J. van Bommel, *Nature* **168**, 271 (1951).
- [70] J. B. Biot, *Ann. Chim. Physique* **59**, 206 (1860).
- [71] P. A. Levene and A. Rothen, *Organic Chemistry*, volume 2, John Wiley, New York, 1938.
- [72] K. Rudolph, *J. opt. Soc. America* **45**, 50 (1955).
- [73] O. C. Rudolph and Sons constructor, Caldwell, N.Y.
- [74] M. Billardon and J. Badoz, *C. R. herb. Séances acad. Sci.* **248**, 2466 (1959).
- [75] M. Grosjean, A. Lacam, and M. Legrand, *Bull. Soc. chim. France* , 1495 (1959).
- [76] T. J. Wenzel, *Encyclopedia of Spectroscopy and Spectrometry*, volume 1, pages 411–421, Academic Press, New York, 2000.

- [77] G. Holzwarth et al., J. Am. Chem. Soc. **96**, 251 (1974).
- [78] L. A. Nafie et al., J. Am. Chem. Soc. **97**, 3842 (1975).
- [79] G. A. Garcia et al., J. Chem. Phys. **119**, 8781 (2003).
- [80] A. Giardini et al., Chem. Phys. Chem. **6**, 1164 (2005).
- [81] A. Einstein, Ann. Der Phys. **17**, 132 (1905).
- [82] P. A. Millikan, Phys. Rev. **7**, 362 (1916).
- [83] P. Lennard, Ann. Der Phys. **4**, 149 (1902).
- [84] A. Ernst, W. M. Temmerman, Z. Szotek, M. Woods, and P. Durham, Philosophical Magazine B **78**, 503 (1998).
- [85] M. Luders, A. Ernst, W. M. Temmerman, Z. Szotek, and P. J. Durham, J. Phys.: Condens. Matter **13**, 8587 (2001).
- [86] Y. N. Chiu, J. Chem. Phys. **50**, 5336 (1969).
- [87] B. Ritchie, Phys. Rev A **12**, 567 (1975).
- [88] L. Ley and M. Cardona, *Photoemission in Solids I and II*, Springer-Verlag, 1979.
- [89] G. Binning, H. Rohrer, C. Gerber, and E. Weibel, Phys. Rev. Lett. **49**, 37 (1982).
- [90] R. P. Walker and B. Diviacco, Rev. Sci. Instrum. **63**, 332 (1992).
- [91] M. J. Frisch et al., Gaussian 03, revision c.02, Gaussian, Inc., Wallingford, CT, 2004.
- [92] J. Koopmans, Physica **1**, 104 (1933).

- [93] W. Kohn and L. J. Sham, Phys. Rev **140**, A1133 (1965).
- [94] A. D. Becke, J. Chem. Phys. **98** (1993).
- [95] C. Lee, W. Yang, and R. Parr, Phys. Rev. B **37**, 785 (1988).
- [96] B. Miehlich, A. Savin, H. Stoll, and H. Preuss, Chem. Phys. Lett. **157**, 200 (1989).
- [97] S. H. Vosko, L. Wilk, and M. Nusair, Can. J. Phys. **58** (1980).
- [98] I. Powis, E. E. Rennie, U. Hergenhahn, O. Kungeler, and R. B. Socrate, J. Phys. Chem. **107**, 25 (2003).
- [99] L. Klasinc, J. Elec. Spec. Relat. Phenom. **8**, 161 (1976).
- [100] U. Gelius et al., Physica Scripta **2**, 70 (1970).
- [101] E. Rennie et al., J. Phys. Chem. **106**, 12221 (2002).
- [102] A. R. Slaughter and M. S. Banna, J. Phys. Chem. **92**, 2165 (1988).
- [103] D. P. Chong, Can. J. Chem. **74**, 1005 (1996).
- [104] D. T. Clark, J. Peeling, and L. Colling, Biochim. Biophys. Acta **453**, 533 (1976).
- [105] M. Stener, G. Fronzoni, D. S. D. Tommaso, and P. Decleva, J. Chem. Phys. **120**, 3284 (2004).
- [106] R. J. Lavrich, R. L. Rhea, J. W. McCargar, and M. J. Tubergen, J. Mol. Spectr. **199**, 138 (2000).
- [107] H. Luth, *Surface and Interface of Solid Materials*, volume 1995, Springer-Verlag, Berlin Heidelberg New York.

- [108] A. F. Lee, D. E. Gawthrope, N. J. Hart, and K. Wilson, Surf. Sci. **548**, 200 (2004).
- [109] K. Uvald et al., J. Colloid Interface Sci. **149**, 162 (1992).
- [110] K. Uvald et al., J. Colloid Interface Sci. **140**, 207 (1990).
- [111] G. Jung et al., Biochim. Biophys. Acta **295**, 77 (1973).
- [112] V. Bortolani, N. H. March, and M. P. Tosi, editors, *Interaction of atoms and molecules with solid surfaces*, Plenum Press, New York, 1990.
- [113] X. Zhao, R. G. Zhao, and W. S. Yang, Surf. Sci. **442**, L995 (1999).
- [114] X. Zhao, Z. Gai, R. G. Zhao, W. S. Yang, and T. Sakurai, Surf. Sci. **424**, L347 (1999).
- [115] G. Schonhense, Physica Scripta t **31**, 255 (1990).
- [116] M. Policik et al., Phys. Rev. Lett **92**, 236103 (2004).
- [117] J. W. Kim et al., Phys. Rev. Lett **95**, 107601 (2005).
- [118] <http://www.pwscf.org>.

© 2006 SIMONA IRRERA

Realizzazione: Simona Irrera - Via Casalmonferrato, 2/C - 00182 Roma – Tel 067018485